

# Simultaneous Measurement of Oscillation Parameters in Beam and Atmospheric Neutrino Data from Tokai-to-Kamioka and Super-Kamiokande Experiments

# Daniel Robert Clement Barrow

# Magdalen College, Oxford University

<sup>10</sup> A Dissertation Submitted to Oxford University

<sup>11</sup> for the Degree of Doctor of Philosophy

<sup>12</sup>

13                   **Simultaneous Measurement of**

14                   **Oscillation Parameters in Beam and**

15                   **Atmospheric Neutrino Data from**

16                   **Tokai-to-Kamioka and**

17                   **Super-Kamiokande Experiments**

18                   *Abstract*

19                   Lorem ipsum dolor sit amet, consectetur adipiscing elit, sed do eiusmod tempor incididunt ut labore et dolore magna aliqua. Nulla aliquet porttitor lacus luctus accumsan tortor posuere. Pulvinar neque laoreet suspendisse interdum. Sem viverra aliquet eget sit. Nunc sed velit dignissim sodales ut eu sem integer vitae. At erat pellentesque adipiscing commodo elit at imperdiet dui accumsan. Fames ac turpis egestas integer eget aliquet nibh. Scelerisque eu ultrices vitae auctor eu augue. Purus non enim praesent elementum facilisis leo vel. Sollicitudin nibh sit amet commodo. Vitae auctor eu augue ut. Vel quam elementum pulvinar etiam. A condimentum vitae sapien pellentesque habitant morbi tristique senectus. Viverra accumsan in nisl nisi scelerisque eu ultrices. Sed viverra ipsum nunc aliquet bibendum enim. Sit amet purus gravida quis. In vitae turpis massa

<sup>32</sup> sed elementum tempus egestas sed sed. Vivamus arcu felis bibendum  
<sup>33</sup> ut tristique et egestas. Senectus et netus et malesuada fames ac turpis.  
<sup>34</sup> Ac auctor augue mauris augue.

## 35 Declaration

36 This dissertation is the result of my own work, except where ex-  
37 plicit reference is made to the work of others, and has not been sub-  
38 mitted for another qualification to this or any other university. This  
39 dissertation does not exceed the word limit for the respective Degree  
40 Committee.

41 Daniel Robert Clement Barrow

42 ©The copyright of this thesis rests with the author and is made available under a Creative  
43 Commons Attribution Non-Commercial No Derivatives licence. Researchers are free to copy,  
44 distribute or transmit the thesis on the condition that they attribute it, that they do not use  
45 it for commercial purposes and that they do not alter, transform or build upon it. For any  
46 reuse or redistribution, researchers must make clear to others the licence terms of this work.

47

## Acknowledgements

48 at pretium nibh ipsum. Eget nunc scelerisque viverra mauris in aliquam. Arcu vitae  
49 elementum curabitur vitae nunc sed velit dignissim. Sed arcu non odio euismod lacinia  
50 at quis risus sed. Vitae tempus quam pellentesque nec nam aliquam sem et tortor.  
51 Viverra aliquet eget sit amet tellus cras adipiscing. Purus sit amet luctus venenatis  
52 lectus magna. In aliquam sem fringilla ut morbi tincidunt augue. Fermentum dui  
53 faucibus in ornare. Aliquam malesuada bibendum arcu vitae elementum curabitur  
54 vitae nunc sed.

55 Ultricies leo integer malesuada nunc vel risus commodo. Tellus cras adipiscing  
56 enim eu turpis egestas pretium. Dictumst quisque sagittis purus sit amet volutpat  
57 consequat mauris nunc. Vitae congue mauris rhoncus aenean vel elit scelerisque  
58 mauris pellentesque. Vel facilisis volutpat est velit egestas dui id ornare. Suscipit  
59 adipiscing bibendum est ultricies. At in tellus integer feugiat scelerisque varius  
60 morbi enim. Cras semper auctor neque vitae tempus. Commodo sed egestas egestas  
61 fringilla phasellus faucibus. Cras pulvinar mattis nunc sed blandit. Pretium viverra  
62 suspendisse potenti nullam ac tortor vitae. Purus sit amet volutpat consequat. Orci  
63 sagittis eu volutpat odio facilisis mauris. Sit amet massa vitae tortor condimentum  
64 lacinia quis. Commodo sed egestas egestas fringilla phasellus. Sed libero enim sed  
65 faucibus turpis. Vitae tempus quam pellentesque nec.

66 Blandit massa enim nec dui. Viverra tellus in hac habitasse platea dictumst vestibulu-  
67 lum. Bibendum enim facilisis gravida neque convallis. Sagittis nisl rhoncus mattis  
68 rhoncus urna neque. Nisl rhoncus mattis rhoncus urna neque. Ac tortor vitae purus  
69 faucibus ornare. Aenean sed adipiscing diam donec adipiscing tristique risus. Sapien  
70 nec sagittis aliquam malesuada bibendum. Et leo duis ut diam quam nulla. Tellus  
71 rutrum tellus pellentesque eu tincidunt tortor aliquam nulla facilisi. Fermentum leo

<sup>72</sup> vel orci porta non pulvinar neque. Eget sit amet tellus cras adipiscing enim eu. Sed  
<sup>73</sup> viverra tellus in hac habitasse platea dictumst vestibulum.

<sup>74</sup> Sit amet consectetur adipiscing elit. At varius vel pharetra vel turpis nunc eget  
<sup>75</sup> lorem. Elit scelerisque mauris pellentesque pulvinar pellentesque habitant morbi  
<sup>76</sup> tristique senectus. Odio euismod lacinia at quis risus sed vulputate odio. Vitae suscipit  
<sup>77</sup> tellus mauris a diam maecenas sed enim ut. Dignissim convallis aenean et tortor at  
<sup>78</sup> risus viverra. Diam sollicitudin tempor id eu. Erat velit scelerisque in dictum. Blandit  
<sup>79</sup> cursus risus at ultrices. Ac tortor vitae purus faucibus ornare suspendisse sed.

# **Contents**

81	<b>1 Neutrino Oscillation Physics</b>	1
82	1.1 Discovery of Neutrinos . . . . .	1
83	1.2 Theory of Neutrino Oscillation . . . . .	3
84	1.2.1 Three Flavour Oscillations . . . . .	3
85	1.2.2 The MSW Effect . . . . .	7
86	1.3 Neutrino Oscillation Measurements . . . . .	9
87	1.3.1 Solar Neutrinos . . . . .	9
88	1.3.2 Atmospheric Neutrinos . . . . .	12
89	1.3.3 Accelerator Neutrinos . . . . .	15
90	1.3.4 Reactor Neutrinos . . . . .	18
91	<b>2 T2K and SK Experiment Overview</b>	20
92	2.1 The Super-Kamiokande Experiment . . . . .	21
93	2.1.1 The SK Detector . . . . .	22
94	2.1.2 Calibration . . . . .	25
95	2.1.3 Data Acquisition and Triggering . . . . .	28
96	2.1.4 Cherenkov Radiation . . . . .	30
97	2.2 The Tokai to Kamioka Experiment . . . . .	32
98	2.2.1 The Neutrino Beam . . . . .	33
99	2.2.2 The Near Detector at 280m . . . . .	38
100	2.2.2.1 Fine Grained Detectors . . . . .	40
101	2.2.2.2 Time Projection Chambers . . . . .	41
102	2.2.2.3 $\pi^0$ Detector . . . . .	42
103	2.2.2.4 Electromagnetic Calorimeter . . . . .	44
104	2.2.2.5 Side Muon Range Detector . . . . .	45

105	2.2.3 The Interactive Neutrino GRID . . . . .	45
106	<b>3 Bayesian Statistics and Markov Chain Monte Carlo Techniques</b>	48
107	3.1 Bayesian Statistics . . . . .	49
108	3.2 Monte Carlo Simulation . . . . .	50
109	3.2.1 Markov Chain Monte Carlo . . . . .	52
110	3.2.2 Metropolis-Hastings Algorithm . . . . .	55
111	3.2.3 MCMC Optimisation . . . . .	56
112	3.3 Understanding the MCMC Results . . . . .	60
113	3.3.1 Marginalisation . . . . .	60
114	3.3.2 Parameter Estimation and Credible Intervals . . . . .	61
115	3.3.3 Application of Bayes' Theorem . . . . .	63
116	3.3.4 Comparison of MCMC Output to Expectation . . . . .	64
117	<b>4 Simulation, Reconstruction and Event Selections</b>	66
118	4.1 Simulation . . . . .	66
119	4.2 Event Reconstruction at SK . . . . .	71
120	4.3 Event Selection at SK . . . . .	81
121	<b>5 Oscillation Probability Calculation</b>	86
122	5.1 Overview . . . . .	87
123	5.2 Treatment of Fast Oscillations . . . . .	94
124	5.3 Calculation Engine . . . . .	103
125	5.4 Matter Density Profile . . . . .	104
126	5.5 Production Height Averaging . . . . .	111
127	<b>Bibliography</b>	115
128	<b>List of Figures</b>	126

**129 List of Tables****134**



<sup>131</sup> **Chapter 1**

<sup>132</sup> **Neutrino Oscillation Physics**

<sup>133</sup> When first proposed, neutrinos were expected to be massless fermions that only in-  
<sup>134</sup> teract through weak and gravitational forces. This meant they were very difficult to  
<sup>135</sup> detect as they can pass through significant amounts of matter without interacting. De-  
<sup>136</sup> spite this, experimental neutrino physics has developed with many different detection  
<sup>137</sup> techniques and neutrino sources being used today. In direct tension with **the** standard  
<sup>138</sup> model physics, neutrinos have been determined to oscillate between different lepton  
<sup>139</sup> flavours, requiring them to have mass.

<sup>140</sup> **The observation techniques which lead to the discovery of the neutrino are doc-**  
<sup>141</sup> **umented in section 1.1.** The theory underpinning neutrino oscillation is described in  
<sup>142</sup> section 1.2. This section includes the approximations which can be made to simplify  
<sup>143</sup> the understanding of neutrino oscillation in a two-flavour approximation as well  
<sup>144</sup> as how the medium in which neutrinos propagate can manipulate the oscillation  
<sup>145</sup> probability. **Past**, current, and future neutrino experiments are detailed in section 1.3,  
<sup>146</sup> including the reactor, atmospheric, and long-baseline accelerator neutrino sources that  
<sup>147</sup> have been used to successfully constrain oscillation **parameters determination**.

<sup>148</sup> **1.1 Discovery of Neutrinos**

<sup>149</sup> At the start of the 20<sup>th</sup> century, the electrons emitted from the  $\beta$ -decay of the nucleus  
<sup>150</sup> were found to have a continuous energy spectrum [1,2]. This observation seemingly  
<sup>151</sup> broke the energy conservation invoked within that period's nuclear models. Postulated

in 1930 by Pauli as the solution to this problem, the neutrino (originally termed “neutron”) was theorized to be an electrically neutral spin-1/2 fermion with a mass of the same order of magnitude as the electron [3]. This neutrino was to be emitted with the electron in  $\beta$ -decay to alleviate the apparent breaking of energy conservation. As a predecessor of **the today's** weak interaction model, Fermi's theory of  $\beta$ -decay developed the understanding by coupling the four constituent particles; electron, proton, neutron, and neutrino, into a consistent model [4].

Whilst Pauli was not convinced of the ability to detect neutrinos, **the first observations of the particle were made in the mid-1950s when neutrinos from a reactor were observed via the inverse  $\beta$ -decay (IBD) process,  $\bar{\nu}_e + p \rightarrow n + e^+$  [5, 6]. The detector consisted of two parts: a neutrino interaction medium and a liquid scintillator.** The interaction medium was built from two water tanks. These were loaded with cadmium chloride to allow increased efficiency of neutron capture. The positron emitted from IBD annihilates,  $e^+ + e^- \rightarrow 2\gamma$ , generating a prompt signal and the neutron is captured on the cadmium via  $n + ^{108}Cd \rightarrow ^{109^*}Cd \rightarrow ^{109}Cd + \gamma$ , producing a delayed signal. **The experiment observed an increase in the neutrino event rate when the reactor was operating compared to when it was switched off, in much the same way as modern reactor neutrino experiments operate. An increase in the coincidence rate was observed when the reactor was operating which was interpreted as interactions from neutrinos generated in the reactor.**

After the discovery of the  $\nu_e$ , the natural question of how many flavours of neutrino exist was asked. In 1962, a measurement of the  $\nu_\mu$  was conducted at the Brookhaven National Laboratory [7]. A proton beam was directed at a beryllium target, generating a  $\pi$ -dominated beam which then decayed via  $\pi^\pm \rightarrow \mu^\pm + (\nu_\mu, \bar{\nu}_\mu)$ , and the subsequent interactions of the  $\nu_\mu$  were observed. **As the subsequent interaction of the neutrino generates muons rather than electrons, it was determined the  $\nu_\mu$  was**

178    **fundamentally different from  $\nu_e$ .** The final observation to be made was that of the  
179     $\nu_\tau$  from the DONUT experiment [8]. Three neutrinos seem the obvious solution as it  
180    mirrors the known number of charged lepton (as they form weak isospin doublets) but  
181    there could be evidence of more. Several neutrino experiments have found anomalous  
182    results [9, 10] which could be attributed to sterile neutrinos however cosmological  
183    observations indicate the number of neutrino species  $N_{eff} = 2.99 \pm 0.17$  [11]. DB:  
184    Need to determine how  $N_{eff}$  is calculated.

## 185    1.2 Theory of Neutrino Oscillation

186    As direct evidence of beyond Standard Model physics, a neutrino generated with  
187    lepton flavour  $\alpha$  can change into a different lepton flavour  $\beta$  after propagating some  
188    distance. This phenomenon is called neutrino oscillation and requires that neutrinos  
189    must have a non-zero mass (as seen in subsection 1.2.1). This **observation** is direct  
190    evidence of beyond standard model physics. This behaviour has been characterised  
191    by the Pontecorvo-Maki-Nakagawa-Sakata (PMNS) [12–14] mixing matrix which  
192    describes how the flavour and mass of neutrinos are associated. This is analogous to  
193    the Cabibbo-Kobayashi-Maskawa (CKM) [15] matrix measured in quark physics.

### 194    1.2.1 Three Flavour Oscillations

195    The PMNS parameterisation defines three flavour eigenstates,  $\nu_e$ ,  $\nu_\mu$  and  $\nu_\tau$  (indexed  
196     $\nu_\alpha$ ), which are **assigned based upon eigenstates of** the weak interaction **flavour states**  
197    and three mass eigenstates,  $\nu_1$ ,  $\nu_2$  and  $\nu_3$  (indexed  $\nu_i$ ). Each mass eigenstate is the  
198    superposition of all three flavour states,

$$|\nu_i\rangle = \sum_{\alpha} U_{\alpha i} |\nu_{\alpha}\rangle. \quad (1.1)$$

199 Where  $U$  is the PMNS matrix which **is unitary and connects correlates** the mass  
200 and flavour eigenstates.

201 ~~Neutrinos interact with leptons of the same weak flavour eigenstate rather than~~  
202 ~~mass eigenstate. The weak interaction couples to flavour eigenstates so neutrinos~~  
203 ~~interact with leptons of the same flavour.~~ The propagation of a neutrino flavour  
204 eigenstate, in a vacuum, can be re-written as a plane-wave solution to the time-  
205 dependent Schrödinger equation,

$$|\nu_{\alpha}(t)\rangle = \sum_i U_{\alpha i}^* |\nu_i\rangle e^{-i\phi_i}. \quad (1.2)$$

206 The probability of observing a neutrino of flavour eigenstate  $\beta$  from one which  
207 originated as flavour  $\alpha$  can be calculated as,

$$P(\nu_{\alpha} \rightarrow \nu_{\beta}) = |\langle \nu_{\beta} | \nu_{\alpha}(t) \rangle|^2 = \sum_{i,j} U_{\alpha i}^* U_{\beta i} U_{\alpha j} U_{\beta j}^* e^{-i(\phi_j - \phi_i)} \quad (1.3)$$

208 The  $\phi_i$  term can be expressed in terms of the energy,  $E_i$ , and magnitude of the  
209 three momenta,  $p_i$ , of the neutrino,  $\phi_i = E_i t - p_i x$  ( $t$  and  $x$  being time and position  
210 coordinates). Therefore,

$$\phi_j - \phi_i = E_j t - E_i t - p_j x + p_i x. \quad (1.4)$$

<sup>211</sup> For a relativistic particle,  $E_i \gg m_i$ ,

$$p_i = \sqrt{E_i^2 - m_i^2} \approx E_i - \frac{m_i^2}{2E_i}. \quad (1.5)$$

<sup>212</sup> Making the approximations that neutrinos are relativistic, the mass eigenstates  
<sup>213</sup> were created with the same energy and that  $x = L$ , where  $L$  is the distance traveled by  
<sup>214</sup> the neutrino, Equation 1.4 then becomes

$$\phi_j - \phi_i = \frac{\Delta m_{ij}^2 L}{2E}, \quad (1.6)$$

<sup>215</sup> where  $\Delta m_{ij}^2 = m_i^2 - m_j^2$ . This, **teamed combined** with further use of unitarity  
<sup>216</sup> relations results in Equation 1.3 becoming

$$\begin{aligned} P(\nu_\alpha \rightarrow \nu_\beta) &= \delta_{\alpha\beta} - 4 \sum_{i>j} \Re \left( U_{\alpha i}^* U_{\beta i} U_{\alpha j} U_{\beta j}^* \right) \sin^2 \left( \frac{\Delta m_{ij}^2 L}{4E} \right) \\ &\quad + (-) 2 \sum_{i>j} \Im \left( U_{\alpha i}^* U_{\beta i} U_{\alpha j} U_{\beta j}^* \right) \sin \left( \frac{\Delta m_{ij}^2 L}{2E} \right). \end{aligned} \quad (1.7)$$

<sup>217</sup> Where  $\delta_{\alpha\beta}$  is the Kronecker delta function and the negative sign **on the last term** is  
<sup>218</sup> included for the oscillation probability of antineutrinos.

<sup>219</sup> Typically, the PMNS matrix is parameterised into three mixing angles, a charge  
<sup>220</sup> parity (CP) violating phase  $\delta_{CP}$ , and two Majorana phases  $\alpha_{1,2}$ ,

$$U = \underbrace{\begin{pmatrix} 1 & 0 & 0 \\ 0 & c_{23} & s_{23} \\ 0 & -s_{23} & c_{23} \end{pmatrix}}_{\text{Atmospheric, Accelerator}} \underbrace{\begin{pmatrix} c_{13} & 0 & s_{13}e^{-i\delta_{CP}} \\ 0 & 1 & 0 \\ -s_{13}e^{-i\delta_{CP}} & 0 & c_{13} \end{pmatrix}}_{\text{Reactor, Accelerator}} \underbrace{\begin{pmatrix} c_{12} & s_{12} & 0 \\ -s_{12} & c_{12} & 0 \\ 0 & 0 & 1 \end{pmatrix}}_{\text{Reactor, Solar}} \underbrace{\begin{pmatrix} e^{i\alpha_1/2} & 0 & 0 \\ 0 & e^{i\alpha_2/2} & 0 \\ 0 & 0 & 1 \end{pmatrix}}_{\text{Majorana}}. \quad (1.8)$$

<sup>221</sup> Where  $s_{ij} = \sin(\theta_{ij})$  and  $c_{ij} = \cos(\theta_{ij})$ . The oscillation parameters are often  
<sup>222</sup> grouped; (1,2) as “solar”, (2,3) as “atmospheric” and (1,3) as “reactor”. Many  
<sup>223</sup> neutrino experiments aim to measure the PMNS parameters from a wide array of  
<sup>224</sup> origins, as is the purpose of this thesis.

<sup>225</sup> The Majorana phase,  $\alpha_{1,2}$ , **containing matrix** included within **the fourth matrix**  
<sup>226</sup> **in** Equation 1.8 is only included for completeness. For an oscillation analysis ex-  
<sup>227</sup> periment, **any term in this oscillation probability calculation containing this phase**  
<sup>228</sup> **disappears any terms containing thtis phase disappear** due to taking the expectation  
<sup>229</sup> value of the PMNS matrix. **Measurements of these phases are typically performed**  
<sup>230</sup> **by experiments searching for neutrino-less double  $\beta$ -decay [16].**

<sup>231</sup> A two flavour approximation can be **attained obtained** when one assumes the third  
<sup>232</sup> mass eigenstate is degenerate with another. As discussed in section 1.3, it is found  
<sup>233</sup> that  $\Delta m_{21}^2 \ll |\Delta m_{31}^2|$ . This results in the two flavour approximation being reasonable  
<sup>234</sup> for understanding the features of the oscillation. In this two flavour case, the mixing  
<sup>235</sup> matrix becomes,

$$U_{2 \text{ Flav.}} = \begin{pmatrix} \cos(\theta) & \sin(\theta) \\ -\sin(\theta) & \cos(\theta) \end{pmatrix}. \quad (1.9)$$

<sup>236</sup> This culminates in the oscillation probability,

$$\begin{aligned} P(\nu_\alpha \rightarrow \nu_\alpha) &= 1 - \sin^2(2\theta) \sin^2\left(\frac{\Delta m^2 L}{4E}\right), \\ P(\nu_\alpha \rightarrow \nu_\beta) &= \sin^2(2\theta) \sin^2\left(\frac{\Delta m^2 L}{4E}\right). \end{aligned} \quad (1.10)$$

<sup>237</sup> **For Where**  $\alpha \neq \beta$ . For a fixed neutrino energy, the oscillation probability is a sinusoidal function depending upon the distance over which the neutrino propagates. The <sup>238</sup> frequency and amplitude of oscillation are dependent upon **the ratio of the**  $\Delta m^2 / 4E$  <sup>239</sup> and  $\sin^2 2\theta$ , respectively. **The oscillation probabilities presented thus far assume** <sup>240</sup> **c = 1, where c is the speed of light in vacuum. In more familiar units**, the maximum <sup>241</sup> oscillation probability for a fixed value of  $\theta$  is given at  $L[\text{km}] / E[\text{GeV}] \sim 1.27 / \Delta m^2$ . <sup>242</sup> It is this calculation that determines the best  $L/E$  value for a given experiment to be <sup>243</sup> designed around for measurements of a specific value of  $\Delta m^2$ . <sup>244</sup>

### <sup>245</sup> 1.2.2 The MSW Effect

<sup>246</sup> The theory of neutrino oscillation in a vacuum **is has been** described in subsection 1.2.1. <sup>247</sup> However, the beam neutrinos and atmospheric neutrinos originating from below the <sup>248</sup> horizon propagate through matter in the Earth. The coherent scattering of neutrinos <sup>249</sup> from a material target modifies the Hamiltonian of the system. This results in a change <sup>250</sup> in the oscillation probability. Notably, charged current scattering ( $\nu_e + e^- \rightarrow \nu_e + e^-$ ,

251 propagated by a  $W$  boson) only affects electron neutrinos **compared to whereas** the  
252 neutral current scattering ( $\nu_l + l^- \rightarrow \nu_l + l^-$ , propagated by a  $Z^0$  boson) interacts  
253 through all neutrino flavours equally. In the two-flavour **limit approximation**, the  
254 effective mixing parameter becomes

$$\sin^2(2\theta) \rightarrow \sin^2(2\theta_m) = \frac{\sin^2(2\theta)}{(A/\Delta m^2 - \cos(2\theta))^2 + \sin^2(2\theta)}, \quad (1.11)$$

255 where  $A = 2\sqrt{2}G_F N_e E$ , **with**  $N_e$  is the electron density of the medium and  $G_F$  is  
256 Fermi's constant. It is clear to see that there exists a value of  $A = \Delta m^2 \cos(2\theta)$  for  
257  $\Delta m^2 > 0$  which results in a divergent mixing parameter. This resonance is **due to**  
258 **termed** the Mikheyev-Smirnov-Wolfenstein (MSW) effect (or more colloquially, the  
259 matter resonance) which regenerates the electron neutrino component of the neutrino  
260 flux [17–19]. The density at which the resonance occurs is given by

$$N_e = \frac{\Delta m^2 \cos(2\theta)}{2\sqrt{2}G_F E}. \quad (1.12)$$

261 At densities lower than this critical value, the oscillation probability will be much  
262 closer to that of vacuum oscillation. **For antineutrinos,  $N_e \rightarrow -N_e$  [20].** The reso-  
263 nance occurring from the MSW effect depends on the sign of  $\Delta m^2$ . Therefore, any  
264 neutrino oscillation experiment which observes neutrinos and antineutrinos which  
265 have propagated through matter can have some sensitivity to the ordering of the  
266 neutrino mass eigenstates.

## <sup>267</sup> 1.3 Neutrino Oscillation Measurements

<sup>268</sup> As evidence of beyond standard model physics, the 2015 Nobel Prize in Physics was  
<sup>269</sup> awarded to the Super-Kamiokande (SK) [21] and Sudbury Neutrino Observatory  
<sup>270</sup> (SNO) [22] collaborations for the first definitive observation of solar and atmospheric  
<sup>271</sup> neutrino oscillation [23]. Since then, the field has seen a wide array of oscillation  
<sup>272</sup> measurements from a variety of neutrino sources. As seen in subsection 1.2.1, the  
<sup>273</sup> neutrino oscillation probability is dependent on the ratio of the propagation baseline,  $L$ ,  
<sup>274</sup> to the neutrino energy,  $E$ . It is this ratio that determines the type of neutrino oscillation  
<sup>275</sup> a particular experiment is sensitive to.

<sup>276</sup> As illustrated in Figure 1.1, there are many neutrino sources that span a wide  
<sup>277</sup> range of energies. The least energetic neutrinos are from diffuse supernovae and  
<sup>278</sup> terrestrial neutrinos at  $O(1)$ MeV whereas the most energetic neutrinos originate from  
<sup>279</sup> atmospheric and galactic neutrinos of  $> O(1)$ TeV.

### <sup>280</sup> 1.3.1 Solar Neutrinos

<sup>281</sup> Solar neutrinos are emitted from fusion reaction chains at the center of the Sun. The  
<sup>282</sup> solar neutrino flux, given as a function of neutrino energy for different fusion and  
<sup>283</sup> decay chains, is illustrated in Figure 1.2. Whilst proton-proton fusion generates the  
<sup>284</sup> largest flux of neutrinos, the neutrinos are of low energy and are difficult to reconstruct  
<sup>285</sup> due to the IBD interaction threshold of 1.8MeV. Consequently, most experiments focus  
<sup>286</sup> on the neutrinos from the decay of  $^8B$  (via  $^8B \rightarrow ^8Be^* + e^+ + \nu_e$ ), which are higher  
<sup>287</sup> energy.

<sup>288</sup> The first measurements of solar neutrinos observed a significant reduction in the  
<sup>289</sup> event rate compared to predictions from the Standard Solar Model [26, 27]. The

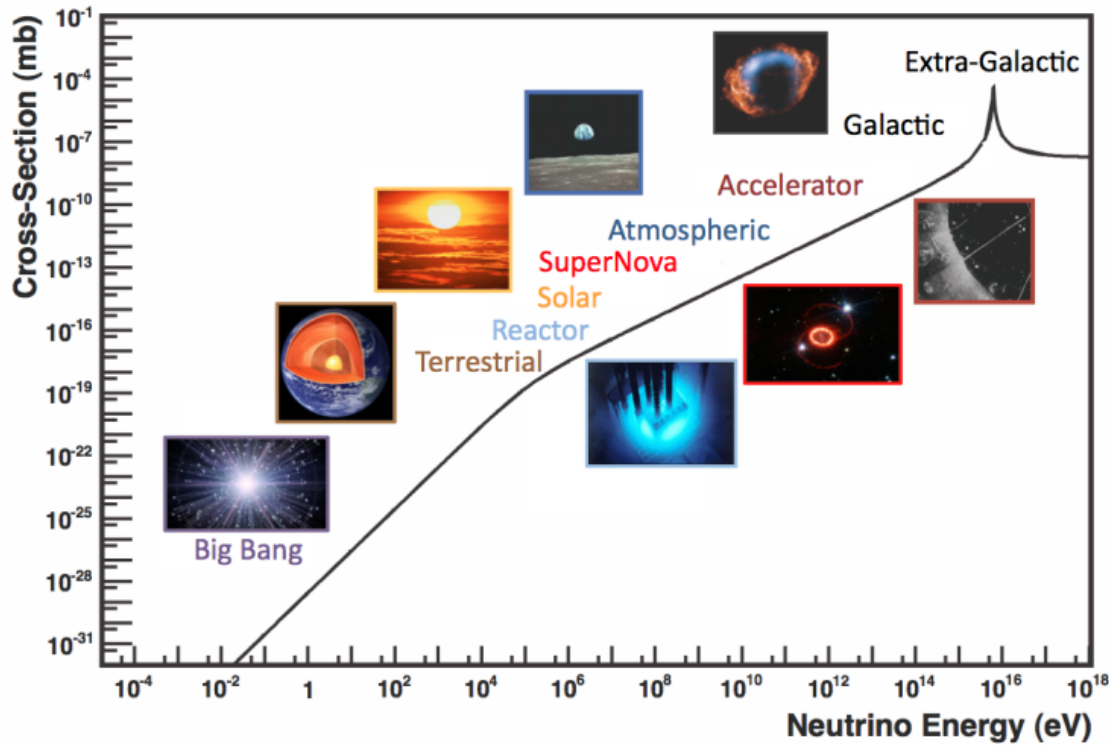


**Figure 1.1:** The cross-section of neutrinos from various natural and man-made sources as a function of neutrino energy. Taken from [24]

290 proposed solution to this “solar neutrino problem” was  $\nu_e \leftrightarrow \nu_\mu$  oscillations in a  
 291 precursory version of the PMNS model [28]. The Kamiokande [29], Gallex [30] and  
 292 Sage [31] experiments confirmed the  $\sim 0.5$  factor deficit of solar neutrinos.

293 The conclusive solution to this problem was determined by the SNO collabora-  
 294 tion [32]. Using a deuterium water target to observe  ${}^8B$  neutrinos, the event rate of  
 295 charged current (CC), neutral current (NC), and elastic scattering (ES) interactions  
 296 (Given in Equation 1.13) was simultaneously measured. CC events can only occur  
 297 for electron neutrinos, whereas the ~~other interaction NC channels are~~ is agnostic  
 298 to neutrino flavour (~~Although , and~~ the ES reaction ~~is more sensitive has a slight~~  
 299 ~~excess sensitivity~~ to electron neutrino interactions). This meant that there were direct  
 300 measurements of the  $\nu_e$  and  $\nu_x$  neutrino flux. It was concluded that the CC and ES  
 301 interaction rates were consistent with the deficit previously observed. Most impor-

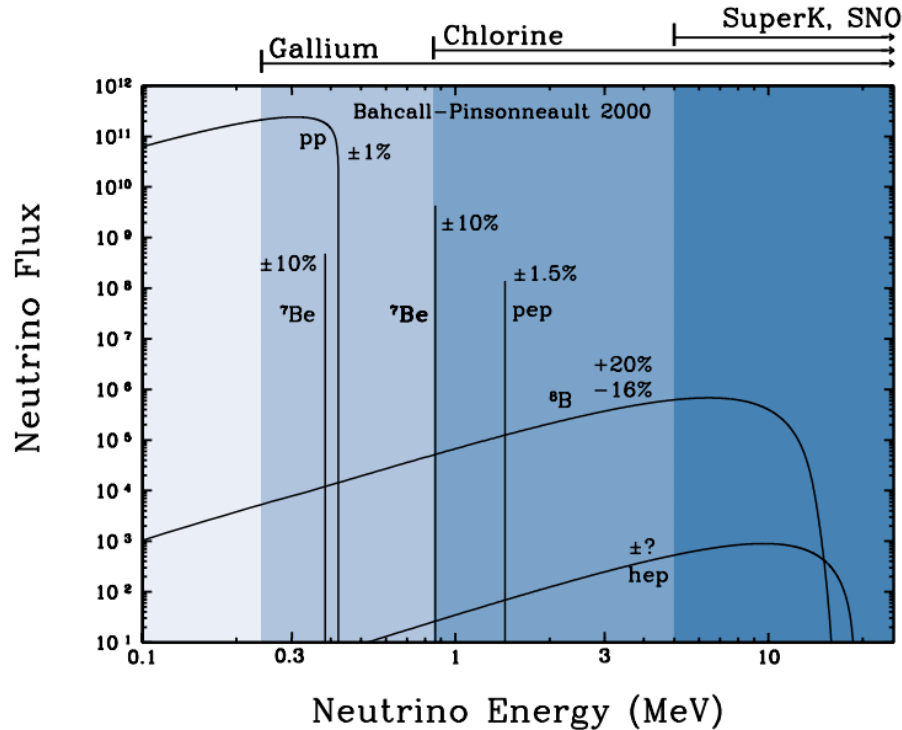
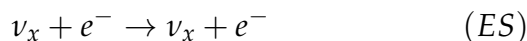
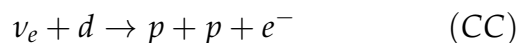


**Figure 1.2:** The solar neutrino flux as a function of neutrino energy for various fusion reactions and decay chains as predicted by the Standard Solar Model. Taken from [25].

tantly, the NC reaction rate was only consistent with the others under the hypothesis of flavour transformation.



Many experiments have since measured the neutrino flux of different interaction chains within the sun [33–35]. The most recent measurement was that of CNO neutrinos which were recently observed with  $5\sigma$  significance by the Borexino collaboration. Future neutrino experiments aim to further these spectroscopic measurements of different fusion chains within the Sun [36–38]. Solar neutrinos act as an irreducible

<sup>309</sup> background for dark matter experiments like DARWIN but oscillation parameter  
<sup>310</sup> measurements can be made [39].

### <sup>311</sup> 1.3.2 Atmospheric Neutrinos

<sup>312</sup> The interactions of primary cosmic ray protons in Earth's upper atmosphere generate  
<sup>313</sup> showers of energetic hadrons. These are mostly pions and kaons which when they  
<sup>314</sup> decay produce a natural source of neutrinos spanning energies of MeV to TeV [40].

<sup>315</sup> **This** The main decay is via

$$\begin{aligned} \pi^\pm &\rightarrow \mu^\pm + (\nu_\mu, \bar{\nu}_\mu) \\ \mu^\pm &\rightarrow e^\pm + (\nu_\mu, \bar{\nu}_\mu) + (\nu_e, \bar{\nu}_e) \end{aligned} \tag{1.14}$$

<sup>316</sup> such that for a single pion decay, three neutrinos are typically produced. The  
<sup>317</sup> atmospheric neutrino flux energy spectra as predicted by the Bartol [41], Honda  
<sup>318</sup> [42–44], and FLUKA [45] models are illustrated in Figure 1.3. The flux distribution  
<sup>319</sup> peaks at an energy of  $O(10)\text{GeV}$ . The uncertainties associated with these models  
<sup>320</sup> are dominated by the hadronic production of kaon and pions as well as the primary  
<sup>321</sup> cosmic flux.

<sup>322</sup> Unlike long-baseline experiments which have a fixed baseline, the distance at-  
<sup>323</sup> mospheric neutrinos propagate is dependent upon the zenith angle at which they  
<sup>324</sup> interact. This is illustrated in Figure 1.4. Neutrinos that are generated directly above  
<sup>325</sup> the detector ( $\cos(\theta) = 1.0$ ) have a baseline equivalent to the height of the atmosphere  
<sup>326</sup> whereas neutrinos that interact directly below the detector ( $\cos(\theta) = -1.0$ ) have to  
<sup>327</sup> travel a length equal to the diameter of the Earth. This means atmospheric neutrinos  
<sup>328</sup> have a baseline that varies from  $O(20)\text{km}$  to  $O(6 \times 10^3)\text{km}$ . Any neutrino generated

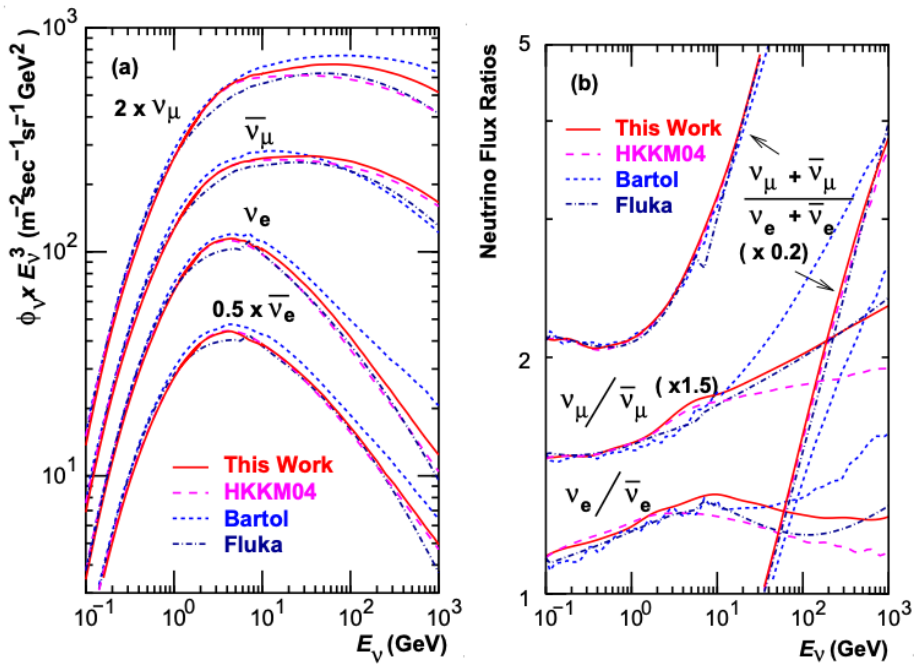


**Figure 1.3:** Left panel: The atmospheric neutrino flux for different neutrino flavours as a function of neutrino energy as predicted by the 2007 Honda model (“This work”) [42], the 2004 Honda model (“HKKM04”) [43], the Bartol model [41] and the FLUKA model [45]. Right panel: The ratio of the muon to electron neutrino flux as predicted by all the quoted models. Both figures taken from [42].

329 at or below the horizon will be subject to matter effects as they propagate through the  
 330 Earth.

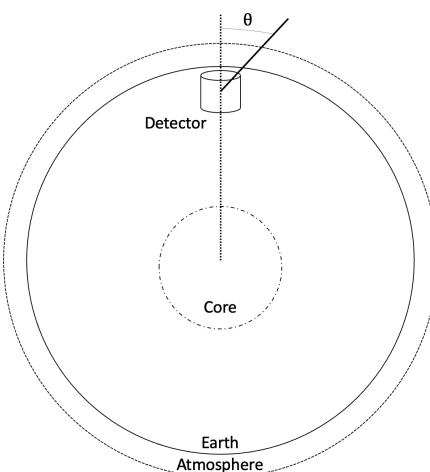


**Figure 1.4:** A diagram illustrating the definition of zenith angle as used in the Super Kamiokande experiment [46].

Figure 1.5 highlights the neutrino flux as a function of the zenith angle for different slices of neutrino energy. For medium to high-energy neutrinos (and to a lesser degree for low-energy neutrinos), the flux is approximately symmetric around  $\cos(\theta) = 0$ . To the accuracy of this approximation, the systematic uncertainties associated with atmospheric flux for comparing upward-going and down-going neutrino cancels. This allows the down-going events, which are mostly insensitive to oscillation probabilities, to act as an unoscillated prediction (similar to a near detector in an accelerator neutrino experiment).

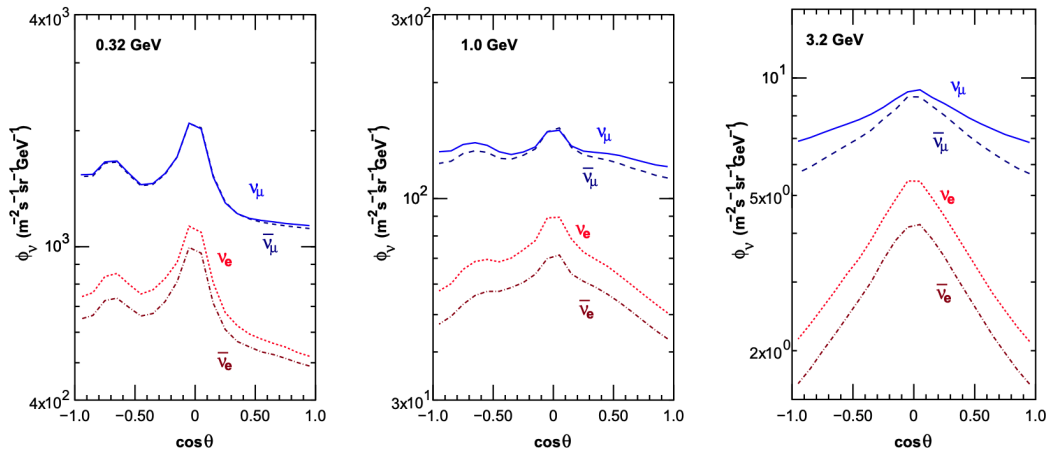


**Figure 1.5:** Prediction of  $\nu_e, \bar{\nu}_e, \nu_\mu, \bar{\nu}_\mu$  fluxes as a function of zenith angle as calculated by the HKKM model [44]. The left, middle and right panels represent three values of neutrino energy, 0.32GeV, 1.0GeV and 3.2GeV respectively. Predictions for other models including Bartol [41], Honda [42] and FLUKA [45] are given in [46].

Precursory hints of atmospheric neutrinos were observed in the mid-1960s searching for  $\nu_\mu + X \xrightarrow{(-)} X^* + \mu^\pm$  [47], although it was called an anomaly at the time of measurement. This was succeeded with the IMB-3 [48] and Kamiokande [49] experiments which measured the ratio of muon neutrinos compared to electron neutrinos  $R(\nu_\mu/\nu_e)$ . Both experiments were found to have a consistent deficit of muon neutrinos, with  $R(\nu_\mu/\nu_e) = 0.67 \pm 0.17$  and  $R(\nu_\mu/\nu_e) = 0.60^{+0.07}_{-0.06} \pm 0.05$ . Super-Kamiokande (SK) [46] extended this analysis by fitting oscillation parameters in  $P(\nu_\mu \rightarrow \nu_\tau)$  which found best fit parameters  $\sin^2(2\theta) > 0.92$  and  $1.5 \times 10^{-3} < \Delta m^2 < 3.4 \times 10^{-3}$  eV<sup>2</sup>.

Since then, atmospheric neutrino experiments have been making precision measurements of the  $\sin^2(\theta_{23})$  and  $\Delta m_{32}^2$  oscillation parameters. Atmospheric neutrino oscillation is dominated by  $P(\nu_\mu \rightarrow \nu_\tau)$ , where SK observed a  $4.6\sigma$  discovery of  $\nu_\tau$  appearance [50]. Figure 1.6 illustrates the current estimates on the atmospheric mixing parameters from a wide range of atmospheric and accelerator neutrino observatories.

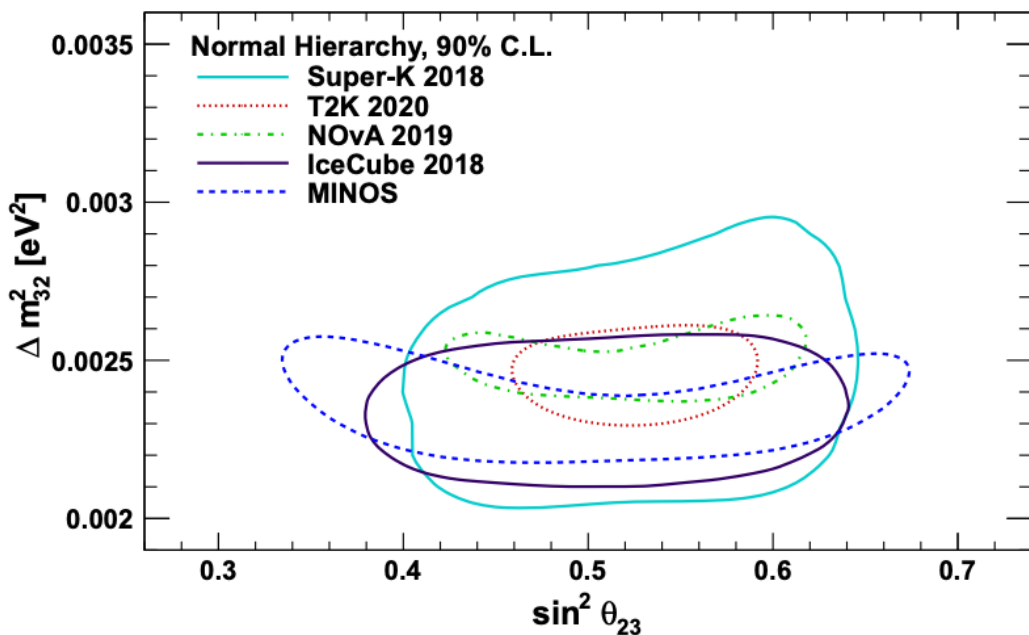


**Figure 1.6:** Constraints on the atmospheric oscillation parameters,  $\sin^2(\theta_{23})$  and  $\Delta m_{32}^2$ , from atmospheric and long baseline experiments: SK [51], T2K [52], NO $\nu$ A [53], IceCube [54] and MINOS [55]. Figure taken from [56].

### 1.3.3 Accelerator Neutrinos

The concept of using a man-made “neutrino beam” was first realised in 1962 [57]. Since then, many experiments have followed which all use the same fundamental concepts. Typically, a proton beam is aimed at a target producing charged mesons that decay to neutrinos. The mesons can be sign-selected by the use of magnetic focusing horns to generate a neutrino or antineutrino beam. Pions are the primary meson that decay and depending on the orientation of the magnetic field, a muon (anti-)neutrino

beam is generated via  $\pi^+ \rightarrow \mu^+ + \nu_\mu$  or  $\pi^- \rightarrow \mu^- + \bar{\nu}_\mu$ . The decay of muons and kaons does result in an irreducible intrinsic electron neutrino background. In T2K, this background contamination is  $O(< 1\%)$  [58]. There is also an approximately  $\sim 5\%$  “wrong-sign” neutrino background of  $\bar{\nu}_\mu$  generated via the same decays. DB: Need to mention that the beam in proton, not antineutrino so the numu flux is higher in the numubar beam

~~The energy of each neutrino in the beam is dependent on the energy of the initial proton beam. Therefore, tuning the proton energy allows Tuning the proton energy in the beam and using beam focusing techniques allows~~ the neutrino energy to be set to a value that maximises the disappearance oscillation probability in the  $L/E$  term in Equation 1.10. This means that accelerator experiments are typically more sensitive to the mixing parameters as compared to a natural neutrino source. However, the disadvantage compared to atmospheric neutrino experiments is that the baseline has to be shorter due to the lower flux. Consequently, there is typically less sensitivity to matter effects and the ordering of the neutrino mass eigenstates.

A neutrino experiment measures

$$R(\vec{x}) = \Phi(E_\nu) \times \sigma(E_\nu) \times \epsilon(\vec{x}) \times P(\nu_\alpha \rightarrow \nu_\beta), \quad (1.15)$$

where  $R(\vec{x})$  is the event rate of neutrinos at position  $\vec{x}$ ,  $\Phi(E_\nu)$  is the flux of neutrinos with energy  $E_\nu$ ,  $\sigma(E_\nu)$  is the cross-section of the neutrino interaction and  $\epsilon(\vec{x})$  is the efficiency **and resolution** of the detector. In order to leverage the most out of an accelerator neutrino experiment, the flux and cross-section systematics need to be constrained. This is typically done via the use of a “near detector”, situated at a baseline

380 of  $O(1)$ km. This detector observes the unoscillated neutrino flux and constrains the  
381 parameters used within the flux and cross-section model.

382 The first accelerator experiments to precisely measure oscillation parameters were  
383 MINOS [59] and K2K [60]. These experiments confirmed the  $\nu_\mu \rightarrow \nu_\mu$  **oscillations**  
384  $\nu_\mu$  **disappearance** seen in atmospheric neutrino experiments by finding consistent  
385 **mixing** parameter values for  $\sin^2(\theta_{23})$  and  $\Delta m_{23}^2$ . The current generation of accelera-  
386 tor neutrino experiments, T2K and NO $\nu$ A extended this field by observing  $\bar{\nu}_\mu \rightarrow \bar{\nu}_e$   
387 and lead the sensitivity to atmospheric mixing parameters as seen in Figure 1.6 [61].  
388 The two experiments differ in their peak neutrino energy, baseline, and detection  
389 technique. The NO $\nu$ A experiment is situated at a baseline of 810km from the NuMI  
390 beamline which delivers 2GeV neutrinos. The T2K neutrino beam is peaked around  
391 0.6GeV and propagates 295km. The NO $\nu$ A experiment also uses functionally iden-  
392 tical detectors (near and far) which allow the approximate cancellation of detector  
393 systematics whereas T2K uses a plastic scintillator technique at the near detector and  
394 a water Cherenkov far detector. The future generation experiments DUNE [62] and  
395 Hyper-Kamiokande [63] will succeed these experiments as the high-precision era of  
396 neutrino oscillation parameter measurements develops.

397 Several anomalous results have been observed in the LSND [9] and MiniBooNE [10]  
398 detectors which were designed with purposefully short baselines. Parts of the neu-  
399 trino community attributed these results to oscillations induced by a fourth “sterile”  
400 neutrino [64] but several searches in other experiments, MicroBooNE [65] and KAR-  
401 MEN [66], found no hints of additional neutrino species. The solution to the anomalous  
402 results **are is** still being determined.

### <sup>403</sup> 1.3.4 Reactor Neutrinos

<sup>404</sup> As illustrated in the first discovery of neutrinos (section 1.1), nuclear reactors are a very  
<sup>405</sup> useful man-made source of electron antineutrinos. For reactors that use low-enriched  
<sup>406</sup> uranium  $^{235}\text{U}$  as fuel, the antineutrino flux is dominated by the  $\beta$ -decay fission of  $^{235}\text{U}$ ,  
<sup>407</sup>  $^{238}\text{U}$ ,  $^{239}\text{Pu}$  and  $^{241}\text{Pu}$  [67] as illustrated in Figure 1.7.

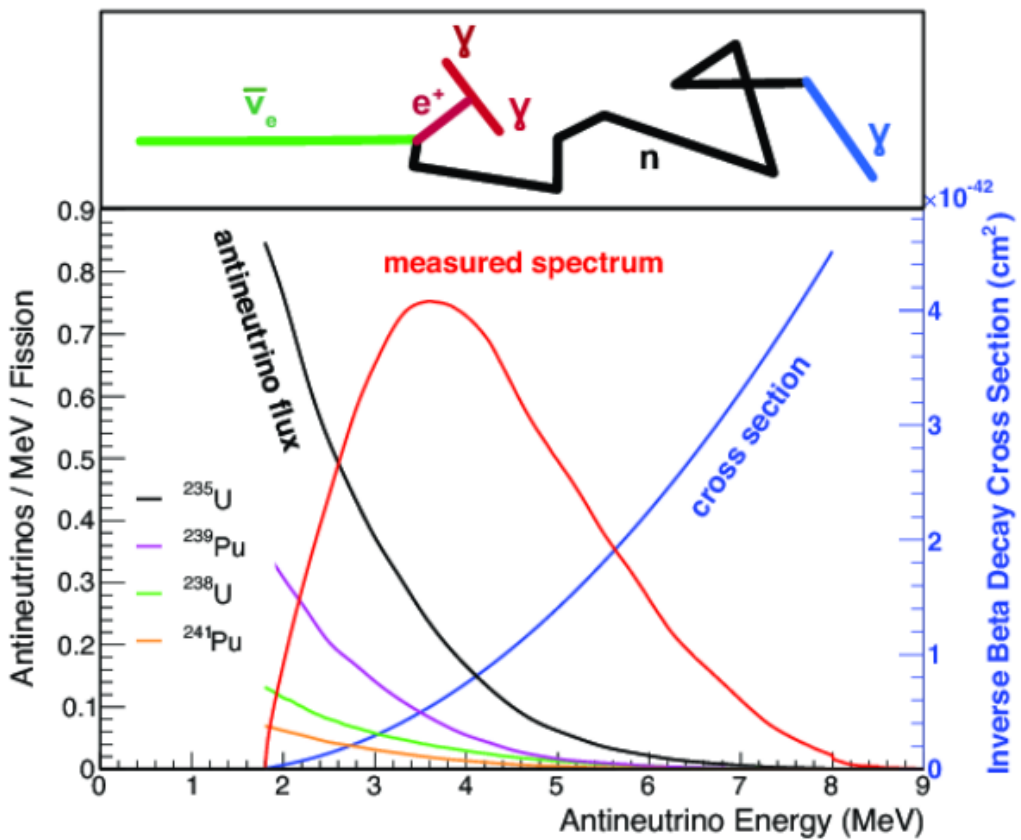


**Figure 1.7:** Reactor electron antineutrino fluxes for  $^{235}\text{U}$  (Black),  $^{238}\text{U}$  (Green),  $^{239}\text{Pu}$  (Purple), and  $^{241}\text{Pu}$  (Orange) isotopes. The inverse  $\beta$ -decay cross-section (Blue) and corresponding measurable neutrino spectrum (Red) are also given. Top panel: Schematic of Inverse  $\beta$ -decay interaction including the eventual capture of the emitted neutron. This capture emits a  $\gamma$ -ray which provides a second signal of the event. Taken from [68].

<sup>408</sup> Due to their low energy, reactor electron antineutrinos predominantly interact  
<sup>409</sup> via the inverse  $\beta$ -decay (IBD) interaction. The typical signature contains two signals  
<sup>410</sup> delayed by  $O(200)\mu\text{s}$ ; firstly the prompt photons from positron annihilation, and

411 secondly the photons emitted ( $E_{tot}^\gamma = 2.2\text{MeV}$ ) from de-excitation after neutron capture  
412 on hydrogen. Searching for both signals improves the detector's ability to distinguish  
413 between background and signal events [69]. Recently, SK included gadolinium dopants  
414 into the ultra-pure water to increase the energy released from the photon cascade to  
415  $\sim 8\text{MeV}$  and reduce the time of the delayed signal to  $\sim 28\mu\text{s}$ .

416 There are many short baseline experiments ( $L \sim O(1)\text{km}$ ) that have measured the  
417  $\sin^2(\theta_{13})$  and  $\Delta m_{23}^2$  oscillation parameters. Daya Bay [70], RENO [71] and Double  
418 Chooz [72] have all provided precise measurements, with the first discovery of a  
419 non-zero  $\theta_{13}$  made by Daya Bay and RENO (and ~~complimented complemented~~ by  
420 T2K [72]). The constraints on  $\sin^2(\theta_{13})$  by the reactor experiments lead the field and  
421 are often used as external inputs to accelerator neutrino experiments to improve their  
422 sensitivity to  $\delta_{CP}$  and mass hierarchy determination. JUNO-TAO [73], a small collabora-  
423 ration within the larger JUNO experiment, is a next-generation reactor experiment that  
424 aims to precisely measure the isotopic antineutrino yields from the different fission  
425 chains. Alongside this, it aims to explain the '5MeV excess' [74–76] by conducting a  
426 search for sterile neutrinos with a mass scale of around 1eV.

427 Kamland [77] is the only experiment to have observed reactor neutrinos using a  
428 long baseline (flux weighted averaged baseline of  $L \sim 180\text{km}$ ) which allows it to have  
429 sensitivity to  $\Delta m_{12}^2$ . Combined with the SK solar neutrino experiment, the combined  
430 analysis puts the most stringent constraint on  $\Delta m_{12}^2$  [78] ~~which is used as a prior~~  
431 ~~uncertainty within accelerator neutrino experiments.~~

432 DB: Include a conclusion section with PDG results

<sup>433</sup> **Chapter 2**

<sup>434</sup> **T2K and SK Experiment Overview**

<sup>435</sup> As the successor of the Kamiokande experiment, the Super-Kamiokande (SK) collaboration has been leading atmospheric neutrino oscillation analyses for over two decades.  
<sup>436</sup> The detector has provided some of the strongest constraints on proton decay **limits** and **as well as** the first precise measurements of the  $\Delta m_{23}^2$  and  $\sin^2(\theta_{23})$  neutrino oscillation parameters. **Despite this, the The** ability of the detector to low-energy neutrino events has been significantly improved with the recent gadolinium doping of the ultra-pure water target. **section 2.1 describes the history, detection technique, and operation of the SK detector. The history, detection technique, and operation of the SK detector is described in section 2.1.**

<sup>444</sup> The Tokai-to-Kamioka (T2K) experiment was one of the first long-baseline experiments to use both neutrino and antineutrino beams to precisely measure the charge parity violation within the neutrino sector. With the SK detector observing the oscillated neutrino flux, the T2K experiment observed the first hints of a non-zero  $\sin^2(\theta_{13})$  measurement and continues to lead the field with the constraints it provides on  $\sin^2(\theta_{13})$ ,  $\sin^2(\theta_{23})$ ,  $\Delta m_{23}^2$  and  $\delta_{CP}$ . **section 2.2 documents the The** techniques which T2K uses in generating its neutrino beam as well as the near-detector used to constrain the flux and cross-section parameters **invoked within the systematic models used in this analysis are documented in section 2.2.**

## <sup>453</sup> 2.1 The Super-Kamiokande Experiment

<sup>454</sup> The SK experiment began taking data in 1996 [79] and has had many modifications  
<sup>455</sup> throughout its lifespan. There have been seven defined periods of data taking as  
<sup>456</sup> noted in Table 2.1. Data taking began in SK-I which ran for five years. Between the  
<sup>457</sup> SK-I and SK-II periods, a significant proportion of the PMTs were damaged during  
<sup>458</sup> maintenance. Those that survived were equally distributed throughout the detector  
<sup>459</sup> in the SK-II era, which resulted in a reduced photo-coverage. From SK-III onwards,  
<sup>460</sup> repairs to the detector meant the full suite of PMTs was operational. Before the  
<sup>461</sup> start of SK-IV, the data acquisition and electronic systems were upgraded. Between  
<sup>462</sup> SK-IV and SK-V, a significant effort was placed into tank open maintenance and  
<sup>463</sup> repair/replacement of defective PMTs, a task for which the author of this thesis was  
<sup>464</sup> required. Consequently, the detector conditions were significantly different between  
<sup>465</sup> the two operational periods. SK-VI saw the start of the 0.01% gadolinium doped  
<sup>466</sup> water. SK-VII, which started during the writing of this thesis, has increased the  
<sup>467</sup> gadolinium concentration to 0.03% for continued operation. [DB: Link to Linyan's talk from Nu2022.](#)

Period	Start Date	End Date	Live-time (days)
I	April 1996	July 2001	1489.19
II	October 2002	October 2005	798.59
III	July 2006	September 2008	518.08
IV	September 2008	May 2018	3244.4
V	January 2019	July 2020	461.02
VI	July 2020	May 2022	583.3
VII	May 2022	Ongoing	N/A

**Table 2.1:** The various SK periods and respective live-time. The SK-VI live-time is calculated until 1<sup>st</sup> April 2022. SK-VII started during the writing of this thesis.

### <sup>469</sup> 2.1.1 The SK Detector

<sup>470</sup> The basic structure of the Super-Kamiokande (SK) detector is a cylindrical tank with a  
<sup>471</sup> diameter 39.3m and height 41.1m filled with ultrapure water [80]. A diagram of the  
<sup>472</sup> significant components of the SK detector is [illustrated given](#) in Figure 2.1. The SK  
<sup>473</sup> detector is situated in the Kamioka mine in Gifu, Japan. The mine is underground with  
<sup>474</sup> roughly 1km rock overburden (2.7km water equivalent overburden) [81]. At this depth,  
<sup>475</sup> the rate of cosmic ray muons is significantly decreased to a value of  $\sim 2\text{Hz}$ . The top of  
<sup>476</sup> the tank is covered with stainless steel which is designed as a working platform for  
<sup>477</sup> maintenance, calibration, and location for high voltage and data acquisition electronics.

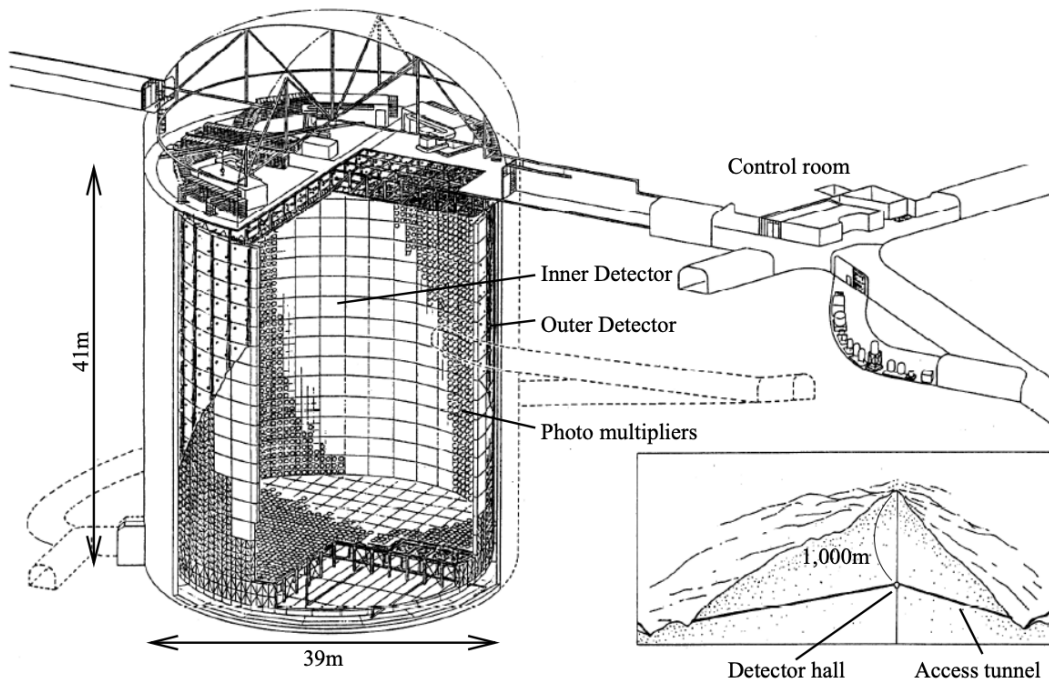


**Figure 2.1:** A schematic diagram of the Super-Kamiokande Detector. Taken from [82].

<sup>478</sup> A smaller cylindrical structure (36.2m diameter, 33.8m height) is situated inside the  
<sup>479</sup> tank, with an approximate 2m gap between this structure and the outer tank wall. The  
<sup>480</sup> purpose of this structure is to support the photomultiplier tubes (PMTs). The volume  
<sup>481</sup> inside and outside the support structure is referred to as the inner detector (ID) and

482 outer detector (OD), respectively. In the SK-IV era, the ID and OD are instrumented  
483 by 11,129 50cm and 1,885 20cm PMTs respectively [80]. The ID contains a 32kton  
484 mass of water. Many analyses performed at SK use a “fiducial volume” defined by the  
485 volume of water inside the ID excluding some distance to the ID wall. This reduces the  
486 volume of the detector which is sensitive to neutrino events but reduces radioactive  
487 backgrounds and allows for better reconstruction performance. The nominal fiducial  
488 volume is defined as the area contained inside 2m from the ID wall for a total of  
489 22.5kton water [83].

490 The two regions of the detector (ID and OD) are optically separated with opaque  
491 black plastic. The purpose of this is to determine whether a track entered or exited  
492 the ID. This allows cosmic ray muons and partially contained events to be tagged and  
493 separated from neutrino events entirely contained within the ID. This black plastic is  
494 also used to cover the area between the ID PMTs to reduce photon reflection from the  
495 ID walls. Opposite to this, the OD is lined with a reflective material to allow photons to  
496 reflect around inside the OD until collected by one of the PMTs. Furthermore, each OD  
497 PMT is backed with  $50 \times 50\text{cm}$  plates of wavelength shifting acrylic which increases  
498 the efficiency of light collection [81].

499 In the SK-IV data-taking period, the photocathode coverage of the detector, or the  
500 fraction of the ID wall instrumented with PMTs, is  $\sim 40\%$  [81]. The PMTs have a  
501 quantum efficiency (the ratio of detected electrons to incident photons) of  $\sim 21\%$  for  
502 photons with wavelengths of  $360\text{nm} < \lambda < 390\text{nm}$ . The proportion of photoelectrons  
503 that produce a signal in the dynode of a PMT, termed the collection efficiency, is  
504  $> 70\%$  [81]. The PMTs used within SK are most sensitive to photons with wavelength  
505  $300\text{nm} \leq \lambda \leq 600\text{nm}$  [81]. One disadvantage of using PMTs as the detection media  
506 is that the Earth’s geomagnetic field can modify its response. Therefore, a set of

compensation coils is built around the inner surface of the detector to mitigate this effect [84].

As mentioned, the SK detector is filled with ultrapure water, which in a perfect world would contain no impurities. However, bacteria and organic compounds can significantly degrade the water quality. This decreases the attenuation length, which reduces the total number of photons that hit a PMT. To combat this, a sophisticated water treatment system has been developed [81, 85]. UV lights, mechanical filters, and membrane degasifiers are used to reduce the bacteria, suspended particulates, and radioactive materials from the water. The flow of water within the tank is also critical as it can remove stagnant bacterial growth or build-up of dust on the surfaces within the tank. Gravity drifts impurities in the water towards the bottom of the tank which, if left uncontrolled, can create asymmetric water conditions between the top and bottom of the tank. Typically, the water entering the tank is cooled below the ambient temperature of the tank to control convection and inhibit bacteria growth. Furthermore, the **rate of** dark noise hits within PMTs is sensitive to the PMT temperature [86] so controlling the temperature gradients within the tank is beneficial for stable measurements.

SK-VI is the first phase of the SK experiment to use gadolinium dopants within the ultrapure water [DB: Link to Linyan's talk at Nu2022](#). As such, the SK water system had to be replaced to avoid removing the gadolinium concentrate from the ultrapure water [87]. For an inverse  $\beta$ -decay (IBD) interaction in a water target, the emitted neutron is thermally captured on hydrogen. This process releases 2.2MeV  $\gamma$  rays which are difficult to detect **due to as the resulting** Compton scattered electrons **from a  $\gamma$  ray of this energy is are** very close to the Cherenkov threshold, limiting the number of photons produced. Thermal capture of neutrons on gadolinium generates  $\gamma$  rays with higher energy (**8MeV [69]**) meaning they are more easily detected. SK-VI has 0.01%

533 Gd loading (0.02% gadolinium sulphate by mass) which causes  $\approx 50\%$  of neutrons  
534 emitted by IBD to be captured on gadolinium [88,89]. Whilst predominantly useful  
535 for low energy analyses, Gd loading allows better  $\nu/\bar{\nu}$  separation for atmospheric  
536 neutrino event selections [90]. Efforts are currently in place to increase the gadolinium  
537 concentrate to 0.03% for  $\approx 75\%$  neutron capture efficiency on gadolinium **DB: Link to**  
538 **Mark's talk at Nu2022**. The final stage of loading targets 0.1% concentrate.

### 539 2.1.2 Calibration

540 The calibration of the SK detector is documented in [80] and summarised below. The  
541 analysis presented within this thesis is dependent upon ‘high energy events’ (Charged  
542 particles with  $O(> 100)\text{MeV}$  momenta). These are events that are expected to generate  
543 a larger number of photons such that each PMT will be hit with multiple photons.  
544 The reconstruction of these events depends upon the charge deposited within each  
545 PMT and the timing response of each individual PMT. Therefore, the most relevant  
546 calibration techniques to this thesis are outlined.

547 Before installation, 420 PMTs were calibrated to have identical charge responses  
548 and then distributed throughout the tank in a cross-shape pattern (As illustrated by  
549 Figure 2.2). These are used as a standardised measure for the rest of the PMTs installed  
550 at similar geometric positions within SK to be calibrated against. To perform this  
551 calibration, a xenon lamp is located at the center of the SK tank which flashes uniform  
552 light at 1Hz. This allows for geometrical effects, water quality variation, and timing  
553 effects to be measured in-situ throughout normal data-taking periods.

554 When specifically performing calibration of the detector (in out-of-data taking  
555 mode), the water in the tank was circulated to avoid top/bottom asymmetric water  
556 quality. Any non-uniformity within the tank significantly affects the PMT hit proba-

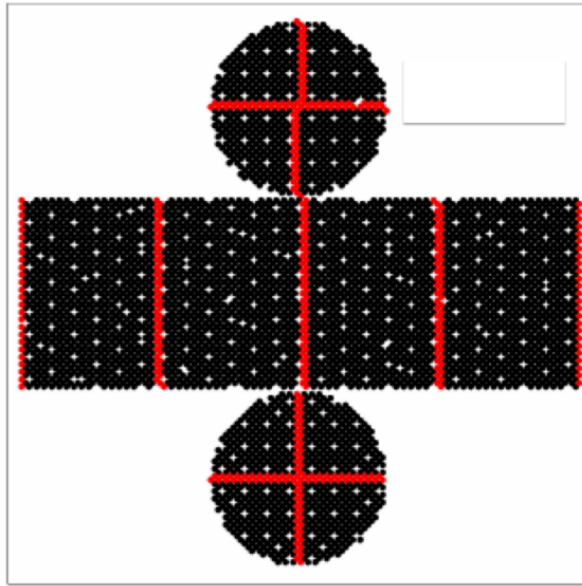


**Figure 2.2:** The location of “standard PMTs” (red) inside the SK detector. Taken from [80].

557     bility through scattering or absorption. This becomes a dominant effect for the very  
 558     low-intensity light sources discussed later which are designed such that only one  
 559     photon is incident upon a given PMT.

560       The “gain” of a PMT is defined as the ratio of the total charge of the signal produced  
 561     compared to the charge of photoelectrons emitted by the photocathodes within the  
 562     PMT. To calibrate the signal of each PMT, the “relative” and “absolute” gain values are  
 563     measured. The relative gain is the variation of gain among each of the PMTs whereas  
 564     the absolute gain is the average gain of all PMTs.

565       The relative gain is calibrated as follows. A laser is used to generate two measure-  
 566     ments: a high-intensity flash that illuminates every PMT with a sufficient number of  
 567     photons, and a low-intensity flash in which only a small number of PMTs collect light.  
 568       The first measurement creates an average charge,  $Q_{obs}(i)$  on PMT  $i$ , whereas the second  
 569     measurement ensures that each hit PMT only generates a single photoelectron. For the  
 570     low-intensity measurement, the number of times each PMT records a charge larger  
 571     than 1/4 photoelectrons,  $N_{obs}(i)$ , is counted. The values measured can be expressed as

$$\begin{aligned} Q_{obs}(i) &\propto I_H \times f(i) \times \epsilon(i) \times G(i), \\ N_{obs}(i) &\propto I_L \times f(i) \times \epsilon(i), \end{aligned} \quad (2.1)$$

572 Where  $I_H$  and  $I_L$  is the intensity of the high and low flashes,  $f(i)$  is the acceptance  
 573 efficiency of the  $i^{\text{th}}$  PMT,  $\epsilon(i)$  is the product of the quantum and collection efficiency  
 574 of the  $i^{\text{th}}$  PMT and  $G(i)$  is the gain of the  $i^{\text{th}}$  PMT. The relative gain for each PMT can  
 575 determined by taking the ratio of these quantities.

576 The absolute gain calibration is performed by observing fixed energy  $\gamma$ -rays of  
 577  $E_\gamma \sim 9\text{MeV}$  emitted isotropically from neutron capture on a NiCf source situated at  
 578 the center of the detector. This generates a photon yield of about 0.004 photoelec-  
 579 trons/PMT/event, meaning that  $> 99\%$  of PMT signals are generated from single  
 580 photoelectrons. A charge distribution is generated by performing this calibration over  
 581 all PMTs, and the average value of this distribution is taken to be the absolute gain  
 582 value.

583 As mentioned in subsection 2.1.1, the average quantum and collection efficiency  
 584 for the SK detector is  $\sim 21\%$  and  $> 70\%$  respectively. However, these values do differ  
 585 between each PMT and need to be calibrated accordingly. Consequently, the NiCf  
 586 source is also used to calibrate the “quantum  $\times$  collection” efficiency (denoted “QE”)  
 587 value of each PMT. The NiCf low-intensity source is used as the PMT hit probability  
 588 is proportional to the QE ( $N_{obs}(i) \propto \epsilon(i)$  in Equation 2.1). A Monte Carlo prediction  
 589 which includes photon absorption, scattering, and reflection is made to estimate the  
 590 number of photons incident on each PMT and the ratio of the number of predicted  
 591 to observed hits is calculated. The difference is attributed to the QE efficiency of that  
 592 PMT. This technique is extended to calculate the relative QE efficiency by normalizing  
 593 the average of all PMTs which removes the dependence on the light intensity.

594 Due to differing cable lengths and readout electronics, the timing response between  
595 a photon hitting the PMT and the signal being captured by the data acquisition can be  
596 different between each PMT. Due to threshold triggers (Described in subsection 2.1.3),  
597 the time at which a pulse reaches a threshold is dependent upon the size of the pulse.  
598 This is known as the ‘time-walk’ effect and also needs to be accounted for in each PMT.  
599 To calibrate the timing response, a pulse of light with width 0.2ns is emitted into the  
600 detector through a diffuser. Two-dimensional distributions of time and pulse height  
601 (or charge) are made for each PMT and are used to calibrate the timing response. This  
602 is performed in-situ **whilst during** data taking with the light source pulsing at 0.03Hz.

603 The top/bottom water quality asymmetry is measured using the NiCf calibration  
604 data and cross-referencing these results to the “standard PMTs”. The water attenuation  
605 length is continuously measured by the rate of vertically-downgoing cosmic-ray  
606 muons which enter via the top of the tank.

### 607 2.1.3 Data Acquisition and Triggering

608 Dark noise is the phenomenon where a PMT registers a pulse that is consistent with a  
609 single photoelectron emitted from photon detection despite the PMT being in complete  
610 darkness. This is predominately caused by two processes. Firstly there is intrinsic  
611 dark noise which is where photoelectrons gain enough thermal energy to be emitted  
612 from the photocathode, and secondly, the radioactive decay of contaminants inside the  
613 structure of the PMT. Typical dark noise rate for PMTs used within SK are  $O(3)$ kHz  
614 [81] **which equates to about 12 dark noise hits per 220ns**. This is lower than the  
615 expected number of photons generated for a ‘high energy event’ (As described in  
616 subsection 2.1.4) but instability in this value can cause biases in reconstruction.

617     The analysis presented in this thesis only uses the SK-IV period of the SK exper-  
 618     iment so this subsection focuses on the relevant points of the data acquisition and  
 619     triggering systems to that SK period. The earlier data acquisition and triggering  
 620     systems are documented in [91, 92].

621     Before the SK-IV period started, the existing front-end electronics were replaced

622     with “QTC-Based Electrons with Ethernet, QBEE” systems [93]. When the QBEE  
 623     observes a signal above a 1/4 photoelectron threshold, the charge-to-time (QTC)

624     converter generates a rectangular pulse. The start of the rectangular pulse indicates

625     the time at which the analog photoelectron signal was received and the width of the

626     pulse indicates the total charge integrated throughout the signal. This is then digitized

627     by time-to-digital converters and sent to the “front-end” PCs. The digitized signal

628     from every QBEE is then chronologically ordered and sent to the “merger” PCs. It is

629     the merger PCs that apply the software trigger. Any triggered events are passed to the

630     “organizer” PC. This sorts the data stream of multiple merger PCs into chronologically

631     ordered events which are then saved to disk. The schematic of data flow from PMTs to

632     disk is illustrated in Figure 2.3.

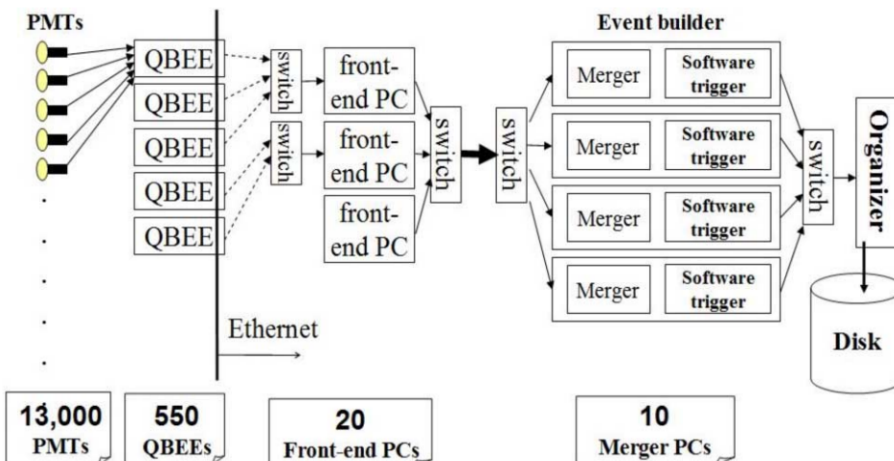


**Figure 2.3:** Schematic view of the data flow through the data acquisition and online system.  
 Taken from [94].

The software trigger (described in [95]) operates by determining the number of PMT hits within a 200ns sliding window,  $N_{200\mu s}$ . This window coincides with the maximum time that a Cherenkov photon would take to traverse the length of the SK tank [92]. For lower energy events that generate fewer photons, this technique is useful for eliminating background processes like dark noise and radioactive decay which would be expected to separate in time. When the value of  $N_{200\mu s}$  exceeds some threshold, a software trigger is issued. There are several trigger thresholds used within the SK-IV period which are detailed in Table 2.2. If one of these thresholds is met, the PMT hits within an extended time window are also read out and saved to disk. In the special case of an event that exceeds the SHE trigger but does not exceed the OD trigger, the AFT trigger looks for delayed coincidences of 2.2MeV gamma rays emitted from neutron capture in a  $535\mu s$  window after the SHE trigger. A similar but more complex “Wideband Intelligent Trigger (WIT)” has been deployed and is described in [96].

Trigger	Acronym	Condition	Extended time window ( $\mu s$ )
Super Low Energy	SLE	>34/31 hits	1.3
Low Energy	LE	>47 hits	40
High Energy	HE	>50 hits	40
Super High Energy	SHE	>70/58 hits	40
Outer Detector	OD	>22 hits in OD	N/A

**Table 2.2:** The trigger thresholds and extended time windows saved around an event which were utilised throughout the SK-IV period. The exact thresholds can change and the values listed here represent the thresholds at the start and end of the SK-IV period.

#### 2.1.4 Cherenkov Radiation

Cherenkov light is emitted from any highly energetic charged particle traveling with relativistic velocity,  $\beta$ , greater than the local speed of light in a medium [97]. Cherenkov light is formed at the surface of a cone with characteristic pitch angle,

$$\cos(\theta) = \frac{1}{\beta n}. \quad (2.2)$$

651 where  $n$  is the refractive index of the medium. Consequently, the Cherenkov  
 652 momentum threshold,  $P_{thres}$ , is dependent upon the mass,  $m$ , of the charged particle  
 653 moving through the **media medium**,

$$P_{thres} = \frac{m}{\sqrt{n^2 - 1}} \quad (2.3)$$

654 For water, where  $n = 1.33$ , the Cherenkov threshold momentum and energy for  
 655 various particles are given in Table 2.3. In contrast,  $\gamma$ -rays are detected indirectly via  
 656 the combination of photons generated by Compton scattering and pair production.  
 657 The threshold for detection in the SK detector is typically higher than the threshold  
 658 for photon production. This is due to the fact that the attenuation of photons in the  
 659 water means that typically  $\sim 75\%$  of Cherenkov photons reach the ID PMTs. Then the  
 660 collection and quantum efficiencies described in subsection 2.1.1 result in the number  
 661 of detected photons being lower than the number of photons which reach the PMTs.

Particle	Threshold Momentum (MeV)	Threshold Energy (MeV)
Electron	0.5828	0.7751
Muon	120.5	160.3
Pion	159.2	211.7
Proton	1070.0	1423.1

**Table 2.3:** The threshold momentum and energy for a particle to generate Cherenkov light in ultrapure water, as calculated in Equation 2.2 in ultrapure water which has refractive index  $n = 1.33$ .

The Frank-Tamm equation [98] describes the relationship between the number of Cherenkov photons generated per unit length,  $dN/dx$ , the wavelength of the photons generated,  $\lambda$ , and the relativistic velocity of the charged particle,

$$\frac{d^2N}{dxd\lambda} = 2\pi\alpha \left(1 - \frac{1}{n^2\beta^2}\right) \frac{1}{\lambda^2}. \quad (2.4)$$

where  $\alpha$  is the fine structure constant. For a 100MeV momentum electron, approximately 330 photons will be produced per centimeter in the  $300\text{nm} \leq \lambda \leq 700\text{nm}$  region which the ID PMTs are most sensitive to [81].

## 2.2 The Tokai to Kamioka Experiment

The Tokai to Kamioka (T2K) experiment is a long-baseline neutrino oscillation experiment located in Japan. Proposed in the early 2000s [99, 100] to replace K2K [101], T2K was designed to observe electron neutrino appearance whilst precisely measuring the oscillation parameters associated with muon neutrino disappearance [102]. The experiment consists of a neutrino beam generated at the Japan Proton Accelerator Research Complex (J-PARC), a suite of near detectors situated 280m from the beam target, and the Super Kamiokande far detector positioned at a 295km baseline. The cross-section view of the T2K experiment is drawn in Figure 2.4.

The T2K collaboration makes world-leading measurements of the  $\sin^2(\theta_{23})$ ,  $\Delta m_{23}^2$ , and  $\delta_{CP}$  oscillation parameters. Improvements in the precision and accuracy of parameter estimates are still being made by including new data samples and developing the models which describe the neutrino interactions and detector responses DB: [Link to Christophe's slides from Nu2022](#). Electron neutrino appearance was first observed

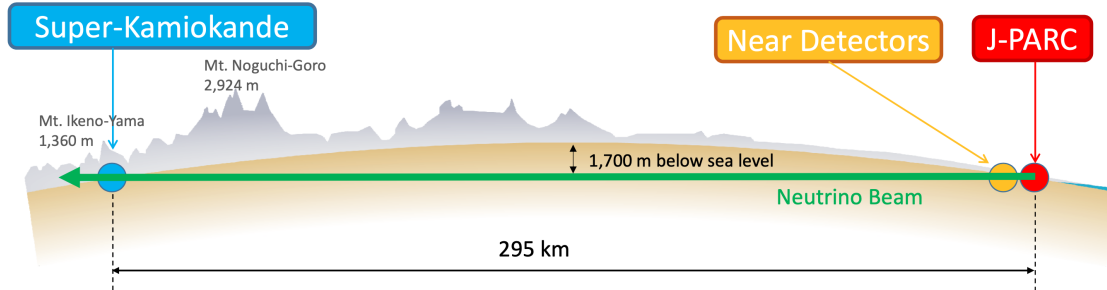


**Figure 2.4:** The cross-section view of the Tokai to Kamioka experiment illustrating the beam generation facility at J-PARC, the near detector situated at a baseline of 280m and the Super Kamiokande far detector situated 295km from the beam target.

682 at T2K in 2014 [103] ~~which accompanied a  $7.3\sigma$  significance of a non-zero  $\sin^2(\theta_{13})$~~   
 683 **measurement with  $7.3\sigma$  significance.**

684 The near detectors provide constraints on the beam flux and cross-section model  
 685 parameters used within the **fit oscillation analysis** by observing the unoscillated  
 686 neutrino beam. There are a host of detectors situated in the near detector hall (As  
 687 illustrated in Figure 2.5): ND280 (subsection 2.2.2), INGRID (subsection 2.2.3), NINJA  
 688 [104], WAGASCI [105], and Baby-MIND [106]. The latter three are not currently used  
 689 within the oscillation analysis presented within this thesis.

690 Whilst this thesis presents the ND280 in terms of its purpose for the oscillation  
 691 analysis, the detector can also make many cross-section measurements at neutrino  
 692 energies of  $O(1)\text{GeV}$  for the different targets within the detector [107, 108]. These  
 693 measurements are of equal importance as they can lead the way in determining the  
 694 model parameters used in the interaction models for the future high-precision era of  
 695 neutrino physics.

### 696 2.2.1 The Neutrino Beam

697 The neutrino beam used within the T2K experiment is described in [58, 109] and  
 698 summarised below. The accelerating facility at J-PARC is composed of two sections; the

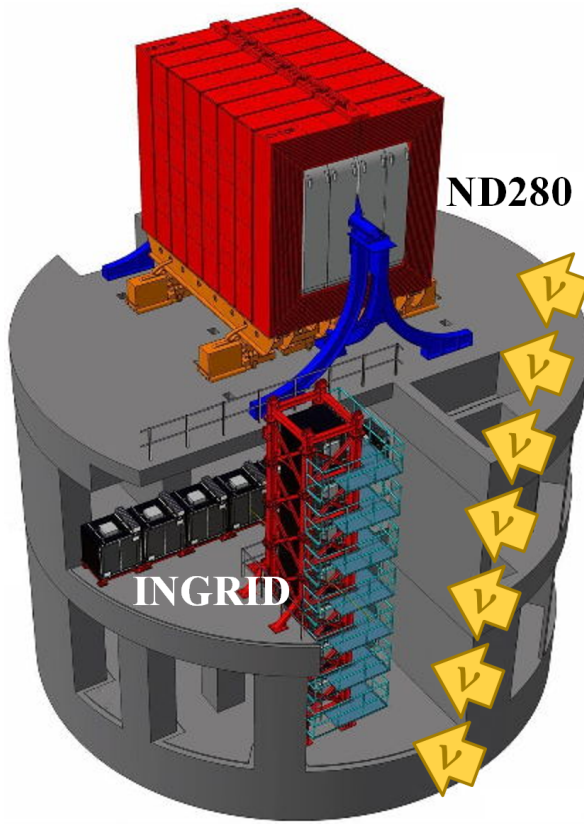
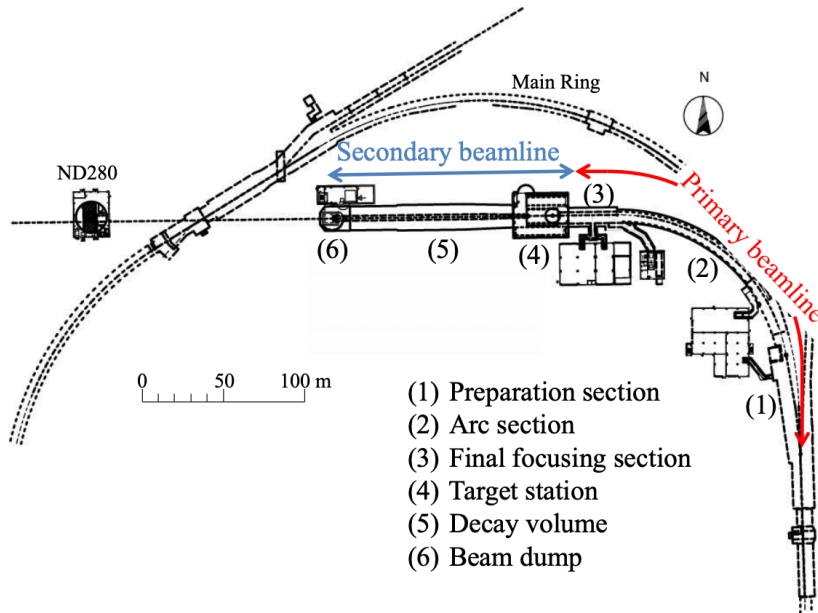


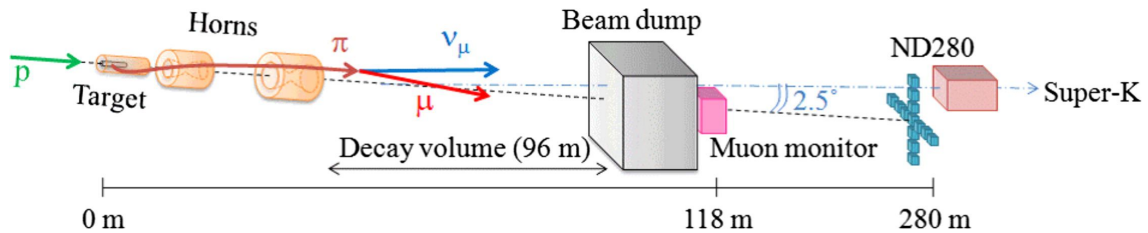
**Figure 2.5:** The near detector suite for the T2K experiment showing the ND280 and INGRID detectors. The distance between the detectors and the beam target is 280m.

699 primary and secondary beamlines. Figure 2.6 illustrates a schematic of the beamline,  
 700 focusing mostly on the components of the secondary beamline. The primary beamline  
 701 has three accelerators that progressively accelerate protons; a linear accelerator, a rapid-  
 702 cycling synchrotron, and the main-ring (MR) synchrotron. Once fully accelerated by  
 703 the MR, the protons have a kinetic energy of 30GeV. Eight bunches of these protons,  
 704 separated by 500ns, are extracted per “spill” from the MR and directed towards a  
 705 graphite target (a rod of length 91.4cm and diameter 2.6cm). Spills are extracted at  
 706 0.5Hz with  $\sim 3 \times 10^{14}$  protons contained per spill.

707 The secondary beamline consists of three main components: the target station, the  
 708 decay volume, and the beam dump. The target station is comprised of the target, beam  
 709 monitors, and three magnetic focusing horns. The proton beam interacts with the  
 710 graphite target to form a secondary beam of mostly pions and kaons. The secondary



(a) Primary and secondary beamline



(b) Secondary beamline

**Figure 2.6:** Top panel: Bird's eye view of the most relevant part of primary and secondary beamline used within the T2K experiment. The primary beamline is the main-ring proton synchrotron, kicker magnet, and graphite target. The secondary beamline consists of the three focusing horns, decay volume, and beam dump. Figure taken from [109]. Bottom panel: The side-view of the secondary beamline including the focusing horns, beam dump and neutrino detectors. Figure taken from [110].

711 beam travels through a 96m long decay volume, generating neutrinos through the  
 712 following decays [58],

$$\begin{aligned}
\pi^+ &\rightarrow \mu^+ + \nu_\mu & \pi^- &\rightarrow \mu^- + \bar{\nu}_\mu \\
K^+ &\rightarrow \mu^+ + \nu_\mu & K^- &\rightarrow \mu^- + \bar{\nu}_\mu \\
&\rightarrow \pi^0 + e^+ + \nu_e & &\rightarrow \pi^0 + e^- + \bar{\nu}_e \\
713 \quad &\rightarrow \pi^0 + \mu^+ + \nu_\mu & &\rightarrow \pi^0 + \mu^- + \bar{\nu}_\mu \\
K_L^0 &\rightarrow \pi^- + e^+ + \nu_e & K_L^0 &\rightarrow \pi^+ + e^- + \bar{\nu}_e \\
&\rightarrow \pi^- + \mu^+ + \nu_\mu & &\rightarrow \pi^+ + \mu^- + \bar{\nu}_\mu \\
\mu^+ &\rightarrow e^+ + \bar{\nu}_\mu + \nu_e & \mu^- &\rightarrow e^- + \nu_\mu + \bar{\nu}_e
\end{aligned}$$

714     The electrically charged component of the secondary beam is focused towards the  
 715   far detector by the three magnetic horns. These horns direct charged particles of a  
 716   particular polarity towards SK whilst defocusing the oppositely charged particles.  
 717   This allows a mostly neutrino or mostly antineutrino beam to be used within the  
 718   experiment, denoted as “forward horn current (FHC)” or “reverse horn current (RHC)”  
 719   respectively.

720     Figure 2.7 illustrates the different contributions to the FHC and RHC neutrino flux.  
 721   The low energy flux is dominated by the decay of pions whereas kaon decay becomes  
 722   the dominant source of neutrinos for  $E_\nu > 3\text{GeV}$ . The “wrong-sign” component,  
 723   which is the  $\bar{\nu}_\mu$  background in a  $\nu_\mu$  beam, and the intrinsic irreducible  $\nu_e$  background,  
 724   are predominantly due to muon decay for  $E_\nu < 2\text{GeV}$ . As the antineutrino **production**  
 725   cross-section is smaller than the neutrino cross-section, the wrong-sign component is  
 726   more dominant in the RHC beam as compared to that in the FHC beam.

727     The beam dump, situated at the end of the decay volume, stops all charged particles  
 728   other than highly energetic muons ( $p_\mu > 5\text{GeV}$ ). The MuMon detector monitors the  
 729   penetrating muons to determine the beam direction and intensity which is used to  
 730   constrain some of the beam flux systematics within the analysis [110, 112].

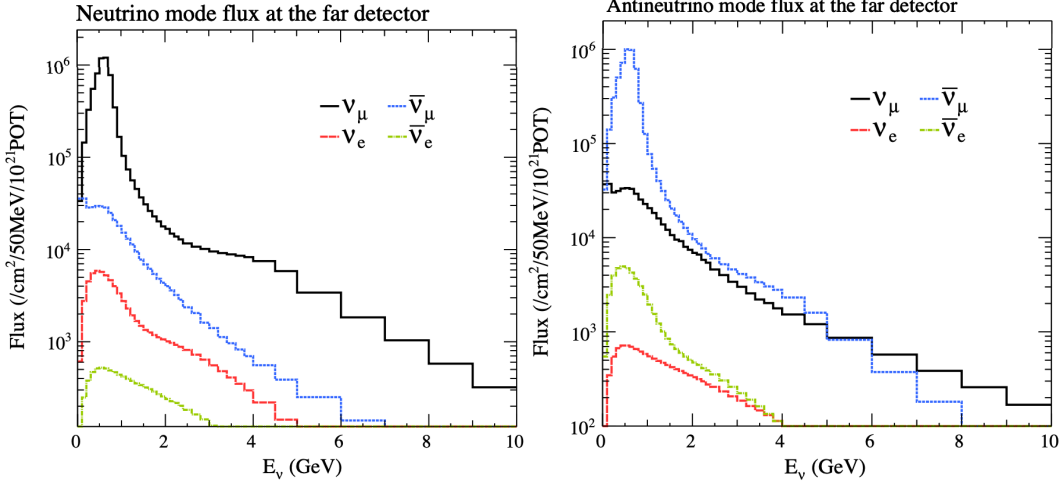


**Figure 2.7:** The Monte Carlo prediction of the energy spectrum for each flavour of neutrino ( $\nu_e$ ,  $\bar{\nu}_e$ ,  $\nu_\mu$  and  $\bar{\nu}_\mu$ ) in the neutrino dominated beam FHC mode (Left) and antineutrino dominated beam RHC mode (Right) expected at SK. Taken from [111].

The T2K experiment uses an off-axis beam to narrow the neutrino energy distribution.

This was the first implementation of this technique in a long-baseline neutrino oscillation experiment after its original proposal [113]. Pion decay,  $\pi \rightarrow \mu + \nu_\mu$ , is a two-body decay. Consequently, the neutrino energy,  $E_\nu$ , can be determined based on the pion energy,  $E_\pi$ , and the angle at which the neutrino is emitted,  $\theta$ ,

$$E_\nu = \frac{m_\pi^2 - m_\mu^2}{2(E_\pi - p_\pi \cos(\theta))}, \quad (2.5)$$

where  $m_\pi$  and  $m_\mu$  are the mass of the pion and muon respectively. For a fixed

energy pion, the neutrino energy distribution is dependent upon the angle at which the neutrinos are observed from the initial pion beam direction. For the 295km baseline at T2K,  $E_\nu = 0.6\text{GeV}$  maximises the electron neutrino appearance probability,  $P(\nu_\mu \rightarrow \nu_e)$ , whilst minimising the muon disappearance probability,  $P(\nu_\mu \rightarrow \nu_\mu)$ . Figure 2.8 illustrates the neutrino energy distribution for a range of off-axis angles, as well as the oscillation probabilities most relevant to T2K.

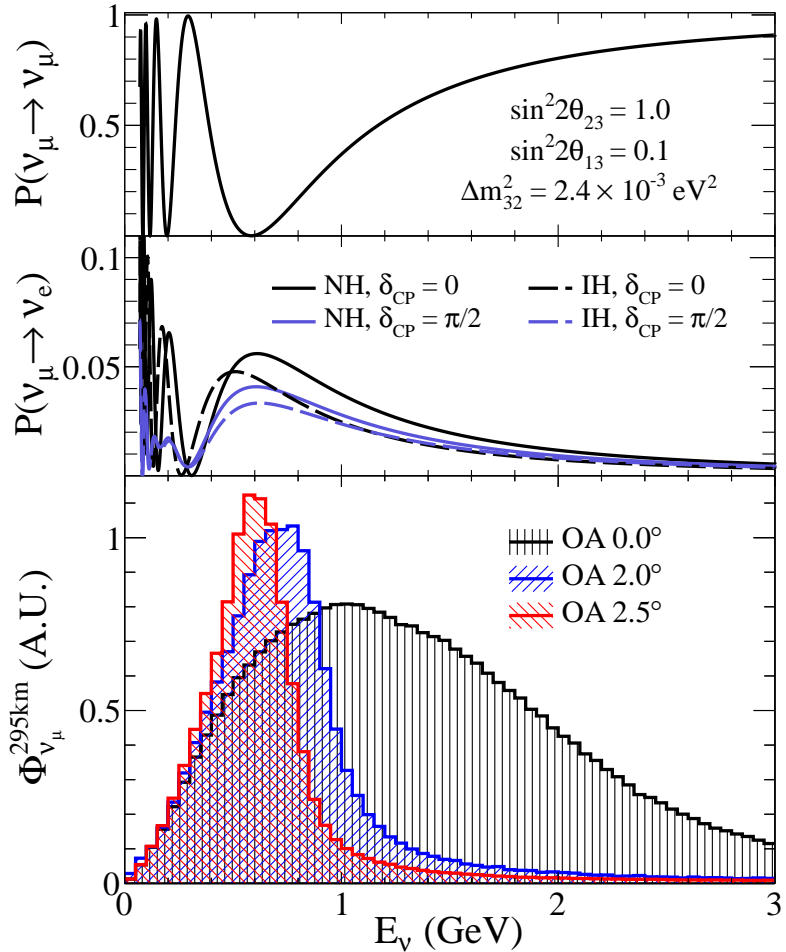


**Figure 2.8:** Top panel: T2K muon neutrino disappearance probability as a function of neutrino energy. Middle panel: T2K electron neutrino appearance probability as a function of neutrino energy. Bottom panel: The neutrino flux distribution for three different off-axis angles (Arbitrary units) as a function of neutrino energy.

### 743 2.2.2 The Near Detector at 280m

744 Whilst all the near detectors are situated in the same “pit” located at 280m from the  
 745 beamline, the “ND280” detector is the off-axis detector which is situated at the same  
 746 off-axis angle as the Super-Kamiokande far detector. It has two primary functions;  
 747 firstly it measures the neutrino flux and secondly it counts the event rates of different  
 748 types of neutrino interactions. Both of these constrain the flux and cross-section  
 749 systematics invoked within the model for a more accurate prediction of the expected  
 750 event rate at the far detector.

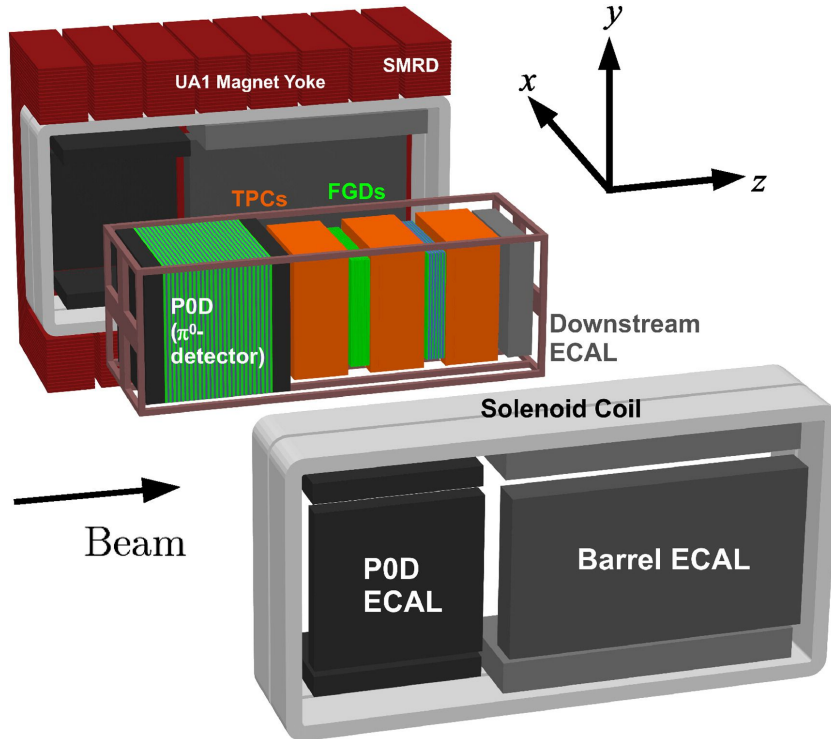


**Figure 2.9:** The components of the ND280 detector. The neutrino beam travels from left to right. Taken from [109].

As illustrated in Figure 2.9, the ND280 detector consists of several sub-detectors.

The most important part of the detector for this analysis is the tracker region. This is comprised of two time projection chambers (TPCs) sandwiched between three fine grain detectors (FGDs). The FGDs contain both hydrocarbon plastics and water targets for neutrino interactions and provide track reconstruction near the interaction vertex. The emitted charged particles can then propagate into the TPCs which provide particle identification and momentum reconstruction. The FGDs and TPCs are further described in subsubsection 2.2.2.1 and subsubsection 2.2.2.2 respectively. The electromagnetic calorimeter (ECAL) encapsulates the tracker region alongside the  $\pi^0$  detector (P0D). The ECAL measures the deposited energy from photons emitted from interactions within the FGD. The P0D constrains the cross-section of neutral current interactions which generate neutral pions, which is one of the largest backgrounds in the electron neutrino appearance oscillation channel. The P0D and ECAL detectors are detailed in subsubsection 2.2.2.3 and subsubsection 2.2.2.4 respectively. The entire

765 detector is located within a large **yolk yoke** magnet which produces a 0.2T magnetic  
766 field. This design of the magnet also includes a scintillating detector called the side  
767 muon range detector (SMRD) which is used to track high-angle muons as well as  
768 acting as a cosmic veto. The SMRD is described in subsubsection 2.2.2.5.

769 **2.2.2.1 Fine Grained Detectors**

770 The T2K tracker region is comprised of two fine grained detectors (FGD) and three  
771 Time Projection Chambers (TPC). A detailed description of the FGD design, construc-  
772 tion, and assembly is found in [114] and summarised below. The FGDs are the primary  
773 target for neutrino interactions with a mass of 1.1 tonnes per FGD. Alongside this,  
774 the FGDs are designed to be able to track short-range particles which do not exit the  
775 FGD. Typically, short-range particles are low momentum and are observed as tracks  
776 that deposit a large amount of energy per unit length. This means the FGD needs  
777 good granularity to resolve these particles. The FGDs have the best timing resolution  
778 ( $\sim 3\text{ns}$ ) of any of the sub-detectors of the ND280 detector. As such, the FGDs are used  
779 for time of flight measurements to **determine distinguish** forward going positively  
780 charged particles from backward going negatively charged particles. Finally, any  
781 tracks which pass through multiple sub-detectors are required to be track matched to  
782 the FGD.

783 Both FGDs are made from square scintillator planes of side length 186cm and  
784 width 2.02cm. Each plane consists of two layers of 192 scintillator bars in an X **or** Y  
785 orientation. A wavelength shifting fiber is threaded through the center of each bar and  
786 is read out by a multi-pixel photon counter (MPPC). FGD1 is the most upstream of  
787 the two FGDs and contains 15 planes of carbon plastic scintillator which is a common  
788 target in external neutrino scattering data. As the far detector is a pure water target, 7  
789 of the 15 scintillator planes in FGD2 have been replaced with a hybrid water-scintillator

target. Due to the complexity of the nucleus, nuclear effects can not be extrapolated between different nuclei. Therefore having the ability to take data on one target which is the same as external data and another target which is the same as the far detector target is beneficial for reliable model parameter estimates.

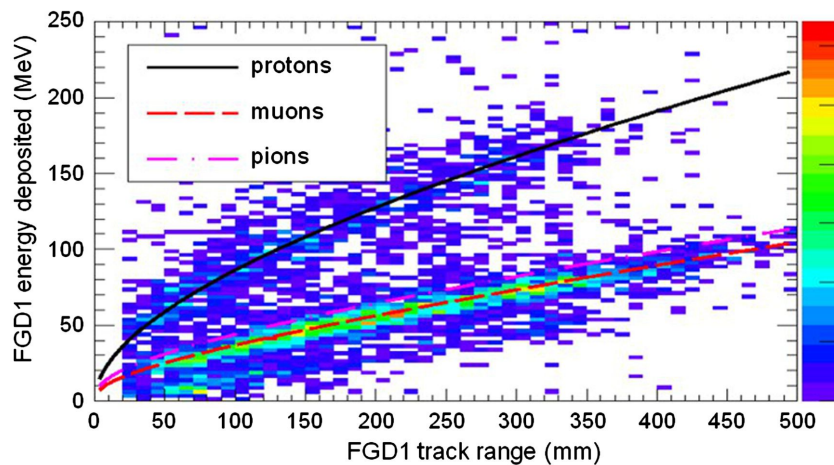


**Figure 2.10:** Comparison of data to Monte Carlo prediction of integrated deposited energy as a function of track length for particles that stopped in FGD1. Taken from [114].

The integrated deposited energy is used for particle identification. The FGD can distinguish protons from other charged particles by comparing the integrated deposited energy from data to Monte Carlo prediction as seen in Figure 2.10.

### 2.2.2.2 Time Projection Chambers

The majority of particle identification and momentum measurements within ND280 are provided by three Time Projection Chambers (TPCs) [115]. The TPCs are located on either side of the FGDs. They are located inside of the magnetic field meaning the momentum of a charged particle can be determined from the bending of the track.

Each TPC module consists of two gas-tight boxes, as shown in Figure 2.11, which are made of non-magnetic material. The outer box is filled with CO<sub>2</sub> which acts as an electrical insulator between the inner box and the ground. The inner box forms

805 the field cage which produces a uniform electric drift field of  $\sim 275\text{V/cm}$  and **is filled**  
 806 **with** an argon gas mixture. Charged particles moving through this gas mixture ionize  
 807 the gas **mixture**. **The and the** ionised charge is drifted towards micromegas detectors  
 808 which measure the ionization charge. The time and position information in the readout  
 809 allows a three-dimensional image of the neutrino interaction.

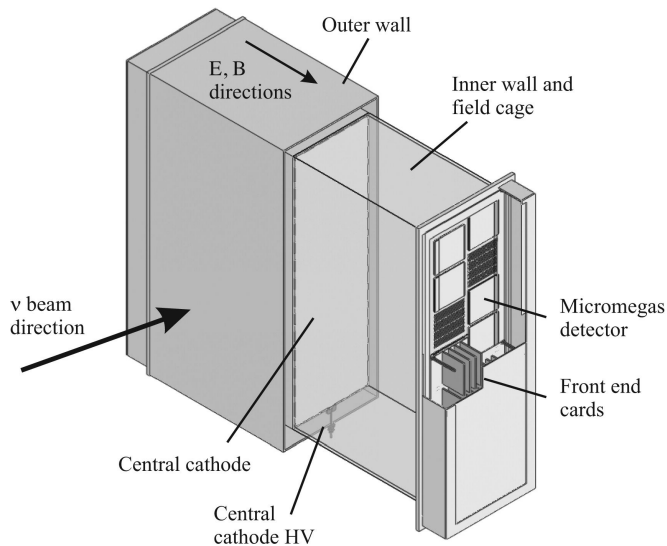
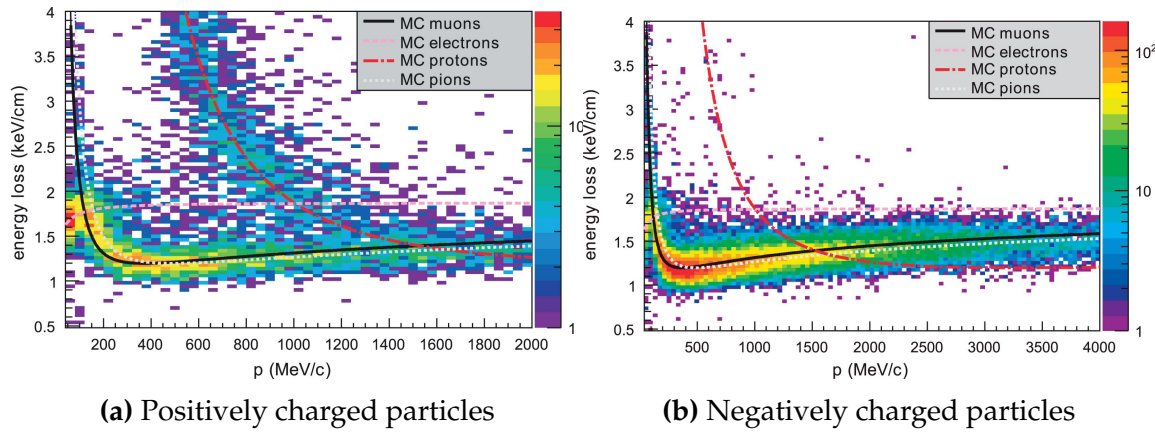


Figure 2.11: Schematic design of a Time Projection Chamber detector. Taken from [115].

810 The particle identification of tracks that pass through the TPCs is performed using  
 811  $dE/dx$  measurements. Figure 2.12 illustrates the data to Monte Carlo distributions  
 812 of the energy lost by a charged particle passing through the TPC as a function of the  
 813 reconstructed particle momentum. The resolution is  $7.8 \pm 0.2\%$  meaning that electrons  
 814 and muons can be distinguished. This allows reliable measurements of the intrinsic  $\nu_e$   
 815 component of the beam.

### 816 2.2.2.3 $\pi^0$ Detector

817 If one of the  $\gamma$ -rays from a  $\pi^0 \rightarrow 2\gamma$  decay is missed at the far detector, the reconstruc-  
 818 tion will determine that event to be **electron-like a charge current  $\nu_e$ -like event**. This  
 819 is one of the main backgrounds hindering the electron neutrino appearance searches.



**Figure 2.12:** The distribution of energy loss as a function of reconstructed momentum for charged particles passing through the TPC, comparing data to Monte Carlo prediction. Taken from [115].

820 Therefore, the  $\pi^0$  detector (P0D) measures the cross-section of the neutral current  
 821 induced neutral pion production on a water target to constrain this background.

822 The P0D is a cube of approximately 2.5m length. The P0D consists of layers of scintillating bars, brass and lead sheets, and water bags as illustrated in  
 823 Figure 2.13. Two electromagnetic calorimeters are positioned at the most upstream  
 824 and most downstream position in the sub-detector and the water target is situated in  
 825 between them. The scintillator layers are built from two triangular bars orientated  
 826 in opposite directions to form a rectangular layer. Each triangular scintillator bar is  
 827 threaded with optical fiber which is read out by MPPCs. The high-Z brass and lead  
 828 regions produce electron showers from the photons emitted in  $\pi^0$  decay.  
 829

830 The sub-detector can generate measurements of NC1 $\pi^0$  cross-sections on a water  
 831 target by measuring the event rate both with and without the water target, with the  
 832 cross-section on a water target being determined as the difference. The total active  
 833 mass is 16.1 tonnes when filled with water and 13.3 tonnes when empty.

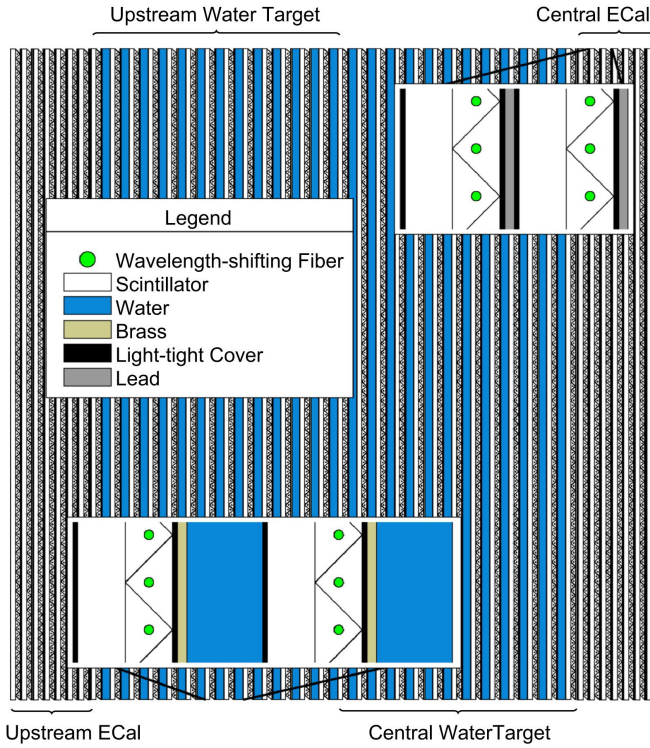


**Figure 2.13:** A schematic of the P0D side-view. Taken from [116].

#### 834 2.2.2.4 Electromagnetic Calorimeter

835 The electromagnetic calorimeter [117] (ECal) encapsulates the P0D and tracking sub-  
 836 detectors. Its primary purpose is to aid  $\pi^0$  reconstruction from any interaction in  
 837 the tracker. To do this, it measures the energy and direction of photon showers from  
 838  $\pi^0 \rightarrow 2\gamma$  decay. It can also distinguish pion and muon tracks depending on the shape  
 839 of the photon shower deposited.

840 The ECal is comprised of three sections; the P0D ECal which surrounds the P0D,  
 841 the barrel ECal which encompasses the tracking region, and the downstream ECal  
 842 which is situated downstream of the tracker region. The barrel and downstream  
 843 ECals are tracking calorimeters that focus on electromagnetic showers from high-angle  
 844 particles emitted from the tracking sub-detectors. Particularly in the TPC, high-angle  
 845 tracks (those which travel perpendicularly to the beam-axis) can travel along a single  
 846 scintillator bar resulting in very few hits. The width of the barrel and downstream

847 ECal corresponds to  $\sim 11$  electron radiation lengths to ensure  ~~$\sim 50\%$  of the energy~~  
848 ~~of the  $\pi^0$  is contained a significant amount of the  $\pi^0$  energy is contained~~. As the  
849 P0D has its own calorimetry which reconstructs showers, the P0D ECal determines  
850 the energy which escapes the P0D.

851 Each ECal is constructed of multiple layers of scintillating bars sandwiched between  
852 lead sheets. The scintillating bars are threaded with optical fiber and read out by  
853 MPPCs. Each sequential layer of the scintillator is orientated perpendicular to the  
854 previous which allows a ~~two-dimensional readout, which when temporal, information is included results in three-dimension event displays three dimensional event displays~~. The target mass of the P0D ECal, barrel ECal, and downstream ECal are 1.50,  
855 4.80 and 6.62 tonnes respectively.  
856

#### 858 2.2.2.5 Side Muon Range Detector

859 As illustrated in Figure 2.9, the ECal, FGDs, P0D, and TPCs are enclosed within the  
860 UA1 magnet. Originally designed for the NOMAD [118] experiment and reconditioned  
861 for use in the T2K experiment [119], the UA1 magnet provides a uniform horizontal  
862 magnetic field of  ~~$0.2 \pm 2 \times 10^{-4}$ T~~  $0.2$ T with an uncertainty of  $2 \times 10^{-4}$ T.

863 Built into the UA1 magnet, the side muon range detector (SMRD) [120] monitors  
864 high-energy muons which leave the tracking region and permeate through the ECal.  
865 It additionally acts as a cosmic muon veto and trigger.

#### 866 2.2.3 The Interactive Neutrino GRID

867 The Interactive Neutrino GRID (INGRID) detector is situated within the same “pit” as  
868 the other near detectors. It is aligned with the beam in the “on-axis” position and mea-  
869 sures the beam direction, spread, and intensity. The detector was originally designed

870 with 16 identical modules [109] (two modules have since been decommissioned) and a  
871 “proton” module. The design of the detector is cross-shaped with length and height  
872  $10\text{m} \times 10\text{m}$  as illustrated in Figure 2.14.

873 Each module is composed of iron sheets interlaced with eleven tracking scintillator  
874 planes for a total target mass of 7.1 tonnes per module. The scintillator design is an X-Y  
875 pattern of 24 bars in both orientations, where each bar contains wave-length shifting  
876 fibers which are connected to multi-pixel photon counters (MPPCs). **The MPPCs con-**  
877 ~~vect detected photons into electrical signals via photodiodes. This is then read out~~  
878 ~~by Trip-T front-end electronics and passed to the readout merging modules along~~  
879 ~~with timing information from the clock module.~~ Each module is encapsulated inside  
880 veto planes to aid the rejection of charged particles entering the module.

881 The proton module is different from the other modules in that it consists of entirely  
882 scintillator planes with no iron target. The scintillator bars are also smaller than those  
883 used in the other modules to increase the granularity of the detector and improve  
884 tracking capabilities. The module sits in the center of the beamline and is designed to  
885 give precise measurements of quasi-elastic charged current interactions to evaluate  
886 the performance of the Monte Carlo simulation of the beamline.

887 The INGRID detector can measure the beam direction to an uncertainty of 0.4mrad  
888 and the beam center within a resolution of 10cm [109]. The beam direction in both the  
889 vertical and horizontal directions is discussed in [121] and it is found to be in good  
890 agreement with the MUMON monitor described in subsection 2.2.1.

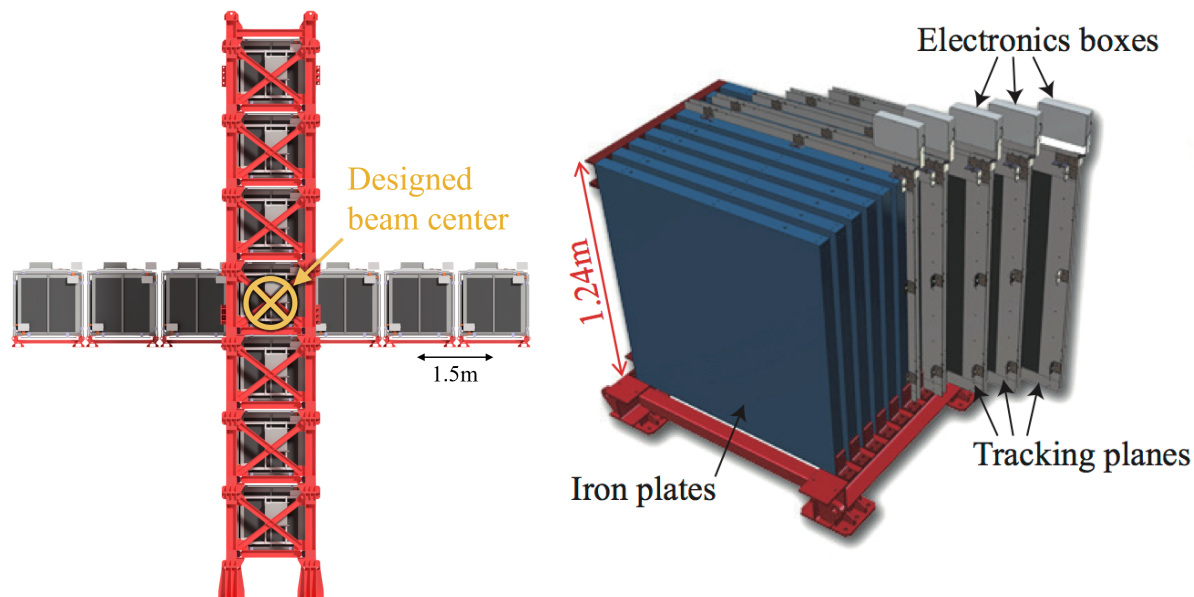


**Figure 2.14:** Left panel: The Interactive Neutrino GRID on-axis Detector. 14 modules are arranged in a cross-shape configuration, with the center modules being directly aligned with the on-axis beam. Right panel: The layout of a single module of the INGRID detector. Both figures are recreated from [109].

891 **Chapter 3**

892 **Bayesian Statistics and Markov Chain  
893 Monte Carlo Techniques**

894 The analysis throughout this thesis is based upon a Bayesian oscillation analysis. To  
895 extract the oscillation parameters, a Markov Chain Monte Carlo (MCMC) method is  
896 used. This chapter explains the theory of how parameter estimates can be determined  
897 using this technique and condenses the material found in the literature [122–125].

898 The oscillation parameter determination presented within this thesis is built upon a  
899 simultaneous fit to the near detector, far detector beam, and atmospheric neutrino data.  
900 In total, there are four oscillation parameters of interest ( $\sin^2(\theta_{23})$  ,  $\sin^2(\theta_{13})$  ,  $\Delta m_{23}^2$  ,  
901 and  $\delta_{CP}$  ), two oscillation parameters to which this study will not be sensitive ( $\sin^2(\theta_{12})$   
902 ,  $\Delta m_{12}^2$  ) and many nuisance parameters that control the systematic uncertainty models  
903 invoked within this study. The systematic uncertainties can be grouped into categories  
904 depending on how they are defined; 574 bin-normalisations due to the near detector  
905 response, 45 bin-normalisations to describe the far detector response to neutrino beam  
906 events, 27 parameters to describe the detector response to atmospheric neutrino events,  
907 100 to model the bin-normalisation due to beam flux uncertainties, 18 which model the  
908 atmospheric flux uncertainties, and 87 to describe the correlated cross-section model.  
909 An alternative parameterisation, where the far detector response is correlated between  
910 the beam and atmospheric samples, replaces the bin-normalisation parameters with  
911 224 shift and smear systematics. Section [DB: Link to Systematics Chapter](#) describes  
912 the systematic model in more depth.

913     The MCMC technique generates a multi-dimensional probability distribution across  
914     all of the model parameters used in the fit. To determine the parameter estimate of a  
915     single parameter, this multi-dimensional object is integrated over all other parameters.  
916     This process is called Marginalisation and is further described in subsection 3.3.1.  
917     Monte Carlo techniques approximate the probability distribution of each parameter  
918     within the limit of generating infinite samples. As ever, generating a large number of  
919     samples is time and resource-dependent. Therefore, an MCMC technique is utilised  
920     within this analysis to reduce the required number of steps to sufficiently sample the  
921     parameter space. This technique is described in further detail in subsection 3.2.1.

## 922     3.1 Bayesian Statistics

923     According to Bayesian Inference, observables and parameters of a statistical model are  
924     treated on an equal footing. To estimate model parameters  $\vec{\theta}$  from some data  $D$ , one  
925     needs to define the joint probability distribution  $P(D|\vec{\theta})$  which can be described as the  
926     prior distribution for model parameters  $P(\vec{\theta})$  and the likelihood of the data given the  
927     model parameters  $P(D|\vec{\theta})$ ,

$$P(D, \vec{\theta}) = P(D|\vec{\theta})P(\vec{\theta}). \quad (3.1)$$

928     The prior distribution,  $P(\vec{\theta})$ , describes all previous knowledge about the parameters  
929     within the model. For example, if the risk of developing health problems is known  
930     to increase with age, the prior distribution would describe the increase. For the  
931     purpose of this analysis, the prior distribution is typically the best-fit values taken  
932     from external data measurements with a Gaussian uncertainty. The prior distribution

can also contain correlations between model parameters. In an analysis using Monte Carlo techniques, the likelihood of measuring some data assuming some set of model parameters is calculated by comparing the Monte Carlo prediction generated at that particular set of model parameters to the data.

It is parameter estimation that is important for this analysis and as such, we apply Bayes' theorem [126]. To calculate the probability for each parameter to have a certain value given the observed data  $P(\vec{\theta}|D)$ , known as the posterior distribution (often termed the posterior). This can be expressed as

$$P(\vec{\theta}|D) = \frac{P(D|\vec{\theta})P(\vec{\theta})}{\int P(D|\vec{\theta})P(\vec{\theta})d\vec{\theta}}. \quad (3.2)$$

The denominator in Equation 3.2 is the integral of the joint probability distribution over all values of all parameters used within the fit. For brevity, we say that the posterior distribution is

$$P(\vec{\theta}|D)\alpha P(D|\vec{\theta})P(\vec{\theta}). \quad (3.3)$$

In subsection 3.3.1, we see that for the cases used within this analysis, it is reasonable to know the posterior to some normalisation constant.

## 3.2 Monte Carlo Simulation

Monte Carlo techniques are used to numerically solve a complex problem that does not necessarily have an analytical solution. These techniques rely on building a large

949 ensemble of samples from an unknown distribution and then using the ensemble to  
950 approximate the properties of the distribution.

951 An example that uses Monte Carlo techniques is to calculate the area underneath  
952 a curve. For example, take the problem of calculating the area under a straight line  
953 with gradient  $M = 0.4$  and intercept  $C = 1.0$ . Analytically, one can calculate the area  
954 under the line is equal to 30 units for  $0 \leq x \leq 10$ . Using Monte Carlo techniques,  
955 one can calculate the area under this line by throwing many random values for the  $x$   
956 and  $y$  components of each sample and then calculating whether that point falls below  
957 the line. The area can then be calculated by the ratio of points below the line to the  
958 total number of samples thrown multiplied by the total area in which samples were  
959 scattered. The study is shown in Figure 3.1 highlights this technique and finds the area  
960 under the curve to be 29.9 compared to an analytical solution of 30.0. The deviation  
961 of the numerical to analytical solution can be attributed to the number of samples  
962 used in the study. The accuracy of the approximation in which the properties of the  
963 Monte Carlo samples replicate those of the desired distribution is dependent on the  
964 number of samples used. Replicating this study with a differing number of Monte  
965 Carlo samples used in each study (As shown in Figure 3.2) highlights how the Monte  
966 Carlo techniques are only accurate within the limit of a high number of samples.

967 Whilst the above example has an analytical solution, these techniques are just as  
968 applicable to complex solutions. Clearly, any numerical solution is only as useful as its  
969 efficiency. As discussed, the accuracy of the Monte Carlo technique is dependent upon  
970 the number of samples generated to approximate the properties of the distribution.  
971 Furthermore, if the positions at which the samples are evaluated are not 'cleverly'  
972 picked, the efficiency of the Monte Carlo technique significantly drops. Given the  
973 example in Figure 3.1, if the region in which the samples are scattered significantly  
974 extends passed the region of interest, many calculations will be calculated but do

not add to the ability of the Monte Carlo technique to achieve the correct result. For instance, any sample evaluated at a  $y \geq 5$  could be removed without affecting the final result. This does bring in an aspect of the ‘chicken and egg’ problem in that to achieve efficient sampling, one needs to know the distribution beforehand.

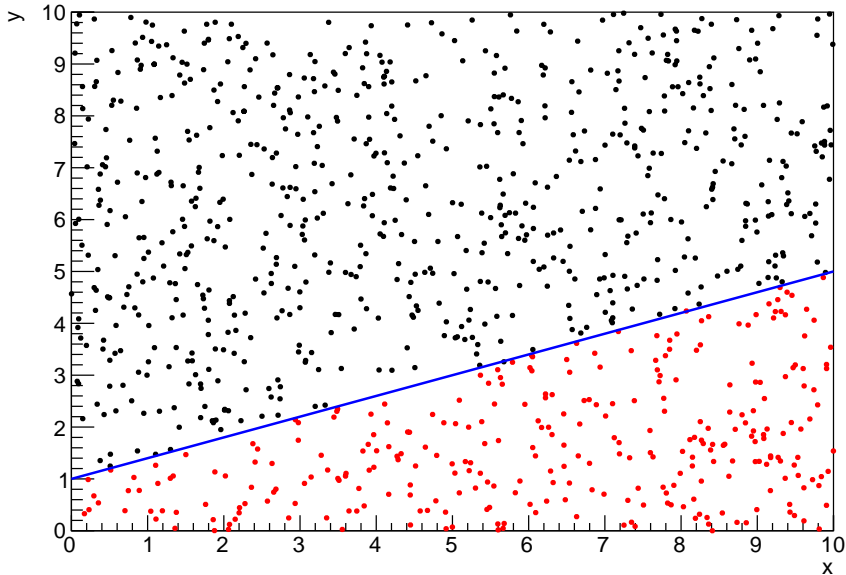


**Figure 3.1:** Example of using Monte Carlo techniques to find the area under the blue line. The gradient and intercept of the line are 0.4 and 1.0 respectively. The area found to be under the curve using one thousand samples is 29.9 units.

### 3.2.1 Markov Chain Monte Carlo

This analysis utilises a multi-dimensional probability distribution, with some dimensions being significantly more constrained than others. This could be from prior knowledge of parameter distributions from external data or un-physical regions in which parameters can not exist. Consequently, the Monte Carlo techniques used need to be as efficient as possible. For this analysis, the Markov Chain Monte Carlo (MCMC) technique is chosen. An MCMC technique is a Monte Carlo technique that uses a Markov chain to select which points at which to sample the parameter distribution.

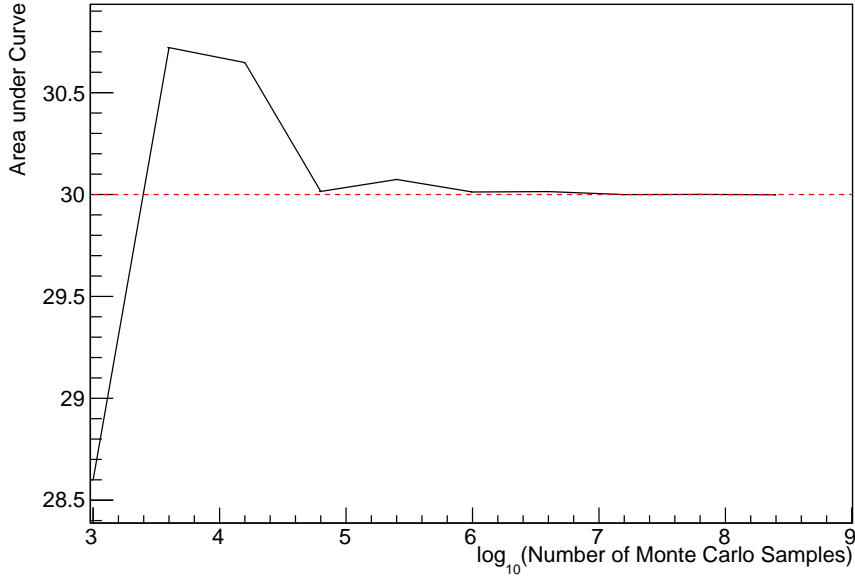


**Figure 3.2:** The area under a line of gradient 0.4 and intercept 1.0 for the range  $0 \leq x \leq 10$  as calculated using Monte Carlo techniques as a function of the number of samples used in each repetition. The analytical solution to the area is 30 units as given by the red line.

987 This technique performs a semi-random stochastic walk through the allowable pa-  
 988 rameter space. This builds a posterior distribution which has the property that the  
 989 density of sampled points is proportional to the probability density of that parame-  
 990 ter. This does mean that the samples produced by this technique are not statistically  
 991 independent but they will cover the space of the distribution.

992 A Markov chain functions by selecting the position of step  $\vec{x}_{i+1}$  based on the  
 993 position of  $\vec{x}_i$ . The space in which the Markov chain selects samples is dependent  
 994 upon the total number of parameters utilised within the fit, where a discrete point in  
 995 this space is described by the N-dimensional space  $\vec{x}$ . In a perfectly operating Markov  
 996 chain, the position of the next step depends solely on the previous step and not on the  
 997 further history of the chain ( $\vec{x}_0, \vec{x}_1$ , etc.). However, in solving the multi-dimensionality  
 998 of the fit used within this analysis, each step becomes correlated with several of  
 999 the steps preceding itself. This behaviour is further explained in subsection 3.2.3.  
 1000 Providing the MCMC chain is well optimised, it will begin to converge towards a

1001 unique stationary distribution. The period between the chain's initial starting point  
1002 and the convergence to the unique stationary distribution is colloquially known as the  
1003 burn-in period. This is discussed further in subsection 3.2.3. Once the chain reaches  
1004 the stationary distribution, all points sampled after that point will look like samples  
1005 from that distribution.

1006 Further details of the theories underpinning MCMC techniques are discussed  
1007 in [123] but can be summarised by the requirement that the chain satisfies the three  
1008 'regularity conditions':

- 1009     • Irreducibility: From every position in the parameter space  $\vec{x}$ , there must exist a  
1010         non-zero probability for every other position in the parameter space to be reached.
- 1011     • Recurrence: Once the chain arrives at the stationary distribution, every step fol-  
1012         lowing from that position must be samples from the same stationary distribution.
- 1013     • Aperiodicity: The chain must not repeat the same sequence of steps at any point  
1014         throughout the sampling period.

1015 The output of the chain after burn-in (ie. the sampled points after the chain  
1016 has reached the stationary distribution) can be used to approximate the posterior  
1017 distribution and model parameters  $\vec{\theta}$ . To achieve the requirement that the unique  
1018 stationary distribution found by the chain be the posterior distribution, one can use  
1019 the Metropolis-Hastings algorithm. This guides the stochastic process depending on  
1020 the likelihood of the current proposed step compared to that of the previous step.  
1021 Implementation and other details of this technique are discussed in subsection 3.2.2.

---

### 1022 3.2.2 Metropolis-Hastings Algorithm

1023 As a requirement for MCMCs, the Markov chain implemented in this technique must  
 1024 have a unique stationary distribution that is equivalent to the posterior distribution.  
 1025 To ensure this requirement and that the regularity conditions are met, this analysis  
 1026 utilises the Metropolis-Hastings (MH) algorithm [127, 128]. For the  $i^{th}$  step in the chain,  
 1027 the MH algorithm determines the position in the parameter space to which the chain  
 1028 moves to based on the current step,  $\vec{x}_i$ , and the proposed step,  $\vec{y}_{i+1}$ . The proposed step  
 1029 is randomly selected from some proposal function  $f(\vec{x}_{i+1}|\vec{x}_i)$ , which depends solely  
 1030 on the current step (ie. not the further history of the chain). The next step in the chain  
 1031  $\vec{x}_{i+1}$  can be either the current step or the proposed step determined by whether the  
 1032 proposed step is accepted or rejected. To decide if the proposed step is selected, the  
 1033 acceptance probability,  $\alpha(\vec{x}_i, \vec{y}_i)$ , is calculated as

$$\alpha(\vec{x}_i, \vec{y}_{i+1}) = \min\left(1, \frac{P(\vec{y}_{i+1}|D)f(\vec{x}_i|\vec{y}_{i+1})}{P(\vec{x}_i|D)f(\vec{y}_{i+1}|\vec{x}_i)}\right). \quad (3.4)$$

1034 Where  $P(\vec{y}_{i+1}|D)$  is the posterior distribution as introduced in section 3.1. To  
 1035 simplify this calculation, the proposal function is required to be symmetric such that  
 1036  $f(\vec{x}_i|\vec{y}_{i+1}) = f(\vec{y}_{i+1}|\vec{x}_i)$ . In practice, a multi-variate Gaussian distribution is used to  
 1037 throw parameter proposals from. This reduces Equation 3.4 to

$$\alpha(\vec{x}_i, \vec{y}_{i+1}) = \min\left(1, \frac{P(\vec{y}_{i+1}|D)}{P(\vec{x}_i|D)}\right). \quad (3.5)$$

1038 After calculating this quantity, a random number,  $\beta$ , is generated uniformly be-  
 1039 tween 0 and 1. If  $\beta \leq \alpha(\vec{x}_i, \vec{y}_{i+1})$ , the proposed step is accepted. Otherwise, the chain  
 1040 sets the next step equal to the current step and this procedure is repeated. This can be  
 1041 interpreted as if the posterior probability of the proposed step is greater than that of  
 1042 the current step, ( $P(\vec{y}_{i+1}|D) \geq P(\vec{x}_i|D)$ ), the proposed step will always be accepted.  
 1043 If the opposite is true, ( $P(\vec{y}_{i+1}|D) \leq P(\vec{x}_i|D)$ ), the proposed step will be accepted  
 1044 with probability  $P(\vec{x}_i|D)/P(\vec{y}_{i+1}|D)$ . This ensures that the Markov chain does not get  
 1045 trapped in any local minima in the potentially non-Gaussian posterior distribution.  
 1046 The outcome of this technique is that the density of steps taken in a discrete region is  
 1047 directly proportional to the probability density in that region.

### 1048 3.2.3 MCMC Optimisation

1049 As discussed in subsection 3.2.2, the proposal function invoked within the MH algo-  
 1050 rithm can take any form and the chain will still converge to the stationary distribution.  
 1051 As discussed in [DB: Link to Analysis Strategy Section](#), this analysis performs the  
 1052 Monte Carlo reweighting on an event-by-event basis. This requires significant com-  
 1053 putational resources to perform a parameter fit. Therefore, the number of steps taken  
 1054 before the unique stationary distribution is found should be minimised as only steps  
 1055 after convergence add information to the fit. Furthermore, the chain should entirely  
 1056 cover the allowable parameter space to ensure that all values have been considered.  
 1057 Tuning the distance that the proposal function jumps between steps on a parameter-  
 1058 by-parameter basis can both minimise the length of the burn-in period and ensure that  
 1059 the correlation between step  $\vec{x}_i$  and  $\vec{x}_j$  is sufficiently small.

1060 The effect of changing the width of the proposal function is highlighted in Figure 3.3.  
 1061 Three scenarios, each with the same underlying stationary distribution (A Gaussian of  
 1062 width 1.0 and mean 0.), are presented. The only difference between the three scenarios

is the width of the proposal function, colloquially known as the ‘step size  $\sigma$ ’. Each scenario starts at an initial parameter value of 10.0 which would be considered an extreme variation. For the case where  $\sigma = 0.1$ , it is clear to see that the chain takes a long time to reach the expected region of the parameter. This indicates that this chain would have a large burn-in period and does not converge to the stationary distribution until step  $\sim 500$ . Furthermore, whilst the chain does move towards the expected region, each step is significantly correlated with the previous. Considering the case where  $\sigma = 5.0$ , the chain approaches the expected parameter region almost instantly meaning that the burn-in period is not significant. However, there are clearly large regions of steps where the chain does not move. This is likely due to the chain proposing steps in the tails of the distribution which have a low probability of being accepted. Consequently, this chain would take a significant number of steps to fully span the allowable parameter region. For the final scenario, where  $\sigma = 0.5$ , you can see a relatively small burn-in period of approximately 100 steps. Once the chain reaches the stationary distribution, it moves throughout the expected region of parameter values many times, sufficiently sampling the full parameter region. This example is a single parameter varying across a continuous distribution and does not fully reflect the difficulties in the many-hundred multi-variate parameter distribution used within this analysis. However, it does give a conceptual idea of the importance of selecting the proposal function and associated step size.

As discussed, step size tuning directly correlates to the average step acceptance rate. If the step size is too small, many steps will be accepted but the chain moves slowly. If the opposite is true, many steps will be rejected as the chain proposes steps in the tails of the distribution. Discussion in [129] suggests that the ‘ideal’ acceptance rate of a high dimension MCMC chain should be approximately  $\sim 25\%$ . An “ideal” step size [129] of

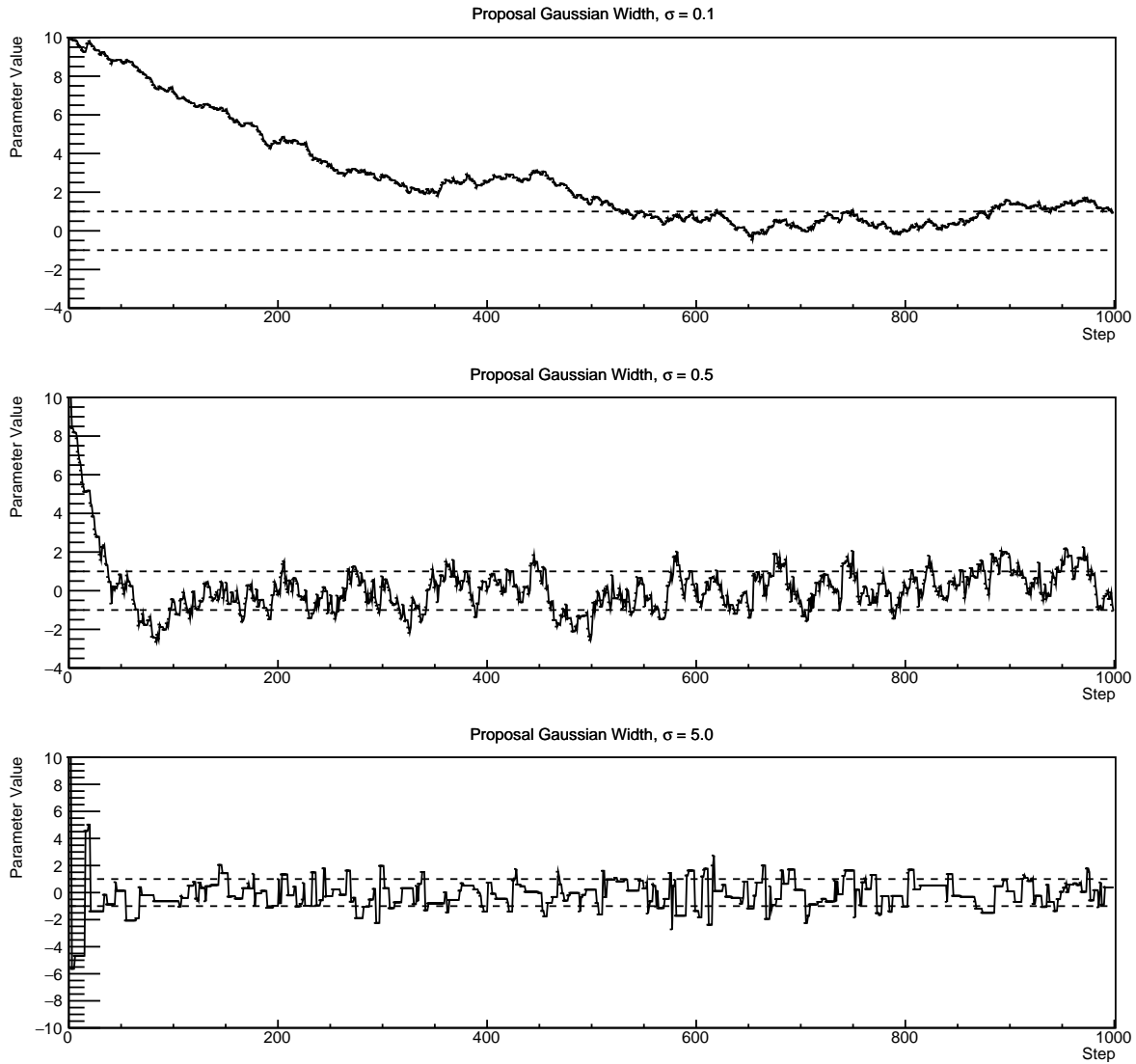


**Figure 3.3:** Three MCMC chains, each with a stationary distribution equal to a Gaussian centered at 0 and width 1 (As indicated by the black dotted lines). All of the chains use a Gaussian proposal function but have different widths (or ‘step size  $\sigma$ ’). The top panel has  $\sigma = 0.1$ , middle panel has  $\sigma = 0.5$  and the bottom panel has  $\sigma = 5.0$ .

$$\sigma = \frac{2.4}{N_p}, \quad (3.6)$$

1089 where  $N_p$  is the number of parameters included in the MCMC fit. However, the  
 1090 complex correlations between systematics mean that some parameters have to be hand

1091 tuned and many efforts have been taken to select a set of parameter-by-parameter step  
1092 sizes to approximately reach the ideal acceptance rate.

1093 Figure 3.3 highlights the likelihood as calculated by the fit in [DB: Link to AsimovA](#)  
1094 [Sensitivity Section](#) as a function of the number of steps in each chain. In practice,  
1095 many independent MCMC chains are run simultaneously to parallelise the task of  
1096 performing the fit. This figure overlays the distribution found in each chain. As seen,  
1097 the likelihood decreases from its initial value and converges towards a stationary  
1098 distribution after  $\sim 1 \times 10^5$  steps. Each fit (whether it be different asimov fits or data  
1099 fit) will have a different set of preferred parameter values which results in a different  
1100 stationary distribution. For each fit presented in this thesis, a burn-in period of  $1 \times 10^5$   
1101 steps was found to be sufficient.

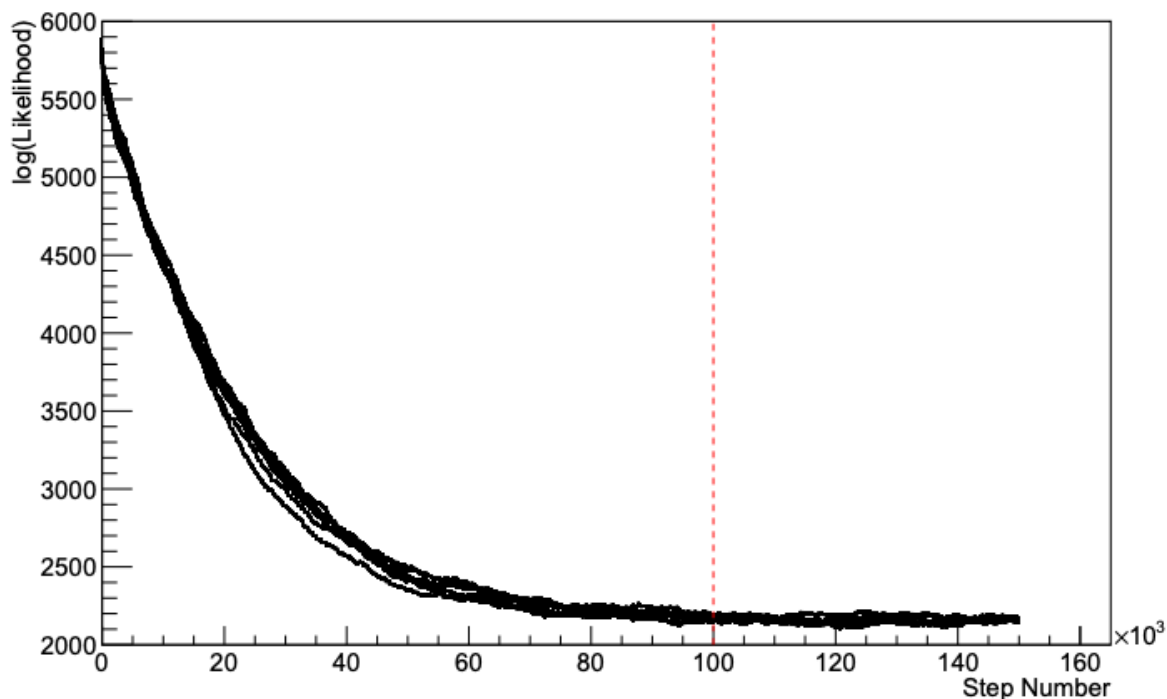


**Figure 3.4:** The log-likelihood from the fit detailed in [DB: Link to AsimovA](#) [Sensitivity Section](#) as a function of the number of steps accumulated in each fit. Many independent MCMC chains were run in parallel and overlaid on this plot. The red line indicates the  $1 \times 10^5$  step burn-in period after which the log-likelihood becomes stable.

## 1102 3.3 Understanding the MCMC Results

1103 Whilst section 3.1 and section 3.2 describe how to interpret Bayesian statistics and  
1104 explains the MCMC techniques used within this analysis, there is no mention of  
1105 how to interpret the output of the chain. The posterior distribution output from the  
1106 chain is a high dimension object, with as many dimensions as there are parameters  
1107 included in the fit. However, this multi-dimensional object is difficult to conceptualize  
1108 so parameter estimations are often presented in one or two-dimensional projections  
1109 of this probability distribution. To do this, we invoke the marginalisation technique  
1110 highlighted in subsection 3.3.1.

### 1111 3.3.1 Marginalisation

1112 The output of the MCMC chain is a highly dimensional probability distribution  
1113 which is very difficult to interpret. From the standpoint of an oscillation analysis  
1114 experiment, the one or two-dimensional ‘projections’ of the oscillation parameters of  
1115 interest are most relevant. Despite this, the best fit values and uncertainties on the  
1116 oscillation parameters of interest should correctly encapsulate the correlations to the  
1117 other systematic uncertainties (colloquially called ‘nuisance’ parameters). For this joint  
1118 beam and atmospheric analysis, the oscillation parameters of interest are  $\sin^2(\theta_{23})$  ,  
1119  $\sin^2(\theta_{13})$  ,  $\Delta m_{23}^2$  , and  $\delta_{CP}$  . All other parameters (Including the oscillation parameter  
1120 this fit is insensitive to) are deemed nuisance parameters. To generate these projections,  
1121 we rely upon integrating the posterior distribution over all nuisance parameters. This  
1122 is called marginalisation. A simple example of this technique is to imagine the scenario  
1123 where two coins are flipped. To determine the probability that the first coin returned  
1124 a ‘head’, the exact result of the second coin flip is disregarded and simply integrated

1125 over. For the parameters of interest,  $\vec{\theta}_i$ , we can calculate the marginalised posterior by  
1126 integrating over the nuisance parameters,  $\vec{\theta}_n$ . In this case, Equation 3.2 becomes

$$P(\vec{\theta}_i|D) = \frac{\int P(D|\vec{\theta}_i, \vec{\theta}_n)P(\vec{\theta}_i, \vec{\theta}_n)d\vec{\theta}_n}{\int P(D|\vec{\theta})P(\vec{\theta})d\vec{\theta}} \quad (3.7)$$

1127 Where  $P(\vec{\theta}_i, \vec{\theta}_n)$  encodes the prior knowledge about the uncertainty and correlations  
1128 between the parameters of interest and the nuisance parameters. In practice, this  
1129 is simply taking the one or two-dimensional projection of the multi-dimensional  
1130 probability distribution.

1131 Whilst in principle an easy solution to a complex problem, correlations between the  
1132 interesting and nuisance parameters can bias the marginalised results. A similar effect  
1133 is found when the parameters being marginalised over have non-Gaussian probability  
1134 distributions. For example, Figure 3.5 highlights the marginalisation bias in the  
1135 probability distribution found for a parameter when requiring a correlated parameter  
1136 to have a positive parameter value. Due to the complex nature of this oscillation  
1137 parameter fit presented in this thesis, there are certainly correlations occurring between  
1138 the oscillation parameters of interest and the other nuisance parameters included in  
1139 the fit.

### 1140 3.3.2 Parameter Estimation and Credible Intervals

1141 The purpose of this analysis is to determine the best fit values for the oscillation  
1142 parameters that the beam and atmospheric samples are sensitive to;  $\sin^2(\theta_{23})$ ,  $\sin^2(\theta_{13})$   
1143,  $\Delta m_{23}^2$ , and  $\delta_{CP}$ . Typically, the results presented take the form of one or two-dimension  
1144 marginalised probability distributions for the appearance ( $\sin^2(\theta_{13})$  and  $\delta_{CP}$ ) and

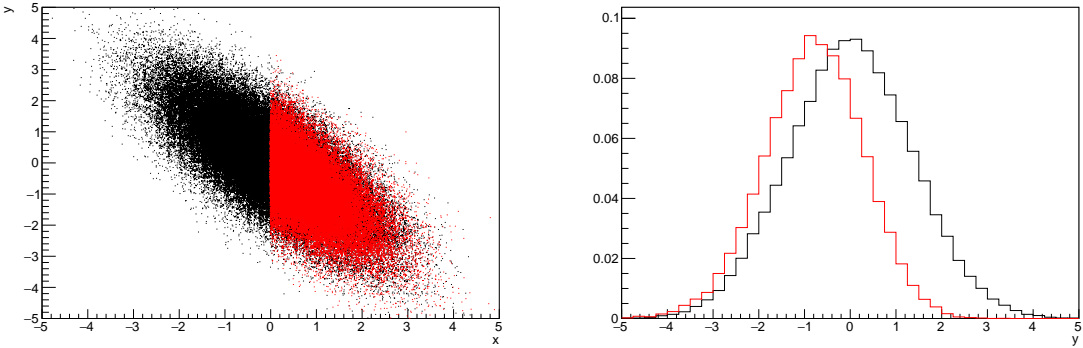


**Figure 3.5:** Left: The two dimensional probability distribution for two correlated parameters  $x$  and  $y$ . The red distribution shows the two dimensional probability distribution when  $0 \leq x \leq 5$ . Right: The marginalised probability distribution for the  $y$  parameter found when requiring the  $x$  to be bound between  $-5 \leq x \leq 5$  and  $0 \leq x \leq 5$  for the black and red distribution, respectively.

1145 disappearance ( $\sin^2(\theta_{23})$  and  $\Delta m_{23}^2$ ) parameters. The posterior probability density  
 1146 taken from the output MCMC chain is binned in these parameters. The parameter  
 1147 best-fit point is then taken to be the value that has the highest posterior probability.  
 1148 This is performed in both one and two-dimensional projections.

1149 However, the single best-fit point in a given parameter is not of much use on its  
 1150 own. We would also like to determine the uncertainty, or credible interval, on that  
 1151 best-fit point. The definition of the  $1\sigma$  credible interval is that we have 68% belief that  
 1152 the parameter is within those bounds. For a more generalised definition, the credible  
 1153 interval is the region of the posterior distribution that contains a specific fraction of  
 1154 the total probability, such that

$$\int P(\theta|D)d\theta = \alpha \quad (3.8)$$

1155 Where  $\theta$  is the parameter on which we calculate the credible interval. This technique  
 1156 then calculates the  $\alpha \times 100\%$  credible interval.

In practice, this analysis uses the highest posterior density (HPD) credible intervals which are calculated through the following method. First, the probability distribution is area-normalised such that it has an integrated area equal to 1.0. The bins of probability are then summed from the highest to lowest until the sum exceeds the  $1\sigma$  level (0.68 in this example). This process is repeated for a range of credible intervals, notably the  $1\sigma$ ,  $2\sigma$  and  $3\sigma$  along with other levels where the critical values for each level can be found in [130]. This process can be repeated for the two-dimensional probability distributions by creating two-dimensional contours of credible intervals rather than a one-dimensional result.

### 3.3.3 Application of Bayes' Theorem

Due to the matter resonance, this analysis has some sensitivity to the mass hierarchy of neutrino states (whether  $\Delta m_{23}^2$  is positive or negative) and the octant of  $\sin^2(\theta_{23})$ . The Bayesian approach utilised within this analysis gives an intuitive method of model comparison by determining which hypothesis is most favourable. Taking the ratio of Equation 3.3 for the two hypotheses of normal hierarchy,  $NH$ , and inverted hierarchy,  $IH$ , gives

$$\frac{P(\vec{\theta}_{NH}|D)}{P(\vec{\theta}_{IH}|D)} = \frac{P(D|\vec{\theta}_{NH})}{P(D|\vec{\theta}_{IH})} \times \frac{P(\vec{\theta}_{NH})}{P(\vec{\theta}_{IH})}. \quad (3.9)$$

The middle term defines the Bayes factor which is a data-driven interpretation of how strong the data prefers one hierarchy to the other. For this analysis, equal priors on both mass hierarchy hypotheses are chosen ( $P(\vec{\theta}_{NH}) = P(\vec{\theta}_{IH}) = 0.5$ ). In practice, the MCMC chain proposes a value of  $|\Delta m_{23}^2|$  and then applies a 50% probability that the value is sign flipped. Consequently, the Bayes factor can be calculated from

1178 the ratio of the probability density in either hypothesis. This equates to counting the  
1179 number of steps taken in the normal and inverted hierarchies and taking the ratio. The  
1180 same approach can be taken to compare the upper octant (UO) compared to the lower  
1181 octant (LO) hypothesis of  $\sin^2(\theta_{23})$ .

1182 Whilst the value of the Bayes factor should always be shown, the Jeffreys scale [131]  
1183 (highlighted in Table 3.1) gives an indication of the strength of preference for one model  
1184 compared to the other. Other interpretations of the strength of preference of a model  
1185 exist, e.g. the Kass and Raferty Scale [132].

$\log_{10}(B_{AB})$	$B_{AB}$	Strength of Preference
< 0.0	< 1	No preference for hypothesis A (Supports hypothesis B)
0.0 – 0.5	1.0 – 3.16	Preference for hypothesis A is weak
0.5 – 1.0	3.16 – 10.0	Preference for hypothesis A is substantial
1.0 – 1.5	10.0 – 31.6	Preference for hypothesis A is strong
1.5 – 2.0	31.6 – 100.0	Preference for hypothesis A is very strong
> 2.0	> 100.0	Decisive preference for hypothesis A

**Table 3.1:** Jeffreys scale for strength of preference for two models  $A$  and  $B$  as a function of the calculated Bayes factor ( $B_{AB} = B(A/B)$ ) between the two models [131]. The original scale is given in terms of  $\log_{10}(B(A/B))$  but converted to linear scale for easy comparison throughout this thesis.

### 1186 3.3.4 Comparison of MCMC Output to Expectation

1187 Whilst not important for the extraction of oscillation parameters, understanding how  
1188 the data constrains the model parameters is important to the understanding of this  
1189 analysis. A simple method of doing this is to perform a comparison in the fitting  
1190 parameters (For instance, the reconstructed neutrino energy and lepton direction for  
1191 T2K far detector beam samples) of the spectra generated by the MCMC chain to ‘data’.  
1192 This ‘data’ could be true data or some variation of Monte Carlo prediction. This allows  
1193 easy comparison of the MCMC probability distribution to the data. To perform this,  $N$

1194 steps from the post burn-in MCMC chain are randomly selected (Where for all plots  
1195 of this style in this thesis,  $N = 3000$ ). From these, the Monte Carlo prediction at each  
1196 step is generated by reweighting the model parameters to the values specified at that  
1197 step. Due to the probability density being directly correlated with the density of steps  
1198 in a certain region, parameter values close to the best fit value are most likely to be  
1199 selected.

1200 In practice, for each bin of the fitting parameters has a probability distribution  
1201 of event rates, with one entry per sampled MCMC step. This distribution is binned  
1202 where the bin with the highest probability is selected as the mean and an error on  
1203 the width of this probability distribution is calculated using the approach highlighted  
1204 in subsection 3.3.2. Consequently, the best fit distribution in the fit parameter is not  
1205 necessarily that which would be attained by reweighting the Monte Carlo prediction  
1206 to the most probable parameter values.

1207 A similar study can be performed to illustrate the freedom of the model parameter  
1208 space prior to the fit. This can be done by throwing parameter values from the prior  
1209 uncertainty of each parameter. This becomes troublesome for parameters with no  
1210 prior uncertainty as the range is technically infinite. Where applicable solutions to  
1211 remove these have been addressed.

# 1212 Chapter 4

## 1213 **Simulation, Reconstruction and Event Se- 1214 lections**

### 1215 4.1 Simulation

1216 In order to generate a Monte Carlo prediction of the expected event rate at the far  
1217 detector for both sets of samples, all the processes in the beamline, atmospheric flux,  
1218 neutrino interaction, and detector need to be modeled. The beamline simulation  
1219 consists of three distinct parts; initial hadron interaction modeling, target station  
1220 geometry and particle tracking and hadronic re-interactions. These are modeled by  
1221 FLUKA [133], JNUBEAM [134, 135], and GCALOR [136], respectively. FLUKA is  
1222 not very adaptable but matches external cross-section measurements in the region of  
1223 interest better than GCALOR ( $O(10)$ GeV). Thus a small simulation is built to model  
1224 the interactions in the target and the output is then passed to JNUBEAM and GCALOR  
1225 for propagation. The hadronic interactions are tuned to data from the NA61/SHINE  
1226 [137–139] and HARP [140] experiments. The tuning is done by reweighting the FLUKA  
1227 and GCALOR predictions to match the external data multiplicity and cross-section  
1228 measurements, based on final state particle kinematics [141]. The predicted flux for  
1229 neutrino and antineutrino beam modes is illustrated in Figure 2.7.

1230 The atmospheric neutrino flux predictions are simulated by the HKKM model  
1231 [42, 44], where the primary cosmic ray flux is tuned to AMS [142] and BESS [143]

external data assuming the US-standard atmosphere '76 [144] density profile and includes geomagnetic field effects. Secondary interactions of pions and muons are handled by DPMJET-III [145] for energies above 32GeV and JAM [44, 146] for energies below that value. These hadronic interactions are tuned to external data [147, 148] using the same methodology as the tuning of the beamline simulation. The energy and cosine zenith predictions of  $\nu_e, \bar{\nu}_e, \nu_\mu, \bar{\nu}_\mu$  flux are given in Figure 1.3 and Figure 1.5, respectively. The flux is approximately symmetrical and peaked around  $\cos(\theta_Z) = 0.0$ . This is because horizontally-going pions and kaons can travel further than their vertically-going counterparts resulting in a larger probability of decay to neutrinos. The symmetry is broken in low-energy neutrinos due to geomagnetic effects, which modify the track of the primary cosmic rays.

The neutrino interactions in all three detectors are simulated with NEUT [149, 150]. This simulates quasi-elastic (QE), meson exchange (MEC), single meson production (PROD), coherent pion production (COH), and deep inelastic scattering (DIS) interactions. These interaction categories can be further broken down by whether they were propagated via a  $W^\pm$  boson in Charged Current (CC) interactions or via a  $Z^0$  boson in Neutral Current (NC) interactions. CC interactions have a charged lepton in the final state, which can be flavour-tagged in reconstruction to determine the flavour of the neutrino. In contrast, NC interactions have a neutrino in the final state so no flavour information can be determined from the observables in the detector. This is the reason why NC events are assumed to not oscillate within the analysis. Both CC and NC interactions are modeled for all the above interaction categories, other than MEC interactions which are only modeled for CC events. The SK detector is only sensitive to charged particles, so all charged current interactions are simulated whilst only neutral current processes that produce charged mesons (NCDIS, NCCOH, and NCPROD) are modeled. NC MEC interactions can only produce charged particles through secondary re-interactions which is a low cross-section process.

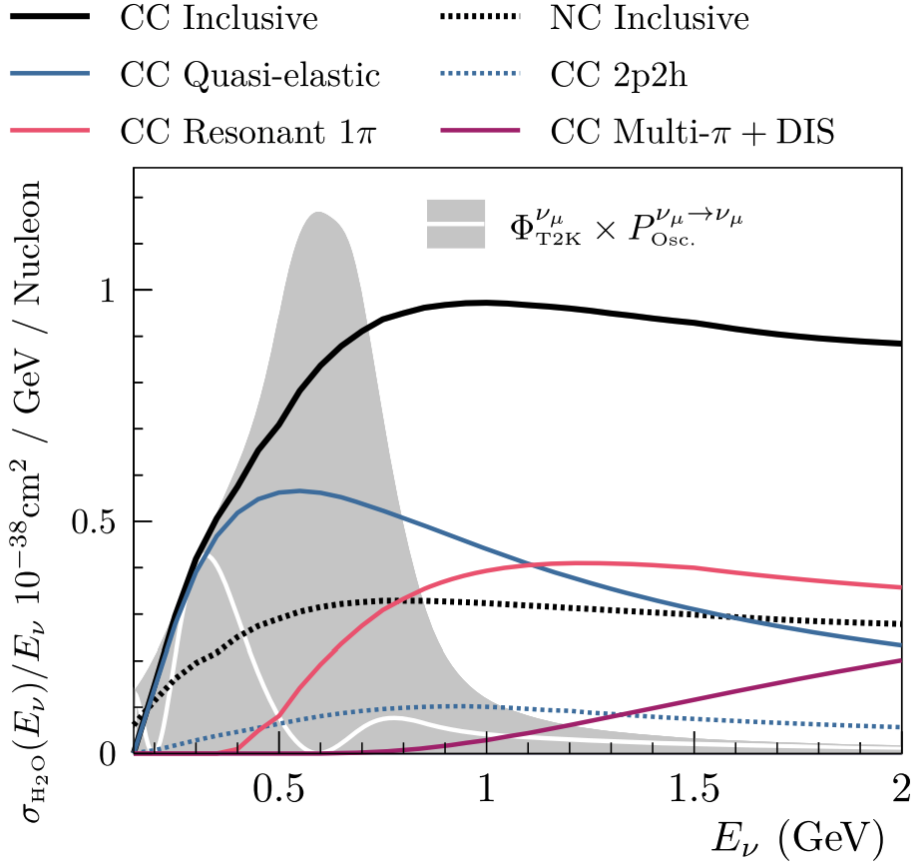


**Figure 4.1:** The NEUT prediction of the  $\nu_\mu$ -H<sub>2</sub>O cross-section overlaid on the T2K  $\nu_\mu$  flux. The charged current (black, solid) and neutral current (black, dashed) inclusive, charged current quasi-elastic (blue, solid), charged current 2p2h (blue, dashed), charged current single pion production (pink), and charged current multi- $\pi$  and DIS (Purple) cross-sections are illustrated. Taken from [149].

As illustrated in Figure 4.1, QE interactions dominate the low-energy cross-section of neutrino interactions. The NEUT implementation adopts the Llewellyn Smith [151] model for neutrino-nucleus interactions, where the nuclear ground state of any bound nucleons (neutrino-oxygen interactions) is approximated by a spectral-function [152] model that simulates the effects of Fermi momentum and Pauli blocking. The cross-section of QE interactions are controlled by vector and axial-vector form factors parameterised by the BBBA05 [153] model and a dipole form factor with  $M_A^{QE} = 1.21 \text{ GeV}$  fit to external data [154], respectively. QE interactions only account for single-nucleon interactions whereas multi-nucleon interactions (or MEC) can contribute significantly to the overall cross-section. NEUT implements the Valencia [155] model

1269 to simulate MEC events, where two nucleons and two holes in the nuclear target are  
1270 produced (Often called 2p2h interactions due to this effect).

1271 For neutrinos of energy  $O(1)\text{GeV}$ , PROD interactions become dominant. These  
1272 predominantly produce charged and neutral pions although  $\gamma$ , kaon, and  $\eta$  production  
1273 is also considered. To simulate these interactions, the Berger-Sehgal [156] model is  
1274 implemented within NEUT. It simulates the excitation of a nucleon from a neutrino  
1275 interaction, production of an intermediate baryon, and the consequential decay to a  
1276 single meson or  $\gamma$ . Pions can also be produced through COH interactions, which occur  
1277 when the incoming neutrino interacts with the entire oxygen nuclei target leaving a  
1278 single pion outside of the nucleus. NEUT utilises the Berger-Sehgal [157] model to  
1279 simulate these interactions.

1280 DIS and multi- $\pi$  producing interactions become the most dominant for energies  
1281  $> O(5)\text{GeV}$ . PYTHIA [158] is used to simulate any interaction with invariant mass,  
1282  $W > 2\text{GeV}/c^2$ , which produces at least one meson. For any interaction which produces  
1283 at least two mesons but has  $W < 2\text{GeV}/c^2$ , the Bronner model is invoked [159].  
1284 Both of these models use Parton distribution functions based on the Bodek-Yang  
1285 model [160–162].

1286 Any pion which is produced within the nucleus can re-interact through final state  
1287 interactions before it exits, as illustrated by the scattering, absorption, production, and  
1288 exchange interactions in Figure 4.2. These re-interactions alter the observable particles  
1289 within the detector. For instance, if the charged pion from a CC PROD interaction  
1290 is absorbed, the observables would mimic a CC QE interaction. To simulate these  
1291 effects, NEUT uses a semi-classical intranuclear cascade model [149]. This cascade  
1292 functions by stepping the pion through the nucleus in fixed-length steps equivalent  
1293 to  $dx = R_N/100$ , where  $R_N$  is the radius of the nucleus. At each step, the Monte  
1294 Carlo allows the pion to interact through scattering, charged exchange, absorption, or

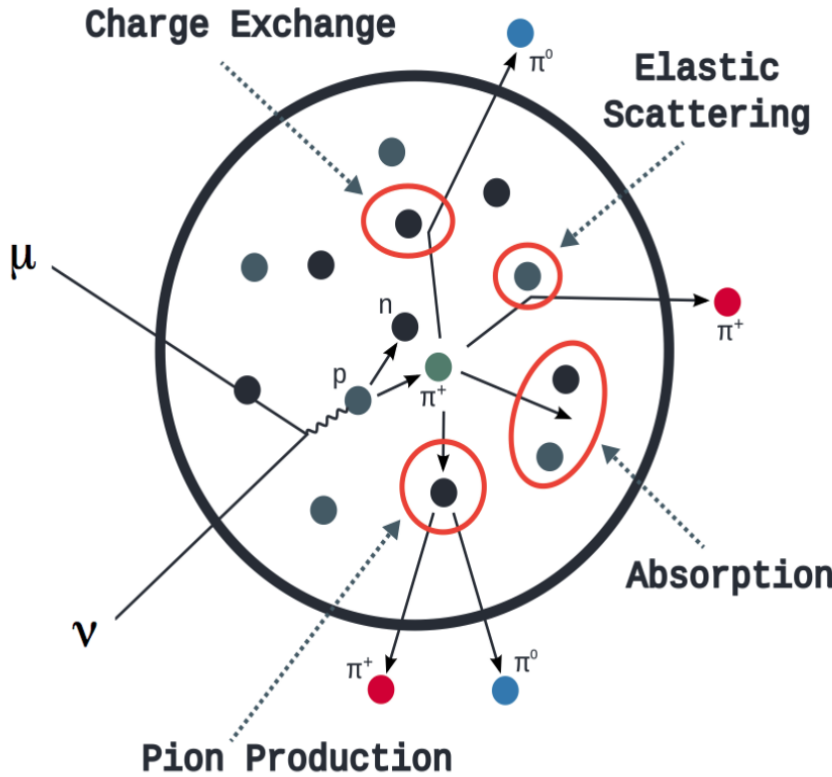


**Figure 4.2:** Illustration of the various processes which a pion can undergo before exiting the nucleus. Taken from [163].

1295 production with an interaction-dependent probability calculated from a fit to external  
 1296 data [164]. This cascade continues until the pion is absorbed or exits the nucleus.

1297 Once the outgoing particle kinematics have been determined from NEUT, they  
 1298 are passed into the detector simulation. The near detectors ND280 and INGRID are  
 1299 simulated using a GEANT4 package [109, 165] to simulate the detector geometry and  
 1300 particle tracking. The response of the detectors is simulated using the elecSim pack-  
 1301 age. The far detector simulation is based upon the original Kamiokande experiment  
 1302 software which uses the GEANT3-based SKDETSIM [109, 166] package. This controls  
 1303 the interactions of particles in the water as well as Cherenkov light production. The  
 1304 water quality and PMT calibration measurements detailed in subsection 2.1.2 are also  
 1305 used within this simulation to make accurate predictions of the detector response.

## 1306 4.2 Event Reconstruction at SK

1307 Any above Cherenkov threshold event which occurs in SK will be recorded by the  
1308 PMT array, where each PMT records the time and accumulated charge is measured.  
1309 This is shown in the event displays illustrated in Figure 4.3. To be useful for physics  
1310 analyses, this series of PMT hit information needs to be reconstructed to determine the  
1311 particle’s identity and kinematics. This is because the charge and timing distribution  
1312 of photons generated by a particular particle in an event is dependent upon its initial  
1313 vertex position, time, direction, and momentum of the particle.

1314 For the purposes of this analysis, the `fitQun` reconstruction algorithm is utilised.  
1315 Its core function is to compare a prediction of the accumulated charge and timing  
1316 distribution from each PMT, generated for a particular particle hypothesis, to that  
1317 observed in the neutrino event. It determines the best particle hypothesis by min-  
1318 imising a likelihood function which includes information from PMTs which were hit  
1319 and those that were not hit. This improves upon the `APFit` reconstruction algorithm  
1320 which has been used for many previous SK analyses. `APFit` only includes information  
1321 from PMTs within the 43 deg Cherenkov cone and then sequentially fits the kinematic  
1322 parameters and particle configuration. Conversely, `fitQun` performs a simultaneous  
1323 fit, improving both the accuracy of the fit parameters and the rejection of neutral  
1324 current  $\pi^0$  events [167, 168]. The `fitQun` algorithm is based on the key concepts  
1325 on the MiniBooNE reconstruction algorithm [169] and is described in [170] which is  
1326 summarised below.

1327 An event in SK can consist of multiple “sub-events”. For example, a muon neutrino  
1328 interaction will generate a muon which will subsequently decay into an electron.  
1329 Both the muon and electron can generate Cherenkov photons but both subevents  
1330 need to be reconstructed separately. Therefore, to avoid assigning photons generated

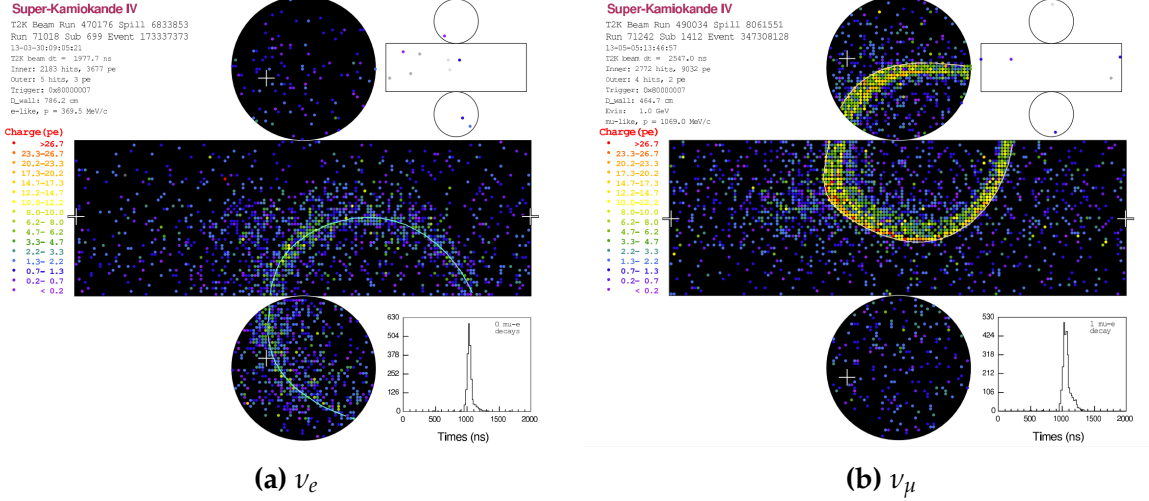


**Figure 4.3:** Event displays from Super Kamiokande illustrating the “crisp” ring from a muon and the typically “fuzzy” electron ring. Each pixel represents a PMT and the color scheme denotes the accumulated charge deposited on that PMT. Figures taken from [171].

1331 by the decay-electron to the muon, each event is divided into time clusters, termed  
 1332 “subevents”, where subevent is defined to contain at most one hit for each PMT. To  
 1333 find the subevents, a vertex goodness metric is calculated for some vertex position  $\vec{x}$   
 1334 and time  $t$ ,

$$G(\vec{x}, t) = \sum_i^{\text{hit PMTs}} \exp \left( -\frac{1}{2} \left( \frac{T_{Res}^i(\vec{x}, t)}{\sigma} \right)^2 \right) \quad (4.1)$$

1335 where

$$T_{Res}^i(\vec{x}, t) = t_i - t - |R_{PMT}^i - \vec{x}| / c_n \quad (4.2)$$

1336 is the residual hit time,  $R_{PMT}^i$  is the position of the  $i^{th}$  PMT,  $c_n$  is the speed of light in  
 1337 water and  $\sigma = 4\text{ns}$  which is comparable to the time resolution of the PMT. When the fit

1338 values of time and vertex are close to the true values,  $T_{Res}^i(\vec{x}, t)$  tends to zero resulting  
 1339 in subevents appearing as spikes in the goodness metric. The fit vertex and time are  
 1340 grid-scanned, and the values which maximise the goodness metric are selected as the  
 1341 “pre-fit vertex”. Whilst this predicts a vertex for use in the clustering algorithm, the  
 1342 final vertex is fit using the higher-precision maximum likelihood method described  
 1343 below.

1344 Once the pre-fit vertex has been determined, the goodness metric is scanned as a  
 1345 function of  $t$  to determine the number of delayed peaks. A peak-finding algorithm  
 1346 is then used on the goodness metric, requiring the goodness metric to exceed some  
 1347 threshold and drop below a reduced threshold before any delayed additional peaks  
 1348 are considered. The thresholds are set such that the rate of false peak finding is  
 1349 minimised while still attaining good data to Monte Carlo agreement. To improve  
 1350 performance, the pre-fit vertex for each delayed subevent is re-calculated after PMT  
 1351 hits from the primary subevent are masked. This improves the decay-electron tagging  
 1352 performance. Once all subevents have been determined, the time window around  
 1353 each subevent is then defined by the earliest and latest time which satisfies  $-180 <$   
 1354  $T_{Res}^i < 800\text{ns}$ . The subevents and associated time windows are then used as seeds for  
 1355 further reconstruction.

1356 For a given subevent, `fiTQun` constructs a likelihood based on the accumulated  
 1357 charge  $q_i$  and time information  $t_i$  from the  $i^{th}$  PMT,

$$L(\Gamma, \vec{\theta}) = \prod_j^{\text{unhit}} P_j(\text{unhit}|\Gamma, \vec{\theta}) \prod_i^{\text{hit}} \{1 - P_i(\text{unhit}|\Gamma, \vec{\theta})\} f_q(q_i|\Gamma, \vec{\theta}) f_t(t_i|\Gamma, \vec{\theta}), \quad (4.3)$$

1358 where  $\vec{\theta}$  defines the track parameters; vertex position, direction vector and mo-  
 1359 ments, and  $\Gamma$  represents the particle hypothesis.  $P_i(\text{unhit}|\Gamma, \vec{\theta})$  defines the probability

of the  $i^{th}$  tube to not register a hit given the track parameters and particle hypothesis. The charge likelihood,  $f_q(q_i|\Gamma, \vec{\theta})$ , and time likelihood,  $f_t(t_i|\Gamma, \vec{\theta})$ , represent the probability density function of observing charge  $q_i$  and time  $t_i$  on the  $i^{th}$  PMT given track parameters  $\vec{\theta}$  and particle hypothesis  $\Gamma$ .

As the generation and propagation of the optical photons are independent of the PMT and electronics response, it is natural to split the calculation into two. Firstly, calculating the expected number of photoelectrons (or predicted charge),  $\mu_i$ , at the  $i^{th}$  PMT, and then calculating the likelihood based on this value. This substitution allows the charge likelihood density  $f_q(q_i|\mu_i)$  and unhit probability  $P_i(\text{unhit}|\mu_i)$  to be expressed via quantities that are only dependent on the response of the PMT.

The predicted charge is calculated based on contributions from both the direct light and the scattered light. The direct light contribution is determined based on the integration of the Cherenkov photon profile along the track. PMT angular acceptance and water quality and calibration measurements discussed in subsection 2.1.2 are included to accurately model the detector's response. The scattered light is calculated in a similar way although it includes a scattering function that depends on the vertex of the particle and the position of the PMT. The charge likelihood is calculated by comparing the prediction to the observed charge in the PMT, where the prediction assumes photoelectron generation obeys a Poisson distribution.

The time likelihood is approximated to depend on the vertex  $\vec{x}$ , direction  $\vec{d}$ , and time  $t$  of the track parameters as well as the particle hypothesis. The expected time for PMT hits is calculated by assuming unscattered photons being emitted from the midpoint of the track,  $S_{mid}$ ,

$$t_i^{exp} = t + S_{mid}/c + |R_{PMT}^i - \vec{x} - S_{mid}\vec{d}|/c_n, \quad (4.4)$$

where  $c$  is the speed of light in a vacuum. The time likelihood is then expressed in terms of the residual difference between the PMT hit time and the expected hit time,  $t_i^{Res} = t_i - t_i^{exp}$ . As the first photon hit defines the PMT hit time, the time likelihood density profile is narrower for higher momenta particles which introduces a dependence on the predicted charge. The particle hypothesis and momentum also affect the Cherenkov photon distribution which modifies the shape of the time likelihood density since in reality not all photons are emitted at the midpoint of the track. As with the charge likelihood, the contributions from both the direct and scattered light to the time likelihood density are calculated separately, which are both calculated from particle gun studies.

The track parameters,  $\vec{\theta}$ , which maximise  $L(\Gamma|\vec{\theta})$  are defined the best fit parameters. In practice MINUIT [172] is used to minimise the value of  $-\ln L(\Gamma, \vec{\theta})$ . The particle hypothesis is determined by the comparison of  $L(\Gamma, \vec{\theta})$  across all viable hypotheses,  $\Gamma$ . The fit considers an electron-like, muon-like, and charged pion-like hypothesis. The particle's identity is determined by taking the ratio of the likelihood of each of the hypotheses. For instance, electrons and muons are distinguished by considering the value of  $\ln(L_e/L_\mu)$  as illustrated in Figure 4.4.

Alongside the three hypotheses which have a single final state particle generating optical photons, denoted “single-ring” particle hypotheses, the `fitQun` algorithm also considers a  $\pi^0$  hypothesis. To do this, it performs a fit looking for two standard electron-hypothesis tracks which point to the same vertex position and time. This assumes the electron tracks are generated from photon-conversion so the electron tracks actually appear offset from the proposed  $\pi^0$  vertex. For these fits, the conversion length, direction, and momenta of each photon are also considered as track parameters which are then fit in the same methodology as the standard single-ring hypotheses.

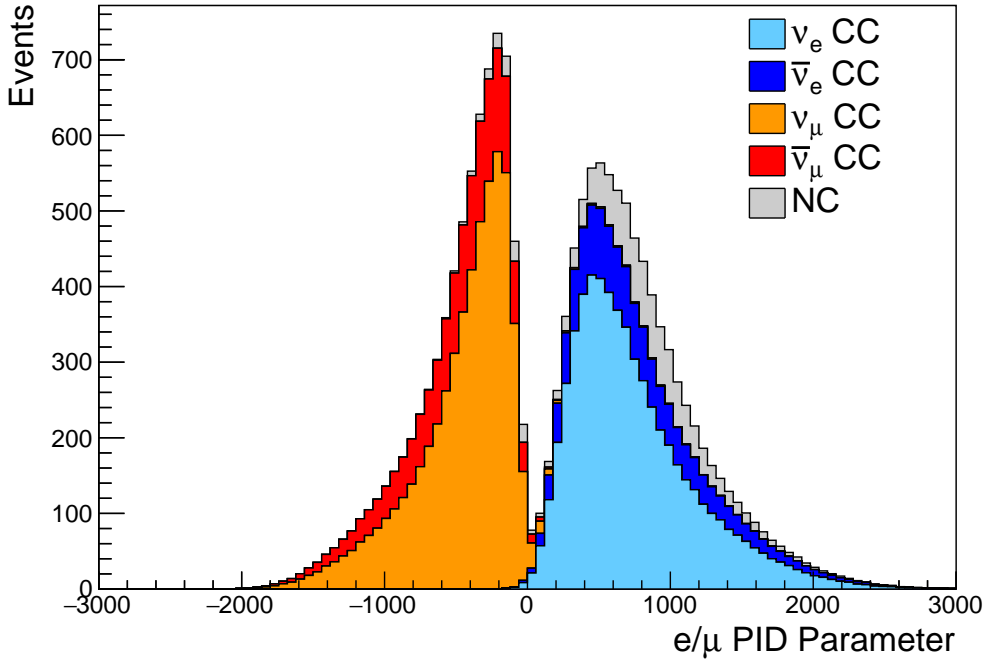


**Figure 4.4:** The electron/muon PID separation parameter for all sub-GeV single-ring events in SK-IV. The charged current (CC) component is broken down in four flavours of neutrino ( $\nu_\mu, \bar{\nu}_\mu, \nu_e$  and  $\bar{n}u_e$ ). Events with positive values of the parameter are determined to be electron-like.

The previous discussion pertains to a single final state particle that generates optical photons. However, the higher energy atmospheric neutrino events can generate final states with multiple particles which generate Cherenkov photons. These “multi-ring” hypotheses are also considered in the `fitQun` algorithm, but only for the first subevent in each ring to reduce computational cost. When calculating the charge likelihood density, the predicted charge associated with each ring is calculated separately and then merged to calculate the total accumulated charge on each PMT. Similarly, the time likelihood for the multi-ring hypothesis is calculated assuming each ring is independent. However, each track is then time-ordered based on the time of flight from the center of the track to the PMT, and the direct light from any ring incident on the PMT arrives before any scattered light. To reduce computational resources required for a fit, the multi-ring fits only consider electron-like and charged pion-like rings as the pion fit can be used as a proxy for a muon fit due to their similar mass.

1421     Typically, multi-ring fits have the largest likelihood because of the additional  
1422     degrees of freedom introduced. Multi-ring fits proceed by proposing another ring  
1423     to the previous fit and then fitting the parameters in the method described above.  
1424     The additional ring is only added if the ratio of likelihoods between the  $n$  and  $n + 1$   
1425     passes the criteria. The criteria values for single-ring and multi-ring separation have  
1426     been determined to be 9.35(11.83) based on Monte-Carlo studies, for hypotheses with  
1427     electron-like(muon-like) the first ring.

1428     As an example of how the reconstruction depends on the detector conditions, the  
1429     author of this thesis assessed the quality of event reconstruction for SK-V data. The  
1430     detector systematics invoked within the T2K-only oscillation analysis are determined  
1431     using data to Monte Carlo comparisons using the SK-IV data [173]. Due to tank-open  
1432     maintenance occurring between SK-IV and SK-V, the dark rate of each PMT was  
1433     observed to increase due to light exposure for a significant time during the repairs.  
1434     This can be seen in Figure 4.5. Run-10 of the T2K experiment was conducted in the SK-  
1435     V period, so the consistency of SK-IV and SK-V data needs to be studied to determine  
1436     whether the SK-IV defined systematics can be applied to the run-10 data. This study  
1437     was performed using the stopping muon data set for both the SK-IV and SK-V periods.  
1438     This data is used due to the high rate of interactions,  $O(200)$  events per hour, as well  
1439     as having similar energies to muons from CCQE  $\nu_\mu$  interactions. The rate of cosmic  
1440     muons does depend on the solar activity cycle [174]. This has been neglected in this  
1441     comparison study as it is the shape of the distributions which is important for the  
1442     purposes of being compared to the detector systematics. 2398.42 and 626.719 hours of  
1443     SK-IV and SK-V are used which equates to 686743 and 192504 events respectively.

1444     The predicted charge used in the `fitQun` charge likelihood calculation for each  
1445     PMT includes the photoelectron emission contribution from the dark rate of the PMT.  
1446     Therefore, the increase in the dark rate needs to be accounted for. In practice, the

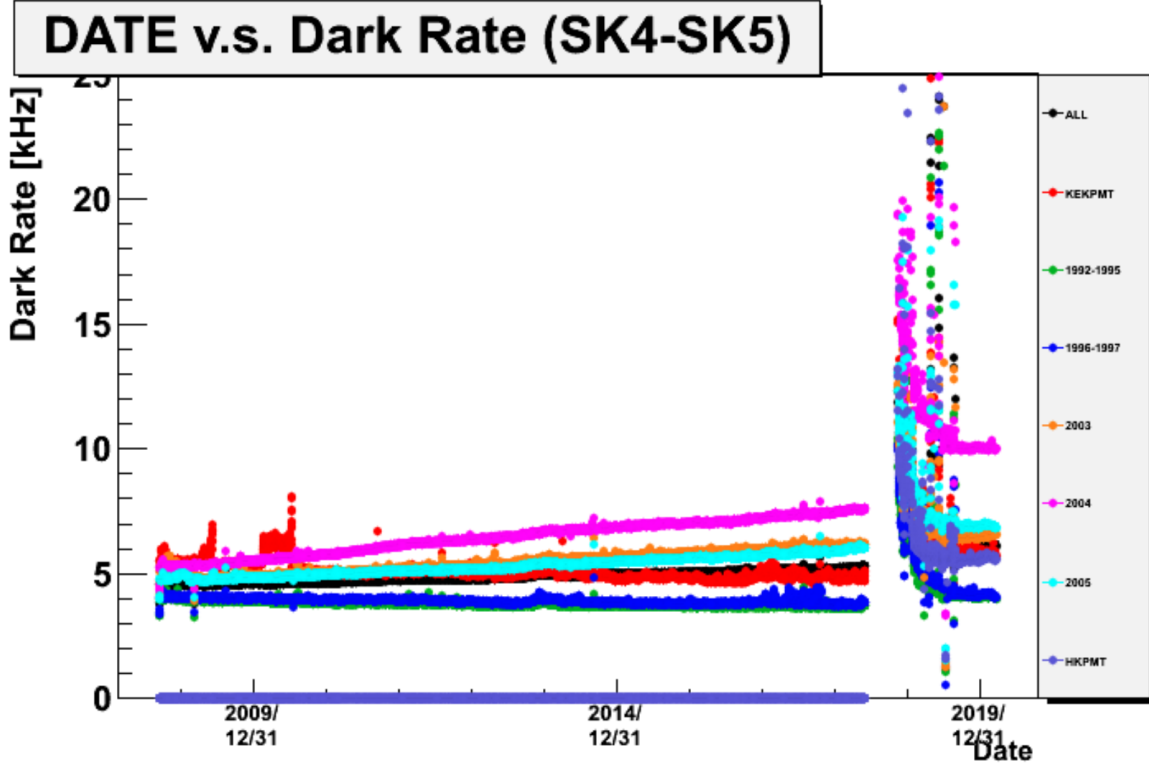


**Figure 4.5:** The variation of the measured dark rate as a function of date, broken down by PMT type. The SK-IV and SK-V periods span September 2008 to May 2018 and January 2019 to July 2020 respectively. The break in measurement between 2018 corresponds to the period of tank repair and refurbishment. Figure adapted from [173].

reconstruction algorithm takes the average dark rate for all PMTs for each SK period as an input and predicts the associated charge from this contribution. The dark rate was calculated by averaging the dark rate per run for each period separately, using the calibration measurements detailed in subsection 2.1.2. The average dark rate from SK-IV and SK-V were found to be  $4.57\text{kHz}$  and  $6.30\text{kHz}$ , respectively. The associated charge with the muon and decay electron subevents are illustrated in Figure 4.6. As expected, the increase in dark rate is not observed in the muon subevent which is of typically higher energy. However, it has a clear effect on the decay electron subevent which is lower energy.

The energy scale systematic for the SK-IV period was determined to be 2.1% [175]. It is defined to be equal to the difference between data and Monte Carlo prediction

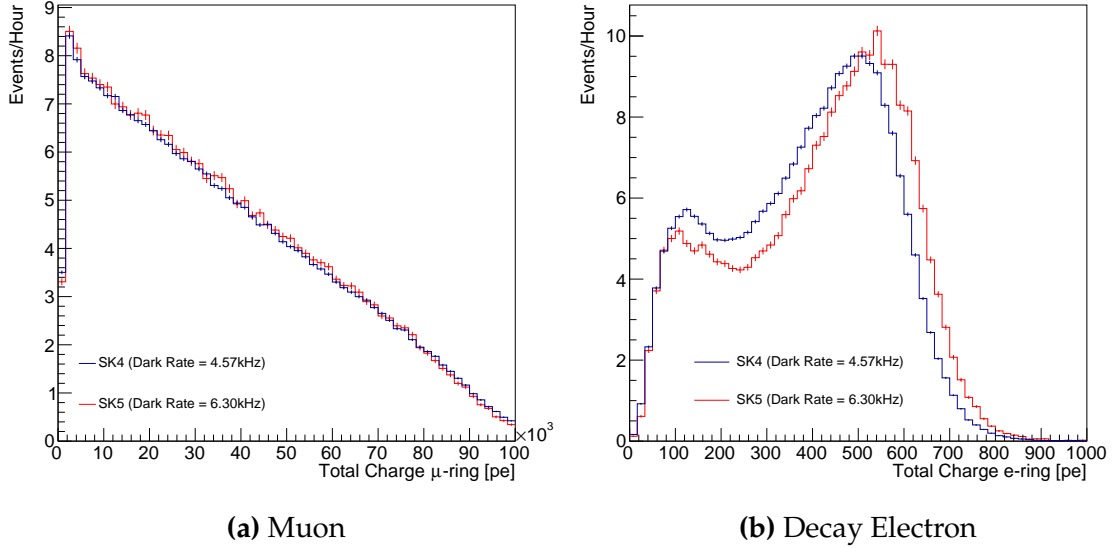


**Figure 4.6:** Comparison of the measured raw charge deposited per event from the stopping muon data samples between SK-IV (Blue) and SK-V (Red), split by the primary muon subevent and the associated decay electron subevent.

in the stopping muon data sample. To determine the consistency of the SK-IV and SK-V with respect to the energy scale systematic, the muon momentum distribution is compared between the two SK periods. The distribution of Cherenkov photons is dependent upon the momentum of the particle. This is then integrated along the track length of the particle to determine the PMT hit probability for each PMT. Consequently, the reconstructed momentum divided by track length is compared between SK-IV and SK-V as illustrated in Figure 4.7.

The consistency between these distributions has been computed in two ways. Firstly, a Gaussian is fit to each distribution separately. The mean of which is found to be  $(2.272 \pm 0.003)\text{MeV/cm}$  and  $(2.267 \pm 0.006)\text{MeV/cm}$  for SK-IV and SK-V respectively. The ratio of these is equal to  $1.002 \pm 0.003$ . The mean of the Gaussian's is consistent with the expected stopping power of a minimum ionising muon for a target material (water) with  $Z/A \sim 0.5$  [176]. The second consistency check is performed by introducing a nuisance parameter,  $\alpha$ , which modifies the SK-V distribution. The value of  $\alpha$  which minimises the  $\chi^2$  between the SK-IV and SK-V is determined by

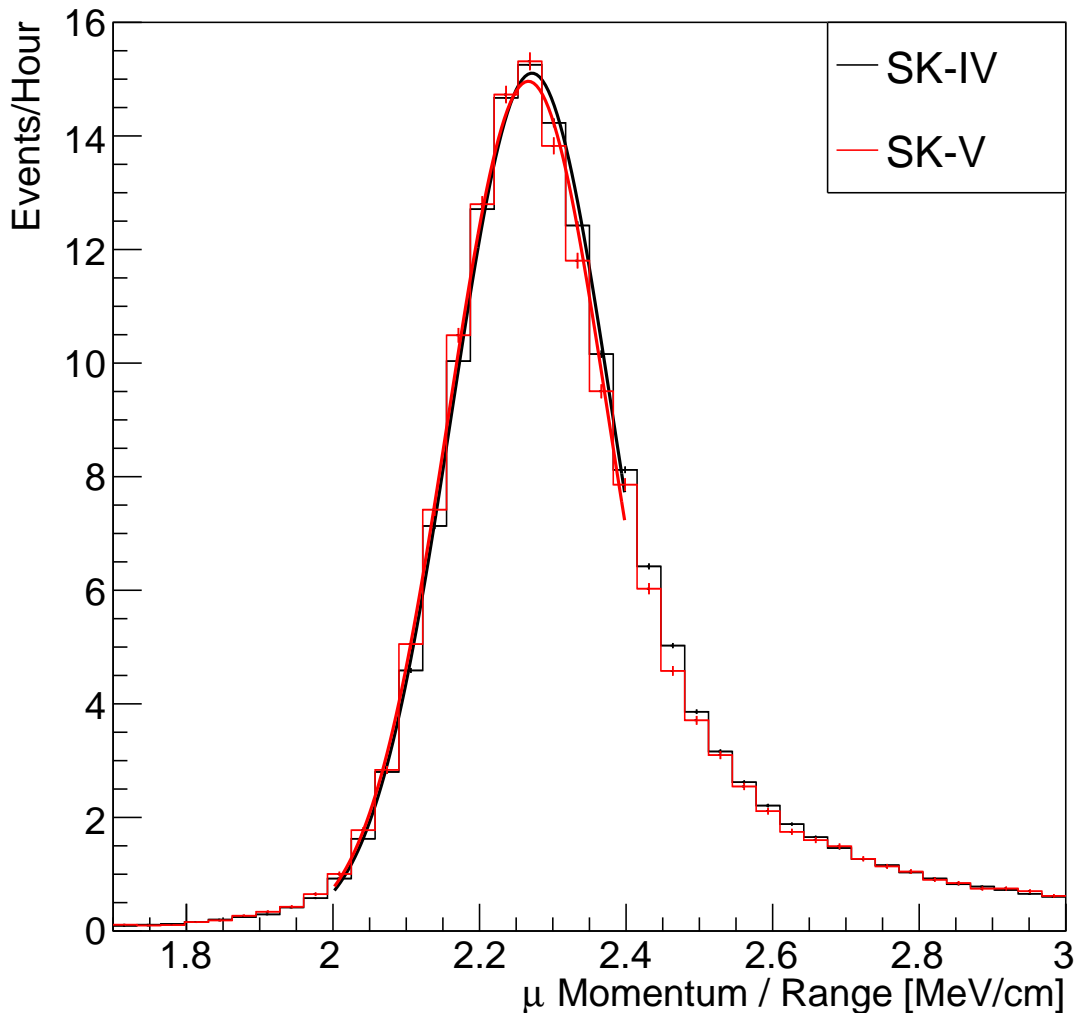


**Figure 4.7:** The distribution of the reconstructed momentum from the muon ring divided by the distance between the reconstructed muon and decay electron vertices as found in the stopping muon data sets of SK-IV (Black) and SK-IV (Red). Only events with one tagged decay electron and considered. A Gaussian fit is considered in the range [2.0, 2.4] MeV/cm and illustrated as the solid curve.

<sup>1473</sup> scanning across a range of values. This is repeated by applying  $\alpha$  as a multiplicative  
<sup>1474</sup> factor and an additive shift. The  $\chi^2$  distributions for different values of  $\alpha$  is illustrated  
<sup>1475</sup> in Figure 4.8. The values which minimise the  $\chi^2$  are found to be 0.0052 and 1.0024 for  
<sup>1476</sup> the additive and multiplicative implementations respectively. No evidence of shifts  
<sup>1477</sup> larger than the 2.1% uncertainty on the energy scale systematic has been found in the  
<sup>1478</sup> reconstructed momentum distribution of SK-IV and SK-V.

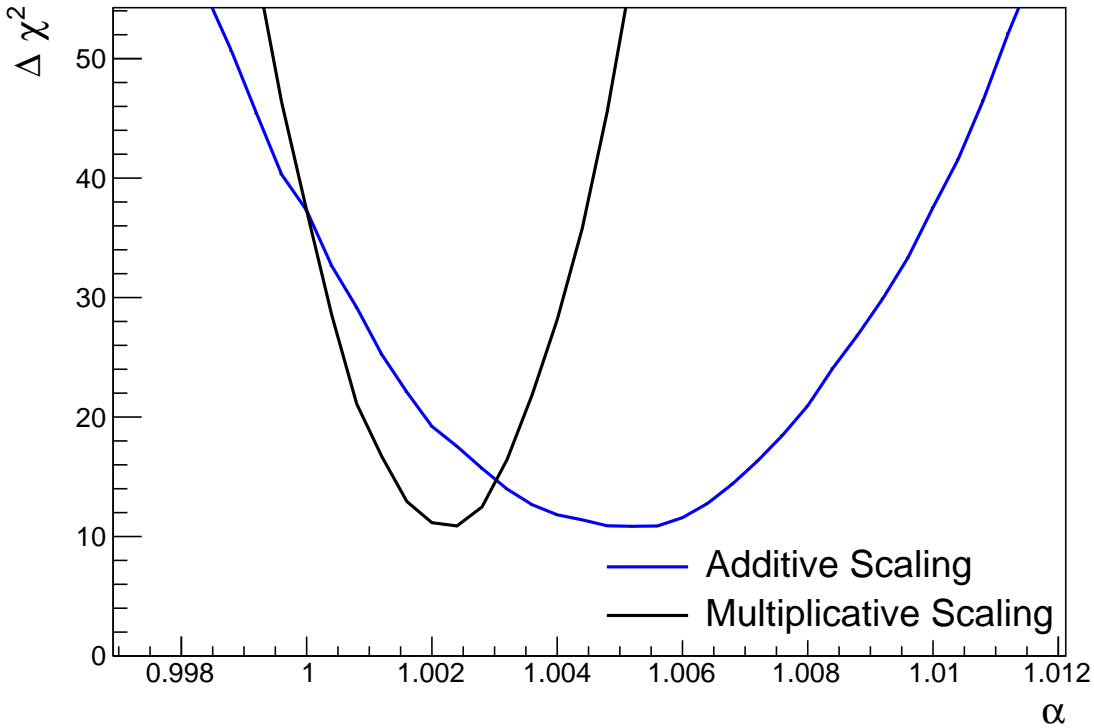


**Figure 4.8:** The  $\chi^2$  difference between the SK-IV and SK-V reconstructed muon momentum divided by range when the SK-V is modified by the scaling parameter  $\alpha$ . Both additive (Blue) and multiplicative (Black) scaling factors have been considered. In practice, the additive scaling factor actually uses the value of  $(\alpha - 1.0)$ .

### <sup>1479</sup> 4.3 Event Selection at SK

<sup>1480</sup> Atmospheric neutrino events observed in the SK detector are categorised into three  
<sup>1481</sup> different types of samples; fully contained (FC), partially contained (PC) and up-  
<sup>1482</sup> going muon (Up- $\mu$ ), using signatures in the inner and outer detector (ID and OD,  
<sup>1483</sup> respectively). To identify FC neutrino events, it is required that the neutrino interacts  
<sup>1484</sup> inside the fiducial volume of the ID such that no significant OD activity is observed.  
<sup>1485</sup> For this analysis, an event is defined to be in the fiducial volume providing the  
<sup>1486</sup> event vertex is at least 0.5m away from the ID walls. PC events have the same ID  
<sup>1487</sup> requirements but can have a larger signal present inside the OD. Typically these events  
<sup>1488</sup> are higher energy muon interactions that penetrate the ID walls. The Up- $\mu$  sample

1489 contains events where muons are created in the OD water or rock below the tank  
1490 and then propagate upwards through the detector. The reason downward-going  
1491 muons generated from neutrino interactions above the tank are neglected is due to  
1492 the difficulty in separating their signature from the cosmic muon shower background.  
1493 The sample categories are visually depicted in Figure 4.9.

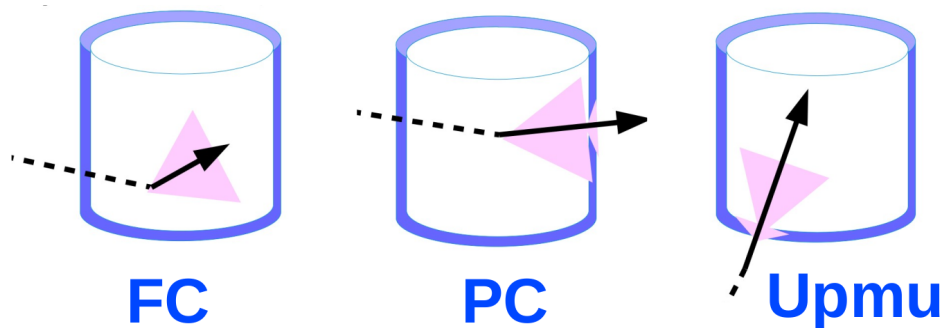


**Figure 4.9:** A depiction of the topology patterns for fully-contained (FC), partially-contained (PC) and up-going muon ( $\text{Up-}\mu$ ) samples included in this analysis.

1494 Based on the event characteristics as defined by the `fitQun` event reconstruction  
1495 software, the FC events are further divided up by

- 1496 • **Visible Energy:** equal to the sum of the reconstructed kinetic energy above the  
1497 Cerenkov threshold for all rings present in the event. The purpose is to separate  
1498 events into sub-GeV and multi-GeV categories.
- 1499 • **Number of observed Cerenkov rings.** The purpose is to separate single-ring and  
1500 multi-ring events, where single-ring events predominantly consist of quasi-elastic  
1501 interactions and multi-ring events are resonant pion production or deep inelastic  
1502 scattering events.
- 1503 • **Particle identification parameter of the most energetic ring:** A value deter-  
1504 mined from the maximum likelihood value based on `fitQun`'s electron, muon, or  
1505 pion hypothesis. The purpose is to separate electron-like and muon-like events.

- 1506     • **Number of sub-events:** Based on optimised time cuts, this quantity determines  
1507       the number of observed decay electrons associated with an event. The main  
1508       purpose is to separate quasi-elastic events (which have one decay electron emitted  
1509       from the muon decay) and resonant pion production events (which have two  
1510       decay electrons emitted from the muon and pion).

1511       The PC and Up- $\mu$  categories are broken down into “through-going” and “stopping”  
1512       samples depending on whether the muon left the detector. This is because the stopping  
1513       events deposited the entire energy of the interaction into the detector, resulting in better  
1514       reconstruction. Through-going Up- $\mu$  samples are further broken down by whether  
1515       any hadronic showering was observed in the event which would be mostly likely due  
1516       to DIS interactions. The expected neutrino energy for the different categories is given  
1517       in Figure 4.10. FC sub-GeV and multi-GeV events peak around 0.7GeV and 3GeV  
1518       respectively, with slightly different peak energies for  $\nu_x \rightarrow \nu_e$  and  $\nu_x \rightarrow \nu_\mu$ . PC and  
1519       Up- $\mu$  are almost entirely comprised of  $\nu_x \rightarrow \nu_\mu$  events and peak around 7GeV and  
1520       100GeV respectively.

1521       In data-taking operation, the SK detector observes many background events along-  
1522       side the beam and atmospheric neutrino signal events of physics interest. Cosmic  
1523       ray muons and flasher events, which is the spontaneous discharge of a given PMTm  
1524       contribute the largest amount of background events in the energy range relevant to  
1525       oscillation analyses. Lower energy analyses like DSNB searches are also subject to  
1526       radioactive backgrounds [177]. Therefore the data recorded is reduced with the aim of  
1527       removing these background events. The reduction process is detailed in [46, 83] and  
1528       briefly summarised below.

1529       The first two steps in the FC reconstruction remove most cosmic ray muons by  
1530       requiring a significant amount of ID activity compared to that measured in the OD.  
1531       This is done by counting the total number of photoelectrons recorded in the ID as

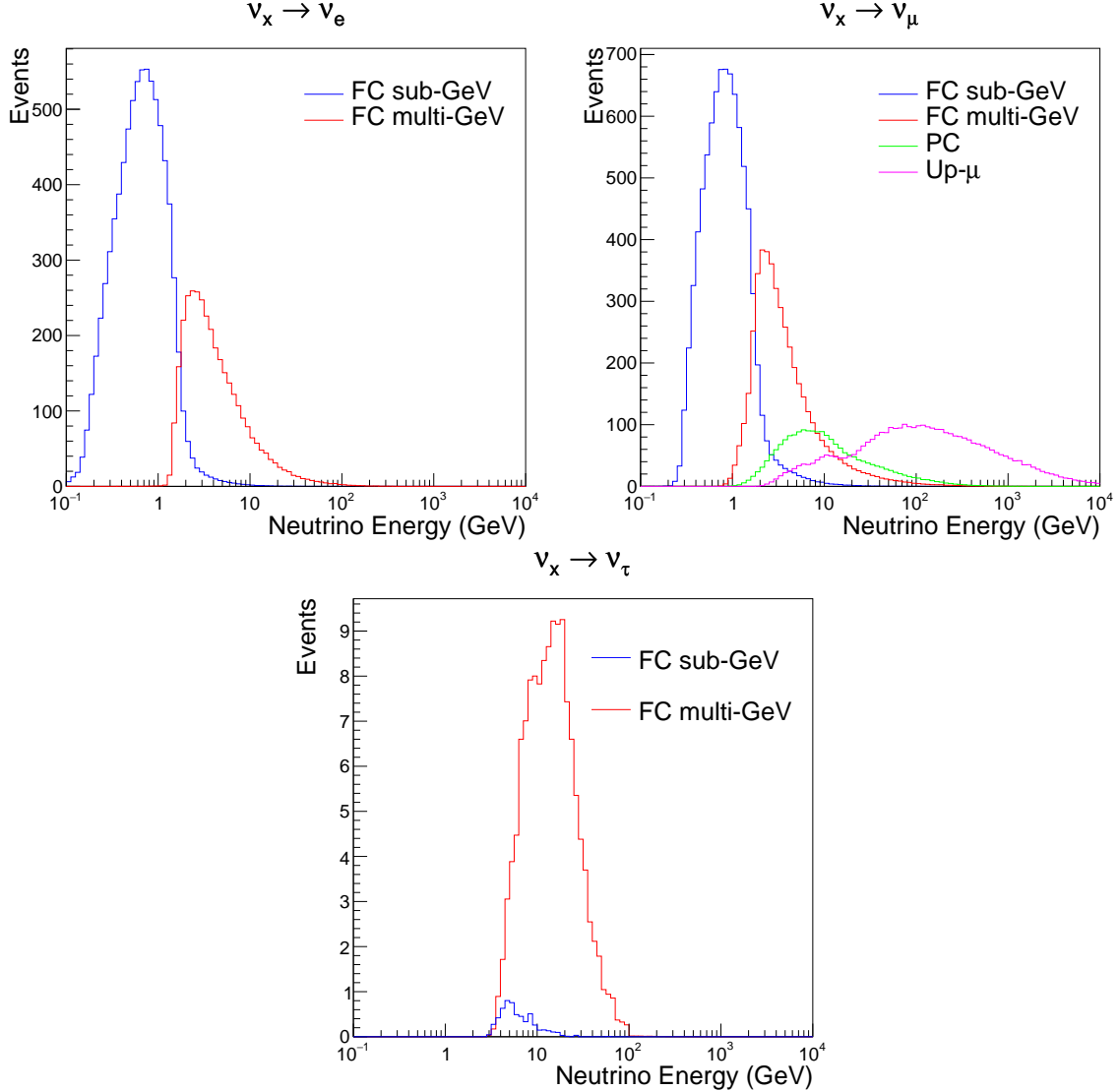


**Figure 4.10:** The predicted neutrino flux of the fully contained (FC) sub-GeV and multi-GeV, partially contained (PC) and upward-going muon (Up- $\mu$ ) events. The prediction is broken down by the  $\nu_x \rightarrow \nu_e$  prediction (top left),  $\nu_x \rightarrow \nu_\mu$  prediction (top right) and  $\nu_x \rightarrow \nu_\tau$  prediction (bottom). All systematic dials are set to their nominal values and the Asimov A oscillation parameters are assumed.

well as the number of hits in the OD. A third reduction step is then applied to select cosmic-ray muons that pass the initial reduction. These are typically high momentum muons or events which leave only a small number of hits in the OD. A purpose-built cosmic muon fitter is used to determine the entrance (or exit) position of the muon from the OD and a cut is applied to OD activity contained within 8m of this position. Flasher events are removed in the fourth reduction step which is based on the close

1538 proximity of PMT hits surrounding the PMT producing the flash. Events that pass the  
1539 reduction stage to this point are reconstructed using the more accurate APFit algorithm  
1540 and the fifth step of the reduction uses the information from this more accurate fitter  
1541 to repeat the third and fourth reduction steps using tighter cuts. This particularly  
1542 targets invisible muons which are below the Cherenkov threshold resulting in no  
1543 OD activity but whose decay electrons generate light inside the ID. The final cuts  
1544 require the event vertex to be within the fiducial volume (0.5m from the wall although  
1545 the nominal distance is 2.0m), visible energy  $E_{vis} > 30\text{MeV}$  and fewer than 16 hits  
1546 within the higher energy OD cluster. The culmination of the fully contained reduction  
1547 results in 8.09 events/day in the nominal fiducial volume [178]. The uncertainty in the  
1548 reconstruction is calculated by comparing Monte Carlo prediction to data. The largest  
1549 discrepancy is found to be 1.3% in the fourth reduction step.

1550 The PC and Up- $\mu$  events are also processed through their own reduction processes  
1551 detailed in [46]. Both of these samples are reconstructed with the APFit algorithm  
1552 rather than `fiTQun`. This is because the efficiency of reconstructing events that leave  
1553 the detector has not been sufficiently studied for reliable systematic uncertainties. 0.66  
1554 and 1.44 events/day are found after the final step of reduction for the PC and Up- $\mu$   
1555 samples respectively.

1556 **Chapter 5**

1557 **Oscillation Probability Calculation**

1558 The calculation of the oscillation probability is crucial to the reliability of the sensitivity  
1559 measurements of the analysis presented within this thesis. Firstly, it is important to  
1560 understand how and where the sensitivity to the oscillation parameters comes from  
1561 for both atmospheric and beam samples. An overview of how these sets of samples  
1562 observe changes in  $\delta_{CP}$ ,  $\Delta m_{23}^2$ , and  $\sin^2(\theta_{23})$  as well as how the atmospheric samples  
1563 have an increased sensitivity to mass hierarchy determination is given in section 5.1.  
1564 It also explains the additional complexities involved when including atmospheric  
1565 neutrinos as compared to a beam-only analysis.

1566 Without additional techniques, atmospheric sub-GeV upward-going neutrinos can  
1567 artificially inflate the sensitivity to  $\delta_{CP}$  due to the quickly varying oscillation probabil-  
1568 ity in this region. Therefore, a “sub-sampling” approach has been developed to reduce  
1569 these biases ensuring accurate and reliable sensitivity measurements. This technique  
1570 ensures that small-scale unresolvable features of the oscillation probability have been  
1571 averaged over whilst the large-scale resolvable features in the oscillation probability  
1572 have been kept. The documentation of this technique is found in section 5.2 alongside  
1573 the validation of the choices which have been made. The CUDAProb3 implementation  
1574 choice made within the fitting framework, as detailed in section 5.3, ensures that the  
1575 analysis can be done in a timely manner.

1576 Whilst the beam neutrinos are assumed to propagate through a constant density  
1577 slab of material, the density variations through the Earth result in more complex  
1578 oscillation patterns Furthermore, the uncertainty in the electron density can modify

1579 the oscillation probability for the denser core layers of the Earth. section 5.4 details  
1580 the model of the Earth used within this analysis. This includes the official SK-only  
1581 methodology as well as relatively straightforward improvements that can be made to  
1582 more closely approximate the PREM model. Another quirk of atmospheric neutrinos  
1583 oscillation studies is that the height of production in the atmosphere is not known  
1584 on an event-by-event analysis. An analytical averaging technique that approximates  
1585 the uncertainty of the oscillation probability has been followed, with the author of  
1586 this thesis being responsible for the implementation and validation. This technique is  
1587 illustrated in section 5.5 alongside the variation in oscillation probability which would  
1588 be an expected effect in the down-going and horizontal-going neutrinos.

## 1589 5.1 Overview

1590 The analysis presented within this thesis focuses on the determination of oscillation  
1591 parameters from atmospheric and beam neutrinos. Whilst subject to the same oscil-  
1592 lation probability, the way in which the two sets of samples have sensitivity to the  
1593 different oscillation parameters differs quite significantly.

1594 Atmospheric neutrinos have a varying baseline, or “path length”, such that the  
1595 distance each neutrino travels before interacting is dependent upon the zenith angle.  
1596 Therefore the oscillation probability can be represented as a two-dimensional “oscillo-  
1597 gram” as shown in Figure 5.1. For this calculation, four layers of fixed density were  
1598 used to model the Earth with values taken from an approximation of the PREM model.  
1599 These can be seen in the distinct discontinuities in the oscillogram as a function of the  
1600 zenith angle.

1601 Another complexity of atmospheric neutrino oscillation probability calculation is  
1602 the uncertainty in the height at which a neutrino was produced, termed the “produc-

tion height". Primary cosmic rays, which contribute most of the neutrino flux, can interact anywhere between the Earth's surface and  $\sim 50$ km above that. The baseline,  $L$ , for a neutrino generated with zenith angle,  $\theta$ , and production height,  $h$ , can be calculated as

$$L = \sqrt{(R_E + h)^2 - R_E^2 (1 - \cos^2(\theta))} - R_E \cos(\theta), \quad (5.1)$$

where  $R_E = 6,371$ km is the Earth's radius.

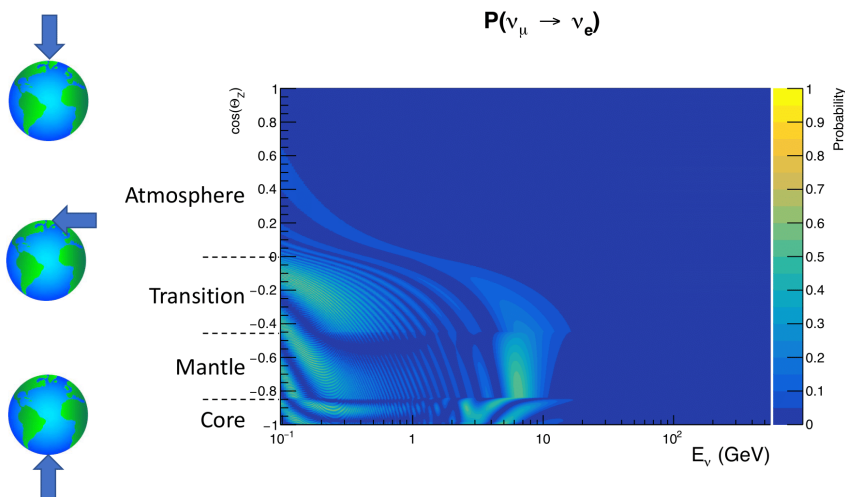


**Figure 5.1:** An "Oscillogram" that depicts the  $P(\nu_\mu \rightarrow \nu_e)$  oscillation probability as a function of neutrino energy and cosine of the zenith angle. The zenith angle is defined such that  $\cos(\theta_Z) = 1.0$  represents neutrinos that travel from directly above the detector. The four-layer constant density PREM model approximation is used and Asimov A oscillation parameters are assumed.

Atmospheric neutrinos do have some sensitivity to  $\delta_{CP}$  through a normalisation term. Figure 5.2 illustrates the difference in oscillation probability between CP-conserving and CP-violating  $\delta_{CP}$  values. The result is a complicated oscillation pattern in the appearance probability for sub-GeV upgoing neutrinos. The detector does not have sufficient resolution to resolve these individual patterns so the sensi-

1613 tivity to  $\delta_{CP}$  for atmospheric neutrinos comes via the overall normalisation of the  
1614 sub-GeV upgoing events. The presence of matter means that the effect  $\delta_{CP}$  has on  
1615 the oscillation probability is not equal between neutrinos and antineutrinos which  
1616 would be expected when propagating through a vacuum. This is further extenuated  
1617 by the fact that SK can not distinguish neutrinos and antineutrinos well and that the  
1618 cross-section neutrino interaction is larger than that for antineutrinos. Finally, sample  
1619 selections (discussed in [DB: Link to selection chapter](#)) targeting different neutrino  
1620 interaction modes (charge current quasi-elastic and single pion production) result in  
1621 an imbalance in the percentage of neutrinos to anti-neutrinos in these samples due  
1622 to pion capture. Negatively charged pions from antineutrino interactions are more  
1623 likely to be captured by a nucleus compared to a positively charged pion emitted from  
1624 a neutrino interaction. This all culminates in atmospheric neutrinos having a very  
1625 complex sensitivity to  $\delta_{CP}$ .

1626 Atmospheric neutrinos are subject to matter effects as they travel through the dense  
1627 matter in the Earth. The vacuum and matter oscillation probabilities for  $P(\nu_e \rightarrow \nu_e)$   
1628 and  $P(\bar{\nu}_e \rightarrow \bar{\nu}_e)$  are presented in Figure 5.3. The oscillation probability for both neutrinos  
1629 and antineutrinos are affected in the presence of matter but the resonance (Effects  
1630 around  $E_\nu \sim 5\text{GeV}$ ) only occurs for neutrinos in normal mass hierarchy and antineu-  
1631 trinos for inverse mass ordering. The exact position and amplitude of the resonance  
1632 depend on  $\sin^2(\theta_{23})$  meaning that the atmospheric neutrinos have sensitivity to the  
1633 octant of  $\theta_{23}$ .

1634 As the T2K beam flux is centered at the first oscillation maximum, the sensitivity  
1635 to  $\delta_{CP}$  is predominantly observed as a change in the event-rate of e-like samples in  
1636  $\nu/\bar{\nu}$  modes. Figure 5.4 illustrates the  $P(\nu_\mu \rightarrow \nu_e)$  oscillation probability for a range  
1637 of  $\delta_{CP}$  values. A circular modulation of the oscillation peak (in both magnitude and  
1638 position) is observed when varying throughout the allowable values of  $\delta_{CP}$ . The CP-

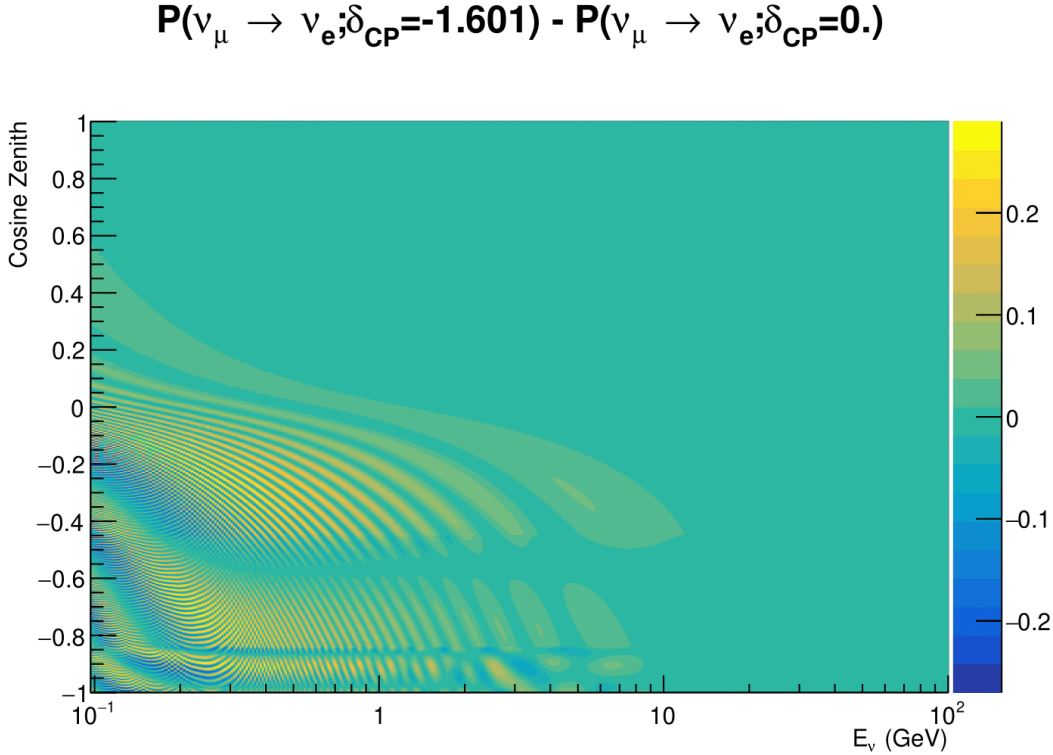


**Figure 5.2:** The effect of  $\delta_{CP}$  for atmospheric neutrinos given in terms of the neutrino energy and zenith angle. The oscillogram compares the  $P(\nu_\mu \rightarrow \nu_e)$  oscillation probability for a CP conserving ( $\delta_{CP} = 0.0$ ) and CP violating ( $\delta_{CP} = -1.601$ ) value of  $\delta_{CP}$ . The other oscillation parameters assume the “Asimov A” oscillation parameter set given in Table 5.1.

1639 conserving values of  $\delta_{CP} = 0, \pi$  have a lower(higher) oscillation maximum than the  
 1640 CP-violating values of  $\delta_{CP} = -\pi/2 (\delta_{CP} = \pi/2)$  leading to a  $\sin(\delta_{CP})$  type sensitivity.  
 1641 A sub-dominant shift in the energy of the oscillation peak is also present to aid in  
 1642 separating the two CP-conserving values of  $\delta_{CP}$ .

1643 T2K’s sensitivity to the atmospheric oscillation parameters is more of a shape-  
 1644 based variation of the muon-like samples, as illustrated in Figure 5.4. The value of  
 1645  $\Delta m_{32}^2$  laterally shifts the position of the oscillation dip (around  $E_\nu \sim 0.6$ GeV) in the  
 1646  $P(\nu_\mu \rightarrow \nu_\mu)$  oscillation probability. A variation of  $\sin^2(\theta_{23})$  is predominantly observed  
 1647 as a vertical shift of the oscillation dip with second-order horizontal shifts being due  
 1648 to matter effects. The beam neutrinos have limited sensitivity to matter effects due

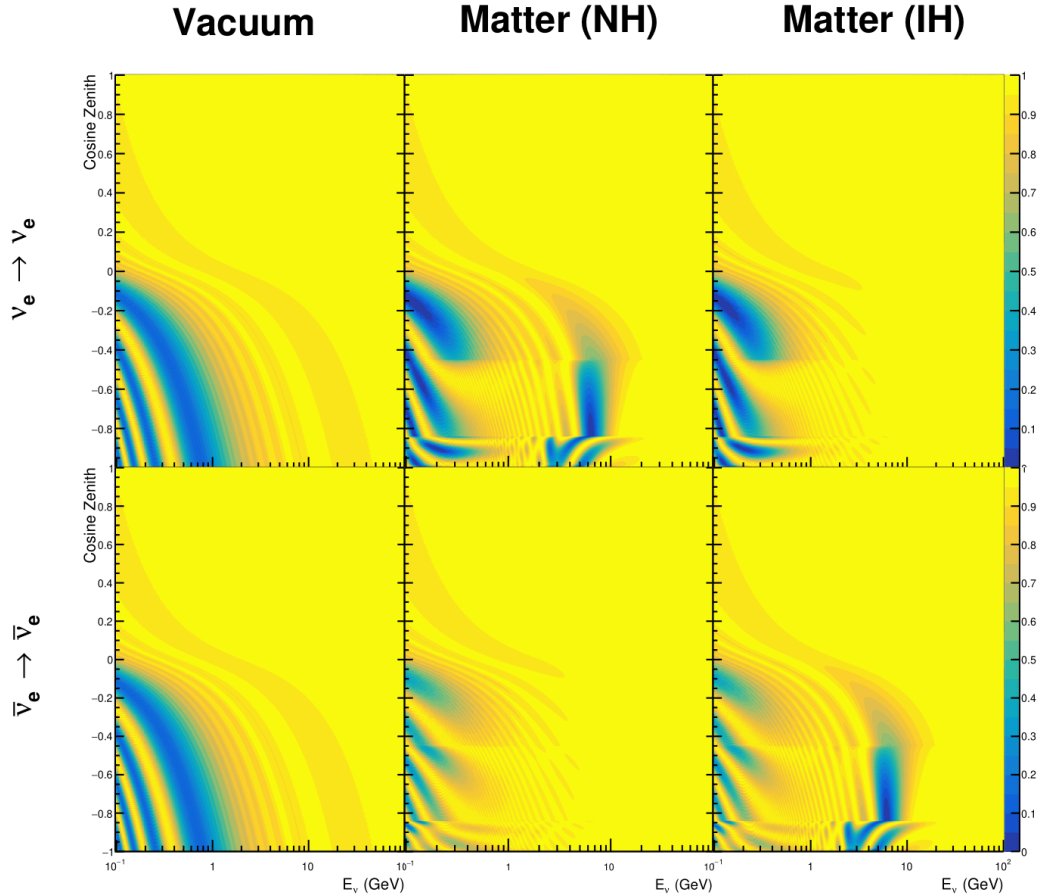


**Figure 5.3:** An illustration of the matter-induced effects on the oscillation probability, given as a function of neutrino energy and zenith angle. The top row of panels gives the  $P(\nu_e \rightarrow \nu_e)$  oscillation probability and the bottom row illustrates the  $P(\bar{\nu}_e \rightarrow \bar{\nu}_e)$  oscillation probability. The left column highlights the oscillation probability in a vacuum, whereas the middle and right column represents the oscillation probabilities when the four layer fixed density PREM model is assumed. All oscillation probabilities assume the “Asimov A” set given in Table 5.1, but importantly, the right column sets an inverted mass hierarchy. The “matter resonance” effects at  $E_\nu \sim 5\text{GeV}$  can be seen in the  $P(\nu_e \rightarrow \nu_e)$  for normal mass hierarchy and  $P(\bar{\nu}_e \rightarrow \bar{\nu}_e)$  for inverted hierarchy.

to the shorter baseline as well as the Earth’s mantle is relatively low-density material  
 (as compared to the Earth’s core). For some values of  $\delta_{CP}$ , the degeneracy in the number of e-like events allows the mass hierarchy to be resolved. This leads to a  $\delta_{CP}$ -dependent mass hierarchy sensitivity which can be seen in Figure 5.5.

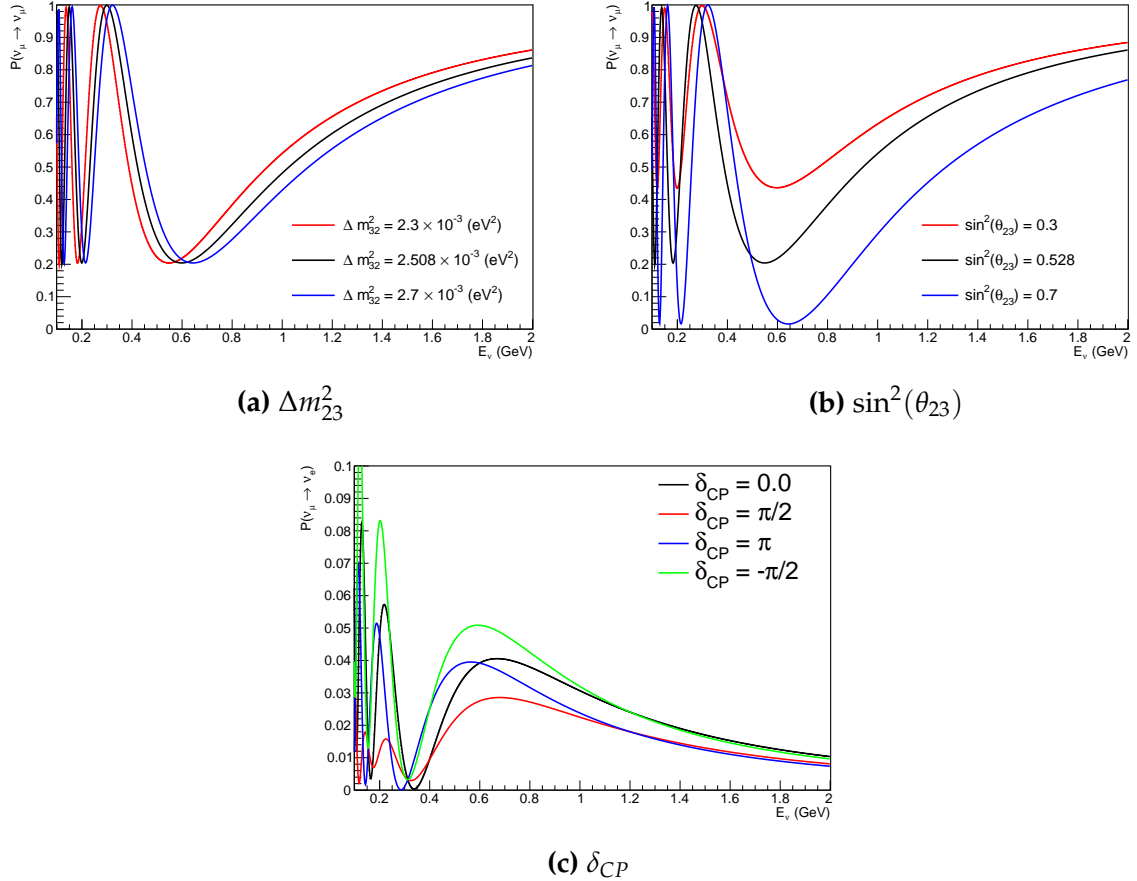


**Figure 5.4:** The oscillation probability for beam neutrino events given as a function of neutrino energy. All oscillation parameters assume the “Asimov A” set given in Table 5.1 unless otherwise stated. Each panel represents a change in one of the oscillation parameters whilst keeping the remaining parameters fixed.

Whilst all oscillation channels should be included for completeness, the computational resources required to run a fit are limited and any reasonable approximations which reduce the number of oscillation probability calculations that need to be made should be applied. The  $\nu_e \rightarrow \nu_{e,\mu,\tau}$  (and antineutrino equivalent) oscillations can be ignored for beam neutrinos as the  $\nu_e/\bar{\nu}_e$  fluxes being approximately two orders of magnitude smaller than the corresponding  $\nu_\mu/\bar{\nu}_\mu$  flux. Furthermore, as the peak neutrino energy of the beam is well below the threshold for  $\tau$  production ( $E_\nu \sim 3$  GeV [179]) only a small proportion of the neutrinos produced in the beam have the required energy. For the few neutrinos that have sufficient energy, the oscillation probability is very small due to the short baseline. Whilst these approximations can be made for the

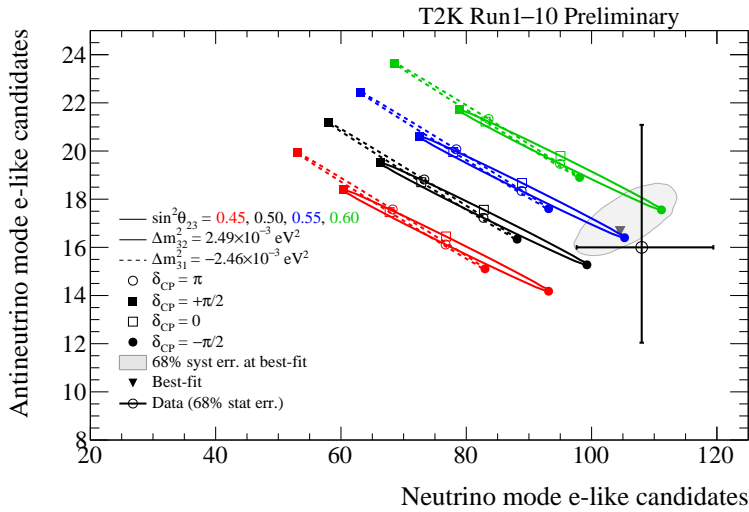


**Figure 5.5:** The number of electron-like events in the FHC and RHC operating mode of the beam, as a function of the oscillation probabilities. Both normal hierarchy (Solid) and inverse hierarchy (Dashed) values of  $\Delta m_{23}^2$  are given.

<sub>1663</sub> beam neutrinos, the atmospheric flux of  $\nu_e$  is of the same order of magnitude as the  $\nu_\mu$   
<sub>1664</sub> flux and the energy distribution of atmospheric neutrinos extends well above the tau  
<sub>1665</sub> production threshold.

<sub>1666</sub> Throughout this thesis, several spectra predictions, Asimov fits, and contour com-  
<sub>1667</sub> parisons are presented which require oscillation parameters to be assumed. Table 5.1  
<sub>1668</sub> defines two sets of oscillation parameters, with “Asimov A” set being close to the pre-  
<sub>1669</sub> ferred values from a previous T2K-only fit [180] and “Asimov B” being CP-conserving  
<sub>1670</sub> and further from maximal  $\theta_{23}$  mixing.

Parameter	Asimov A	Asimov B
$\Delta m_{12}^2$	$7.53 \times 10^{-5} \text{ eV}^2$	
$\Delta m_{32}^2$	$2.509 \times 10^{-3} \text{ eV}^2$	
$\sin^2(\theta_{12})$	0.304	
$\sin^2(\theta_{13})$	0.0219	
$\sin^2(\theta_{23})$	0.528	0.45
$\delta_{CP}$	-1.601	0.0

**Table 5.1:** Reference values of the neutrino oscillation parameters for two different oscillation parameter sets.

**<sub>1671</sub> 5.2 Treatment of Fast Oscillations**

<sub>1672</sub> As shown in Figure 5.6, atmospheric neutrino oscillations have a significantly more  
<sub>1673</sub> complex structure for upgoing neutrinos with energy below 1GeV. This is because the  
<sub>1674</sub>  $L/E$  dependence of the oscillation probability in this region induces rapid variations  
<sub>1675</sub> for small changes in  $L$  or  $E$ . As discussed in section 5.1, this is also the region in which  
<sub>1676</sub> atmospheric neutrinos have sensitivity to  $\delta_{CP}$ . In practice, the direction between  
<sub>1677</sub> the detector and a neutrino's production vertex is inferred from the direction of any  
<sub>1678</sub> secondary particles created in the detector target. For low-energy neutrinos, this  
<sub>1679</sub> inference can be rather poor and introduces a distinct difference to beam neutrinos  
<sub>1680</sub> where the direction to production vertex is very well known.

<sub>1681</sub> As a consequence of the poor detector resolution, an average oscillation probability  
<sub>1682</sub> is observed in this region. This creates a computational problem as a significantly  
<sub>1683</sub> large amount of MC statistics would be required to accurately predict the number  
<sub>1684</sub> of events in each bin if MC averaging was the only technique used. This section  
<sub>1685</sub> describes the 'sub-sampling' approach developed for this analysis and compares it to  
<sub>1686</sub> the methodology used within the SK-only analysis.

<sub>1687</sub> The official SK-only analysis uses the osc3++ oscillation parameter fitter [181]. To  
<sub>1688</sub> perform the fast oscillation averaging, it uses a 'nearest-neighbour' technique. For a  
<sub>1689</sub> given neutrino MC event, the nearest neighbours in reconstructed lepton momentum  
<sub>1690</sub> and zenith angle are found and a distribution of neutrino energies is built. This  
<sub>1691</sub> distribution is then used to compute an average oscillation probability for the given  
<sub>1692</sub> neutrino MC event.

<sub>1693</sub> For the  $i^{th}$  event, the oscillation weight is calculated as

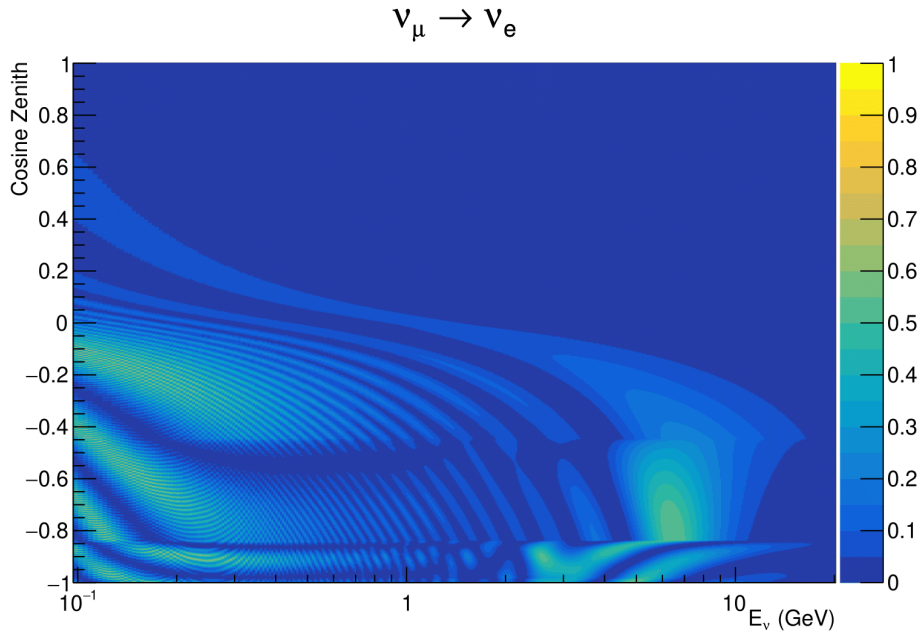


**Figure 5.6:** The oscillation probability  $P(\nu_\mu \rightarrow \nu_e)$ , given as a function of neutrino energy and zenith angle, which highlights an example of the “fast” oscillations in the sub-GeV upgoing region.

$$W_i = \frac{1}{5}P(E_i, \bar{L}_i) + \frac{1}{5} \sum_{\beta=-1, -0.5, 0.5, 1} P(E_i + \beta\sigma_i, L_\beta), \quad (5.2)$$

where  $P(E, L)$  is the oscillation probability calculation for neutrino energy  $E$  and path length  $L$ ,  $\sigma_i$  is the RMS of the energy distribution for the given event, and the two path lengths,  $\bar{L}_i$  and  $L_\beta$  are discussed below. In practice, twenty of the nearest neighbours are used to generate the neutrino energy distribution. All of the oscillation probability calculations are performed with a fixed zenith angle (and therefore have same matter density profile).

The uncertainty in the production height is controlled by using an “average” production height.  $\bar{L}_i$  represents the average path length computed using twenty production heights taken from the Honda flux model’s prediction [44] for a fixed zenith angle, where the production heights are sampled in steps of 5% of their cumulative

1704 distribution function.  $L_\beta$  values are similarly calculated but instead use different  
1705 combinations of four production heights (sampled in the same way),

$$\begin{aligned} L_{-1.0} &= \frac{1}{4}L(45, 50, 55, 60), \\ L_{-0.5} &= \frac{1}{4}L(35, 40, 65, 70), \\ L_{+0.5} &= \frac{1}{4}L(25, 30, 75, 68), \\ L_{+1.0} &= \frac{1}{4}L(15, 20, 85, 89). \end{aligned} \tag{5.3}$$

1706 This averaging works well because of the correlation between the true neutrino  
1707 zenith angle and the inferred direction from secondary particles in the detector. For  
1708 low-energy neutrinos, where the resolution of the true neutrino direction is poor,  $\sigma_i$   
1709 will be large, resulting in significant averaging effects. Contrary to this, the inferred  
1710 direction of high-energy neutrinos will be much closer to the true value, meaning that  
1711  $\sigma_i$  will be smaller.

1712 In practice, this technique is performed before the fit in order to deal with the  
1713 computational cost. Oscillation probabilities are pre-calculated on a 4D grid. This  
1714 is possible as the Osc3++ framework uses binned oscillation parameters rather than  
1715 continuous so the oscillation parameters used in the fit are known prior to run-time.  
1716 The framework used in the analysis presented within this thesis uses continuous  
1717 oscillation parameters. Due to the MCMC technique invoked within the fitter (see  
1718 chapter 3), there is no way to know which oscillation parameter values will be selected  
1719 in each step at run-time. Therefore, the oscillation parameter calculation would have  
1720 to be performed at run-time which is very expensive for event-by-event reweighting.  
1721 Having to compute five oscillation probabilities per event would require far too many

1722 computational resources to be viable so the SK technique can not be used within this  
1723 analysis. However, the concept of the averaging technique can be taken from it.

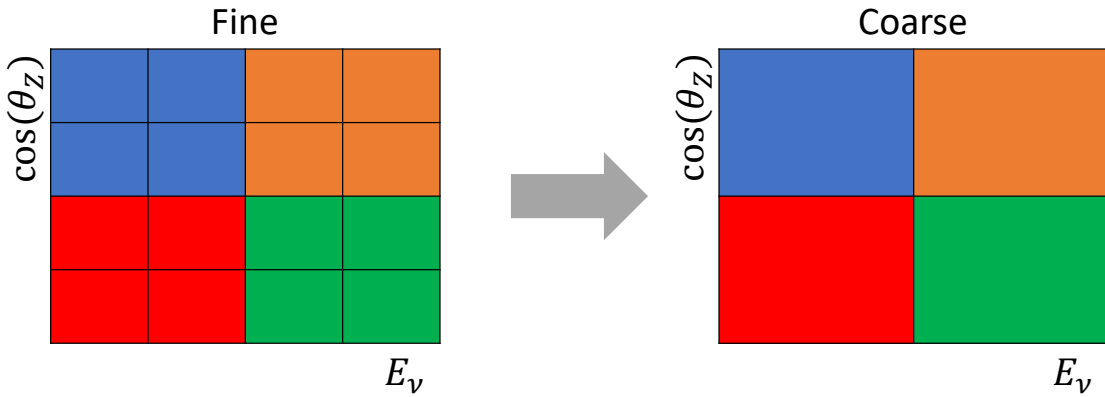


**Figure 5.7:** Illustration of the averaging procedure for  $N = 2$ . The oscillation probabilities calculated on the finer left binning are averaged to obtain the oscillation probabilities in the coarser right binning. These averaged oscillation probabilities with the coarser binning are then applied to each event during the fit.

1724 This analysis uses a binned oscillogram in which oscillation probabilities for a given  
1725 event are selected based on that event's attributes. To perform a similar averaging as  
1726 the SK analysis, a sub-sampling approach has been devised. The technique can be  
1727 explained by considering a "fine" and "coarse" oscillogram. The fine oscillograms  
1728 are used to define the array of cosine zeniths and energies for the neutrino oscillation  
1729 engine. The coarse oscillograms cover the same phase-space as the fine oscillograms  
1730 but have fewer bins in that range. Then, for a given coarse oscillogram bin, the value  
1731 of that bin will be taken as the average of all the oscillation probabilities of all the fine  
1732 oscillogram bins which fall into that coarse oscillogram bin.

1733 The binning which is used to calculate the oscillation probabilities, known as the  
1734 'fine' binning, has  $N \times N$  subdivisions per coarse bin. The value assigned to a coarse  
1735 bin is the linear average (flat prior in  $E_\nu$  and  $\cos(\theta_Z)$ ) of all the oscillation probabilities  
1736 calculated at the center of each fine bin contained within that coarse bin. Figure 5.7  
1737 illustrates the  $N = 2$  example where the assigned value to a coarse bin is the linear

1738 average of the four fine bins which fall in that coarse bin. Whilst the coarse bin edges  
1739 are not linear on either axis, the sub-division of the fine bins is linear over the range  
1740 of a coarse bin. The alignment of the fine and coarse binning edges is checked at  
1741 run-time.

1742 The coarse binning is defined with  $67 \times 52$  bins in true neutrino energy  $\times$  cosine  
1743 zenith. In general, the binning is logarithmically spaced in neutrino energy but has  
1744 some hand-picked bin edges. Firstly, the bin density around the matter resonance is  
1745 smoothly increased around the matter resonance region. This is to avoid smearing  
1746 this region which can be well sampled by the Monte Carlo. Secondly, bin edges  
1747 are selected to hit  $0.4, 0.6, 1, 10, 30, 50, 100\text{GeV}$ . This is to ensure that the Coloumb  
1748 correction systematic and the atmospheric flux systematics definitions in neutrino  
1749 energy can be hit. The cosine zenith binning is approximately linearly spaced across  
1750 the allowable range but the values of layer transitions are hit precisely;  $-0.8376$   
1751 (core-mantle) and  $-0.4464$  (mantle/transition zone). Bins are spread further apart for  
1752 downgoing events as this is a region unaffected by the fast oscillation wavelengths  
1753 and reduces the total number of calculations required to perform the reweight (Not  
1754 the number required to perform the oscillation calculation).

1755 The choice of  $N$  is justified based on two studies. Firstly, the variation of event  
1756 rates of each sample is studied as a function of the number of subdivisions. For  
1757 a given set of oscillation parameters thrown from the PDG prior constraints, the  
1758 oscillation probabilities are calculated using a given value of  $N$ . Each sample is re-  
1759 weighted and the event rate is stored. The value of  $N$  is scanned from 1, which  
1760 corresponds to no averaging, to 24, which corresponds to the largest computationally  
1761 viable subdivision binning. The event rate of each sample at large  $N$  is expected to  
1762 converge to a stationary value due to the fine binning fully sampling the small-scale

1763 structure. Figure 5.8 illustrates this behaviour for the SubGeV\_elike\_0dcy sample for  
 1764 30 different throws of the oscillation parameters.

### SubGeV-elike-0dcy

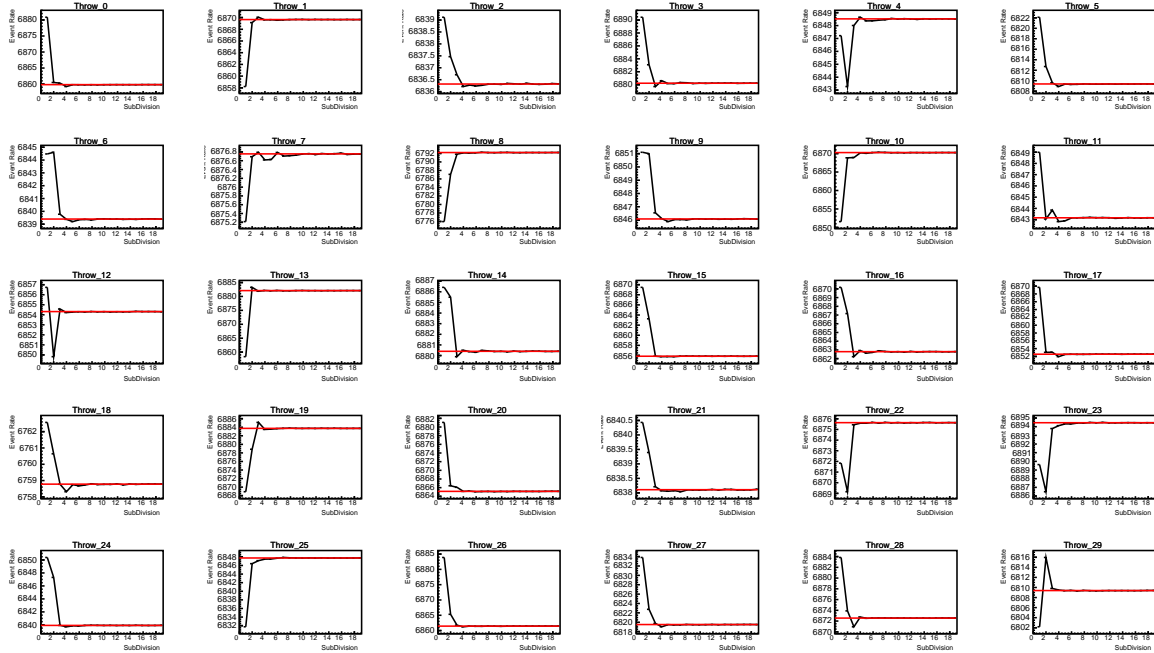


**Figure 5.8:** Event rate of the SubGeV\_elike\_0dcy sample as a function of the number of subdivisions per coarse bin. Each subplot represents the event rate of the sample at a different oscillation parameter set (thrown from the PDG priors). The red line in each subplot represents the mean of the event rate over the different values of sub-divisions for that particular oscillation parameter throw.

1765 Denoting the event rate for one sample for a given throw  $t$  at each  $N$  by  $\lambda_t^{(N)}$ , the  
 1766 average over all considered  $N$  values ( $\bar{\lambda}_t = \frac{1}{24} \sum_{N=1}^{24} \lambda_t^{(N)}$ ) is computed. The variance  
 1767 in the event rate at each  $N$  is then calculated from

$$\text{Var}[\lambda^{(N)}] = \frac{1}{N_{\text{throws}}} \sum_{t=1}^{N_{\text{throws}}} \left( \lambda_t^{(N)} - \bar{\lambda}_t \right)^2 - \left[ \frac{1}{N_{\text{throws}}} \sum_{t=1}^{N_{\text{throws}}} \left( \lambda_t^{(N)} - \bar{\lambda}_t \right) \right]^2. \quad (5.4)$$

The aim of the study is to find the lowest value of  $N$  such that this variance is below 0.001. This is the typical threshold used by T2K fitters to validate systematic implementation so is just as applicable to the oscillation probability calculation. The results of this study for each atmospheric sample used within this thesis are illustrated in Figure 5.9 for 2000 throws of the oscillation parameters. As can be seen, the variance is below the threshold at  $N = 10$ , and is driven primarily by the SubGeV\_mulike\_1dcy and SubGeV\_elike\_0dcy selections.

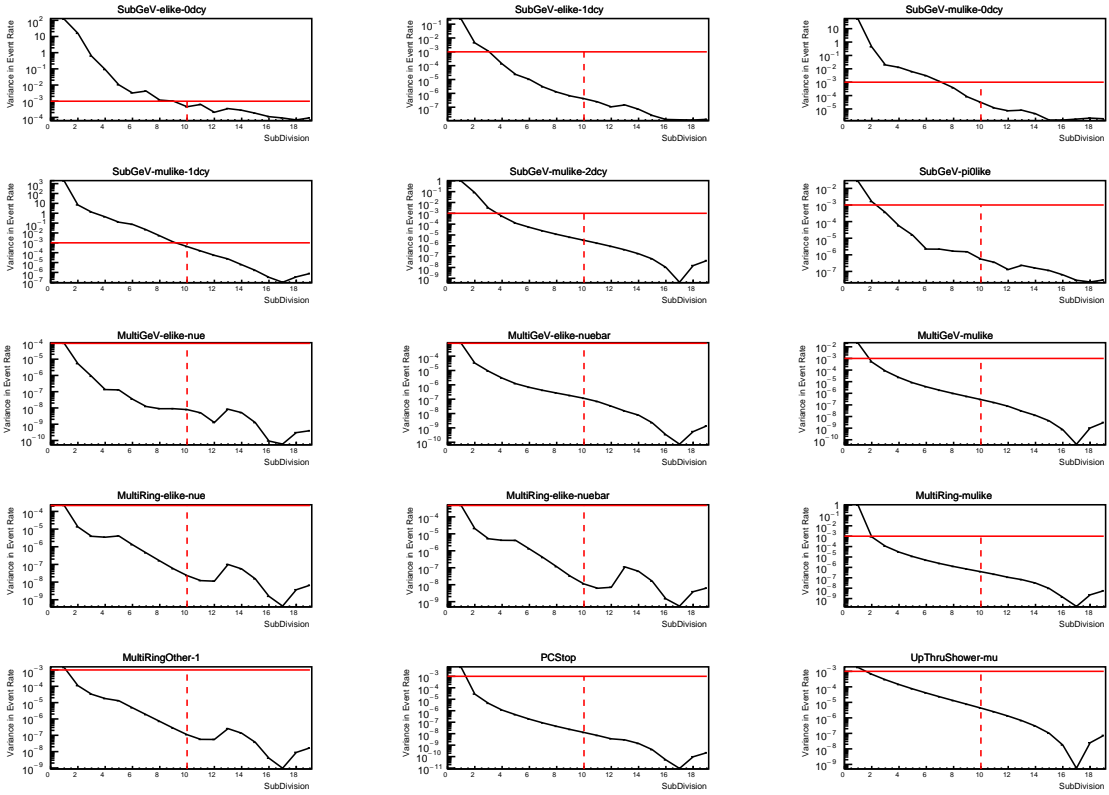


**Figure 5.9:** Variance of event rate for each atmospheric sample as a function of the number of sub-divisions per coarse bin. The solid red line indicates the 0.1% threshold and the dashed red line is a graphical indication of the variance at a sub-division  $N = 10$ .

The second study to determine the value of  $N$  is as follows. The likelihood for each sample is computed against an Asimov data set created with oscillation parameters from “Asimov A” in Table 5.1. Following Equation 5.4, the variance of the log-likelihood over all considered  $N$  is computed. The results are shown in Figure 5.10.

1779 This tests the impact of the averaging on each sample's binning by reconstructed  
 1780 momentum and/or zenith angle and also provides a scale for the calculation errors  
 1781 compared to their statistical uncertainties.

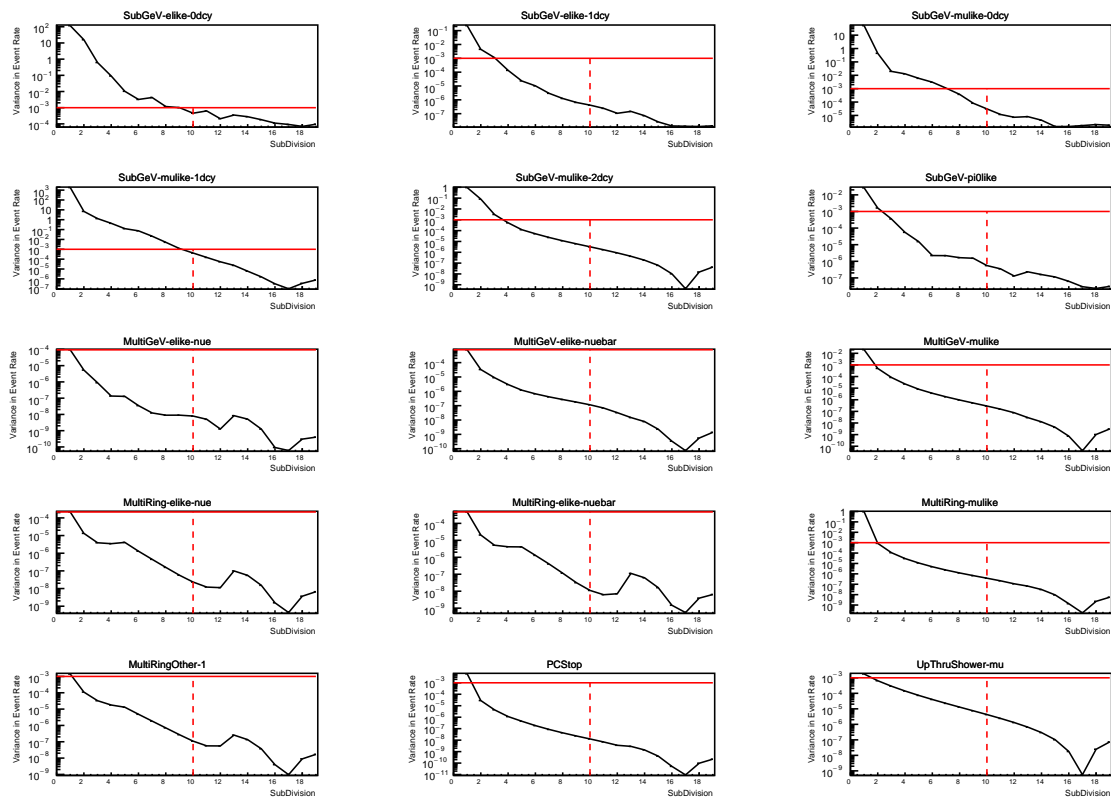


**Figure 5.10:** Variance of sample likelihood, when compared to 'Asimov data' set at Asimov A, for each atmospheric sample as a function of the number of sub-divisions per coarse bin. The solid red line indicates the 0.1% threshold and the dashed red line is a graphical indication of the variance at a sub-division  $N = 10$ .

1782 A choice of  $N$  sub-divisions per coarse bin has a variance in both event rate and  
 1783 log-likelihood residuals less than the required threshold of 0.001. The event rate test is  
 1784 the more stringent test. For the variance of log-likelihood residuals, the largest value is  
 1785 of order  $10^{-7}$ , corresponding to an error on the log-likelihood of about  $3 \times 10^{-4}$ , small  
 1786 enough to be negligible for the oscillation analysis.

1787 In practice Figure 5.11 illustrates the effect of the smearing using  $N = 10$ . The fast  
1788 oscillations in the sub-GeV upgoing region have been replaced with a normalisation  
1789 effect whilst the large matter resonance structure remains.

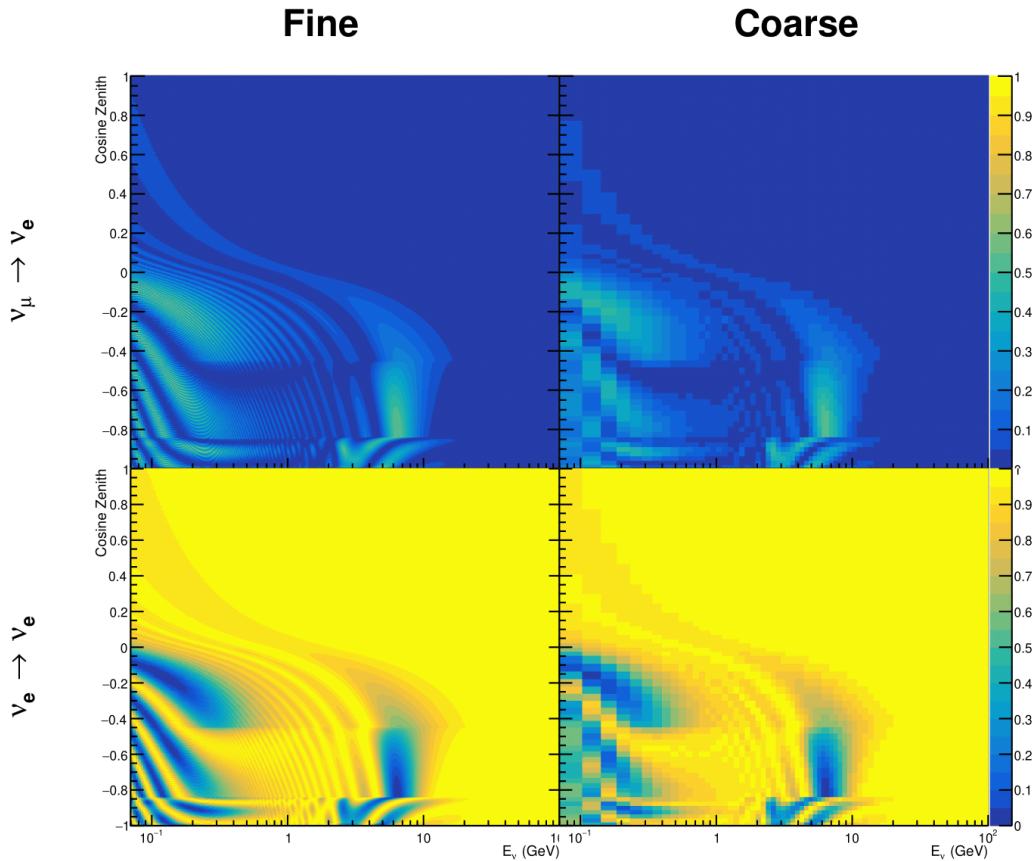


**Figure 5.11:** The oscillation probability,  $P(\nu_\mu \rightarrow \nu_e)$  (top row) and  $P(\nu_e \rightarrow \nu_e)$  (bottom row), given as a function of neutrino energy and zenith angle. The left column gives the “fine” binning used to calculate the oscillation probabilities and the right column illustrates the “coarse” binning used to reweight the MC events. The fine binning choice is given with  $N = 10$ , which was determined to be below threshold from Figure 5.9 and Figure 5.10.

<sub>1790</sub> **5.3 Calculation Engine**

<sub>1791</sub> As previously discussed in section 5.2, the calculation of oscillation probabilities is per-  
<sub>1792</sub> formed at run-time due to utilising continuous oscillation parameters. Consequently,  
<sub>1793</sub> the time per calculation is crucial for fit performance. The fitting framework used for  
<sub>1794</sub> this analysis was developed with ProbGPU [182]. This is a GPU-only implementation  
<sub>1795</sub> of the prob3 engine [183]. It is primarily designed for neutrino propagation in a beam  
<sub>1796</sub> experiment (single layer of constant density) with the atmospheric propagation code  
<sub>1797</sub> not being used prior to the analysis in this thesis.

<sub>1798</sub> Another engine, CUDAProb3 [184], has been implemented within the fitting frame-  
<sub>1799</sub> work used within this analysis. It has been specifically optimised for atmospheric  
<sub>1800</sub> neutrino oscillation calculation so unfortunately does not contain the code to replace  
<sub>1801</sub> the beam oscillation calculation. Based on the benefits shown by the implementation  
<sub>1802</sub> in this chapter, efforts are being placed into including linear propagation for beam  
<sub>1803</sub> neutrino propagation into the engine [185]. The engine utilises object-orientated tech-  
<sub>1804</sub> niques as compared to the functional implementation of ProbGPU. This allows the  
<sub>1805</sub> energy and cosine zenith arrays to be kept on GPU memory, rather than having to  
<sub>1806</sub> load these arrays onto GPU memory for each calculation. General memory interfacing  
<sub>1807</sub> is one of the slowest tasks which GPUs can do, so being able to eliminate this signifi-  
<sub>1808</sub> cantly reduces the time required for calculation. This can be seen in Figure 5.12, where  
<sub>1809</sub> the GPU implementation of CUDAProb3 is approximately three times faster than the  
<sub>1810</sub> ProbGPU engine.

<sub>1811</sub> Another significant advantage of CUDAProb3 is that it contains a CPU multithreaded  
<sub>1812</sub> implementation which is not possible with the ProbGPU or prob3 engines. This elimi-  
<sub>1813</sub> nates the requirement for GPU resources when submitting jobs to batch systems. As  
<sub>1814</sub> illustrated in Figure 5.12, the calculation speed depends on the number of available

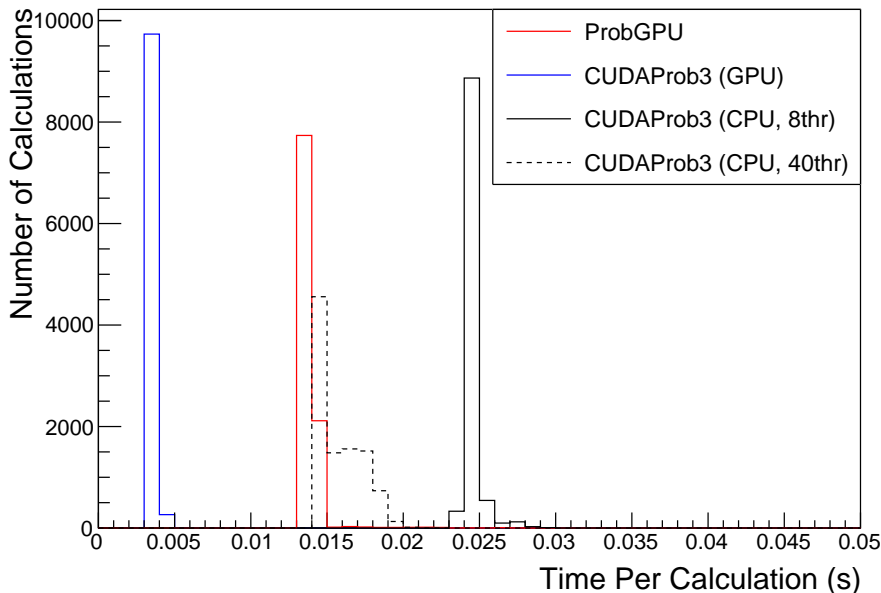


**Figure 5.12:** The calculation time taken to both calculate the oscillation probabilities and fill the “coarse” oscillograms, following the technique given in section 5.2, for the CUDAProb3 and ProbGPU (Red) calculation engines. CUDAProb3 has both a GPU (Blue) and CPU (Black) implementation, where the CPU implementation is multithreaded. Therefore, 8-threads (solid) and 40-threads (dashed) configurations have been used. Prob3, which is a CPU single-thread implementation has a mean step time of 1.142s.

1815 threads. Using 8 threads (which is typical of the batch systems being used) is ap-  
 1816 proximately twice as slow as the ProbGPU engine implementation, but would allow  
 1817 the fitting framework to be run on many more resources. This fact is utilised for any  
 1818 SK-only fits but GPU resources are required for any fits which include beam samples  
 1819 due to the ProbGPU requirement.

## 1820 5.4 Matter Density Profile

1821 For an experiment observing atmospheric neutrinos propagating through the Earth,  
 1822 such as the studies presented in this thesis, a model of the Earth’s density and layering  
 1823 is required. The model used within this analysis is the Preliminary Reference Earth  
 1824 Model (PREM) [186]. This model provides piecewise cubic polynomials as a function

of radius which results in the density profile illustrated in Figure 5.13. As will be discussed in section 5.5, the propagator used within the calculation engine requires constant density layers. To follow the official SK-only analysis [181], the average density of each layer has been taken from the PREM model. Table 5.2 documents the density and radii of the layers used within this approximation.

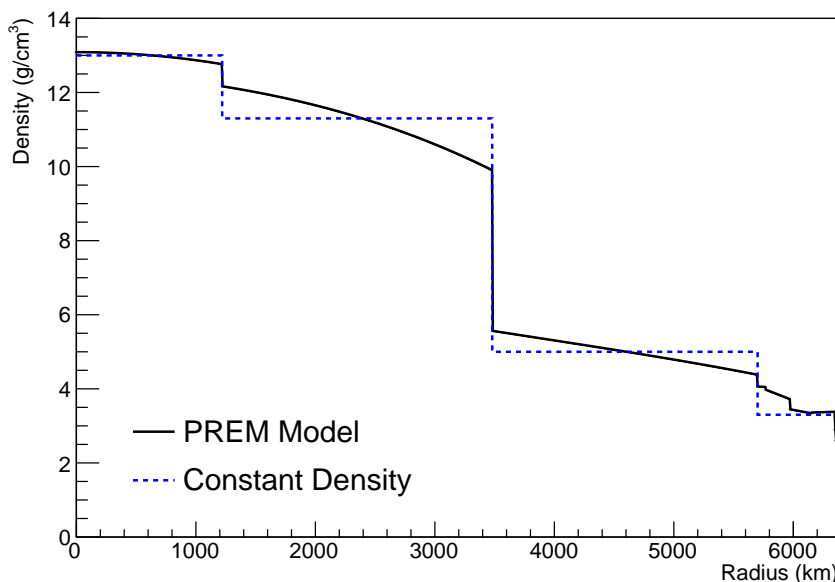


**Figure 5.13:** The density of the Earth given as a function of the radius, as given by the PREM model (Black) and the constant density four-layer approximation (Blue), as used in the official SK-only analysis.

Layer	Outer Radius [km]	Density [g/cm <sup>3</sup> ]	Chemical composition (Z/A)
Inner Core	1220	13	$0.468 \pm 0.029$
Outer Core	3480	11.3	$0.468 \pm 0.029$
Lower Mantle	5701	5.0	0.496
Transition Zone	6371	3.3	0.496

**Table 5.2:** Description of the four layers of the Earth invoked within the average constant density approximation of the PREM model [186].

The density measurements provided in the PREM model are provided in terms of mass density, whereas neutrino oscillations are sensitive to the electron number density. This value can be computed as the product of the chemical composition, or

the  $Z/A$  value, and the mass density of each layer. Currently, the only way to calculate this value for layers close to the Earth's core is through neutrino oscillations. The chemical composition of the upper layers of the Earth's Mantle and the Transition zone is well known due to it being predominantly pyrolite which has a chemical composition value of 0.496 [187]. The components of the Earth's core region are less well known. Consequently, the chemical composition dial for the core layers is set to a value of 0.468 [188]. This value is assigned a Gaussian error with a standard deviation equivalent to the difference in chemical composition in core and mantle layers. Figure 5.14 illustrates the effect of moving from the  $Z/A = 0.5$  method which is used in the official SK-only analysis [181] to more precise values recorded by other neutrino experiments.

The beam oscillation probability in this thesis uses a baseline of 295km, density  $2.6\text{g/cm}^3$  [189], and chemical composition 0.5 as is done by the official T2K-only analysis.

Whilst the propagator requires a fixed density layer model of the Earth, the density only has to be fixed for a specific neutrino energy  $\times \cos(\theta_Z)$  bin in a given layer (I.e. set of values at which to calculate the oscillation probability). As the density is a function of radius, which is a function of the direction in which a neutrino propagates, a better approximation of the PREM model can be made if a  $\cos(\theta_Z)$ -specific density is calculated.

To achieve this, the average density,  $\langle \rho \rangle_i$ , in the  $i^{th}$  layer, is calculated as the density,  $\rho$ , integrated over the track a given  $\cos(\theta_Z)$ ,

$$\langle \rho \rangle_i = \frac{1}{t_{i+1} - t_i} \int_{t_i}^{t_{i+1}} \rho(t) dt \quad (5.5)$$

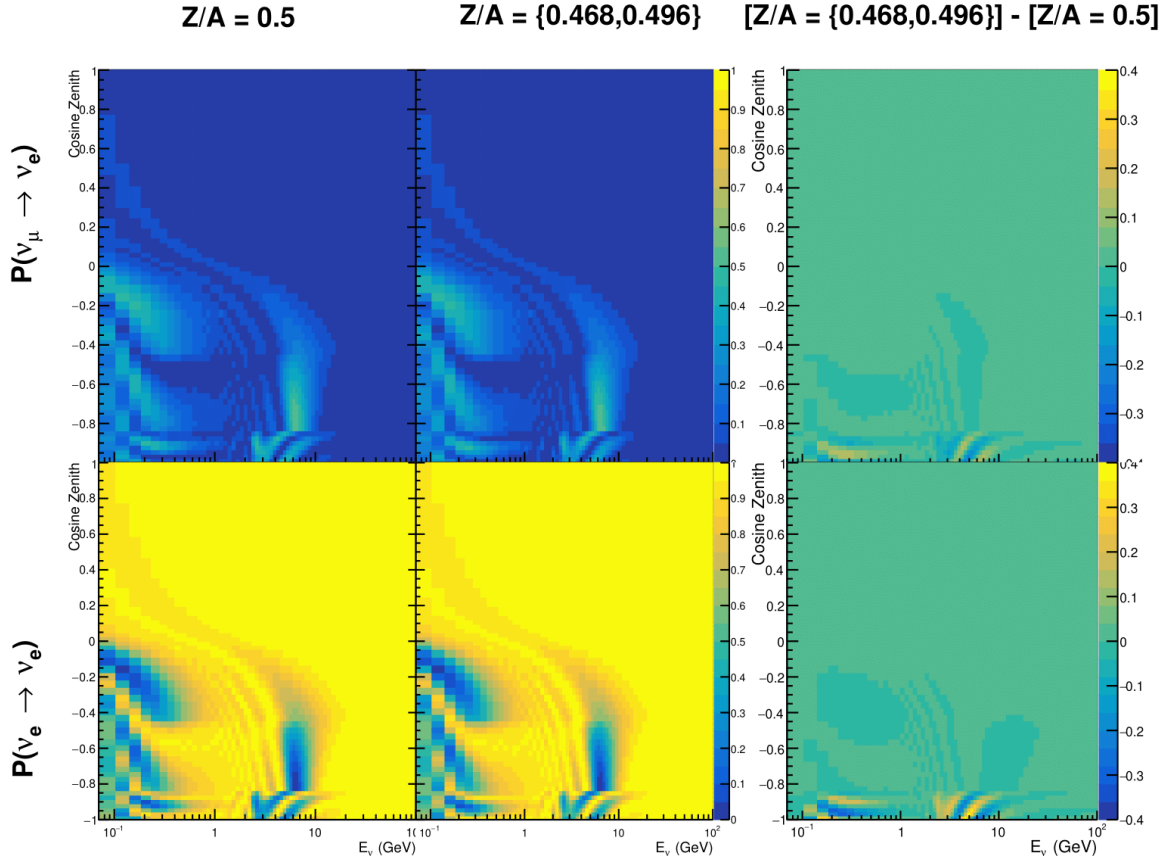


**Figure 5.14:** The oscillation probability,  $P(\nu_\mu \rightarrow \nu_e)$  (top row) and  $P(\nu_e \rightarrow \nu_\mu)$  (bottom row), given as a function of neutrino energy and zenith angle. The left column gives probabilities where the constant  $Z/A = 0.5$  approximation which is used in the official SK-only analysis. The middle column gives the probabilities where the more accurate  $Z/A = [0.468, 0.498]$  values as given in Table 5.2. The right column illustrates the difference in oscillation probability between the two different techniques.

1855 where  $t_i$  are the intersection points between each layer and  $t$  is the path length of  
 1856 the trajectory across the layer which is dependent upon  $\cos(\theta_Z)$ .

1857 The oscillation probability calculation speed is approximately linear in the number  
 1858 of layers invoked within the Earth model. Therefore a four-layer model is still utilized  
 1859 with the only difference to the above example being that the four-layer model used for  
 1860 each value of  $\cos(\theta_Z)$  is different. Following the method outlined in [190], a four-layer  
 1861 piecewise quadratic polynomial is fit to the PREM model for the four layers defined in

1862 Table 5.2. This fit was not performed by the author of the thesis and is documented  
1863 in [191]. The coefficients of the quadratic fit to each layer are given in Table 5.3 with  
1864 the final distribution illustrated in Figure 5.15. The quadratic approximation is clearly  
1865 much closer to the PREM model as compared to the constant density approximation.

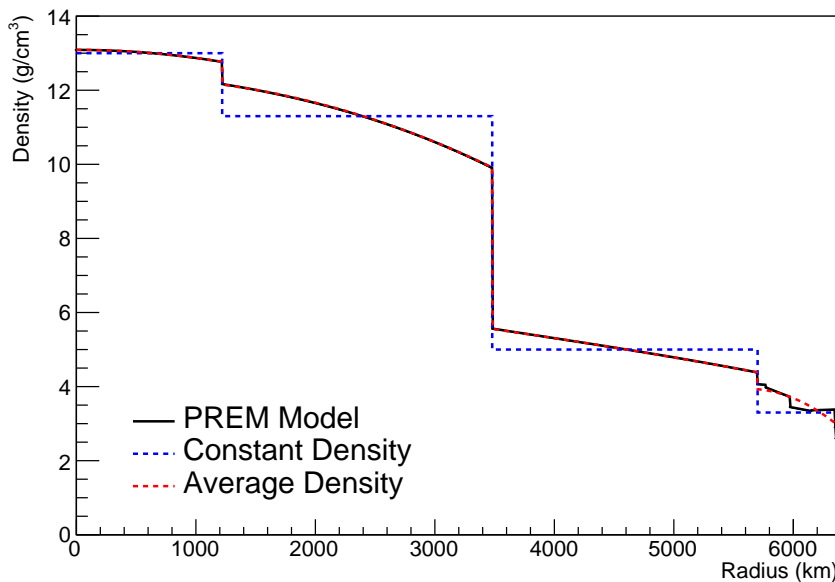


**Figure 5.15:** The density of the Earth given as a function of the radius, as given by the PREM model (Black), the constant density four-layer approximation (Blue), as used in the official SK-only analysis, and the quadratic approximation of the PREM model (Red).

Layer	Outer Radius [km]	Density [g/cm <sup>3</sup> ]
Inner Core	1220	$13.09 - 8.84x^2$
Outer Core	3480	$12.31 + 1.09x - 10.02x^2$
Lower Mantle	5701	$6.78 - 1.56x - 1.25x^2$
Transition Zone	6371	$-50.42 + 123.33x - 69.95x^2$

**Table 5.3:** The quadratic polynomial fits to the PREM model for four assumed layers of the PREM model. The fit to calculate the coefficients is given in [191], where  $x = R/R_{Earth}$ .

1866 The effect of using the average density per  $\cos(\theta_Z)$  model is highlighted in Fig-  
1867 ure 5.16. The slight discontinuity in the oscillation probability around  $\cos(\theta_Z) \sim -0.45$   
1868 in the fixed density model, which is due to the transition to mantle layer boundary, has

<sub>1869</sub> been reduced. This is expected as the difference in the density across this boundary is  
<sub>1870</sub> significantly smaller in the average density model as compared to the constant density  
<sub>1871</sub> model. Whilst the difference in density across the other layer transitions is reduced,  
<sub>1872</sub> there is still a significant difference. This means the discontinuities in the oscillation  
<sub>1873</sub> probabilities remain but are significantly reduced. However, as the average density  
<sub>1874</sub> approximation matches the PREM model well in this region, these discontinuities are  
<sub>1875</sub> due to the Earth model rather than an artifact of the oscillation calculation.

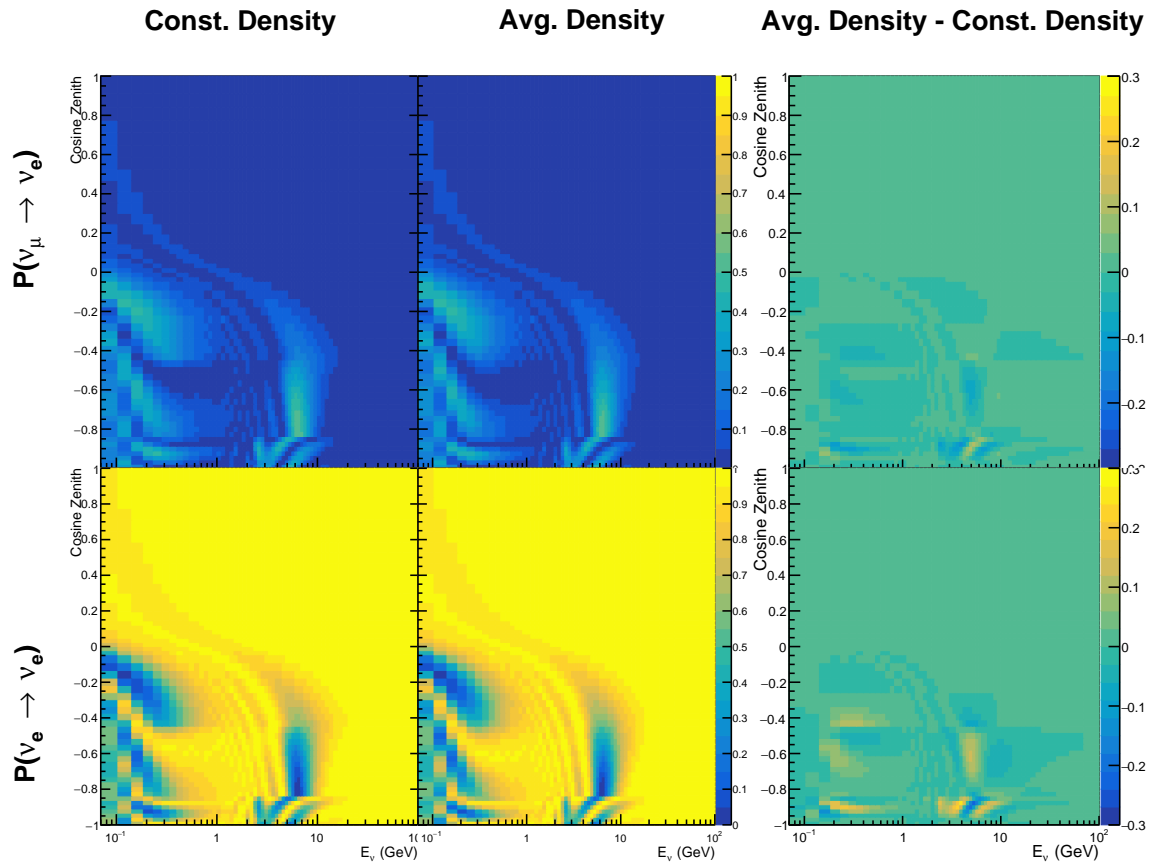


**Figure 5.16:** The oscillation probability,  $P(\nu_\mu \rightarrow \nu_e)$  (top row) and  $P(\nu_e \rightarrow \nu_\mu)$  (bottom row), given as a function of neutrino energy and zenith angle. The left column gives probabilities where the four-layer constant density approximation is used. The middle column gives the probabilities where the density is integrated over the trajectory, using the quadratic PREM approximation, for each  $\cos(\theta_Z)$  is used. The right column illustrates the difference in oscillation probability between the two different techniques.

## <sup>1876</sup> 5.5 Production Height Averaging

<sup>1877</sup> As discussed in section 5.1, the height at which the cosmic ray flux interacts in the  
<sup>1878</sup> atmosphere is not known on an event-by-event basis. The production height can  
<sup>1879</sup> vary from the Earth’s surface to 50km above that. The SK-only analysis methodol-  
<sup>1880</sup> ogy (described in section 5.2) for including the uncertainty on the production height  
<sup>1881</sup> is to include variations from the Honda model when pre-calculating the oscillation  
<sup>1882</sup> probabilities prior to the fit. This technique is not possible for this analysis which  
<sup>1883</sup> uses continuous oscillation parameters that can not be known prior to the fit. Conse-  
<sup>1884</sup> quently, an analytical averaging technique was developed in [191]. The author of this  
<sup>1885</sup> thesis was not responsible for the derivation of the technique but has performed the  
<sup>1886</sup> implementation and validation of the technique for this analysis alone.

<sup>1887</sup> The oscillation probability used within this analysis is based on [20]. The neutrino  
<sup>1888</sup> wavefunction in the vacuum Hamiltonian evolves in each layer of constant matter  
<sup>1889</sup> density via

$$i \frac{d\psi_j(t)}{dt} = \frac{m_j^2}{2E_\nu} \psi_j(t) - \sum_k \sqrt{2} G_F N_e U_{ej} U_{ke}^\dagger \psi_k(t), \quad (5.6)$$

<sup>1890</sup> where  $m_j^2$  is the square of the  $j^{th}$  vacuum eigenstate mass,  $E_\nu$  is the neutrino energy,  
<sup>1891</sup>  $G_F$  is Fermi’s constant,  $N_e$  is the electron number density and  $U$  is the PMNS matrix.  
<sup>1892</sup>  $N_e \rightarrow -N_e$  and  $\delta_{CP} \rightarrow -\delta_{CP}$  for antineutrino propagation.

<sup>1893</sup> Using the 20 production heights per MC neutrino event, provided as 5% percentiles  
<sup>1894</sup> from the Honda flux model, a production height distribution  $p_j(h|E_\nu, \cos \theta_Z)$  is built  
<sup>1895</sup> for each neutrino flavour  $j = \nu_e, \bar{\nu}_e, \nu_\mu, \bar{\nu}_\mu$ . In practice, a histogram is filled with 20  
<sup>1896</sup> evenly spaced bins in production height  $h$  between 0 and 50km. The neutrino energy

1897 and cosine zenith binning is the same as that provided in section 5.2. The average  
1898 production height,  $\bar{h} = \int dh \frac{1}{4} \sum_j p_j(h|E_\nu, \cos(\theta_Z))$ , is calculated. The production height  
1899 binning of this histogram is then translated into  $\delta t(h) = t(z, \bar{h}) - t(z, h)$ , where  $t(z, h)$   
1900 is the distance travelled along the trajectory.

1901 For the  $i^{th}$  traversed layer, the transition amplitude,  $D_i(t_{i+1}, t_i)$ , is computed. The  
1902 time ordered product of these is then used as the overall transition amplitude via

$$A(t_{n+1}, t_0) = D_n(t_{n+1}, t_n) \dots D_1(t_2, t_1) D_0(t_1, t_0), \quad (5.7)$$

1903 where,

$$\begin{aligned} D_n(t_{n+1}, t_n) &= \exp[-iH_n(t_{n+1} - t_n)] \\ &= \sum_{k=1}^3 C_k \exp[ia_k \delta t] \end{aligned} \quad (5.8)$$

1904 is expressed as a diagonalised time-dependent solution to the schrodinger equation.  
1905 The  $0^{th}$  layer is the propagation through the atmosphere and is the only term which  
1906 depends on the production height. Using the subsitution  $t_0 = t(\bar{h}) - \delta t(h)$ , it can be  
1907 shown that

$$D_0(t_1, t_0) = D_0(t_1, \bar{h}) D_0(\delta t). \quad (5.9)$$

1908 Thus Equation 5.7 becomes

$$\begin{aligned}
A(t_{n+1}, t_0) &= D_n(t_{n+1}, t_n) \dots D_1(t_2, t_1) D_0(t_1, \bar{h}) D(\delta t) \\
&= A(t_{n+1}, \bar{h}) \sum_{k=1}^3 C_k \exp[i a_k \delta t], \\
&= \sum_{k=1}^3 B_k \exp[i a_k \delta t].
\end{aligned} \tag{5.10}$$

<sup>1909</sup> The oscillation probability averaged over production height is calculated as

$$\begin{aligned}
\bar{P}(\nu_j \rightarrow \nu_i) &= \int d(\delta t) p_j(\delta t | E_\nu, \cos \theta_Z) P(\nu_j \rightarrow \nu_i) \\
&= \int d(\delta t) p_j(\delta t | E_\nu, \cos \theta_Z) A(t_{n+1}, t_0) A^*(t_{n+1}, t_0) \\
&= \sum_{km} (B_k)_{ij} (B_m)_{ij}^* \int d(\delta t) p_j(\delta t | E_\nu, \cos \theta_Z) \exp[i(a_k - a_m)\delta t]
\end{aligned} \tag{5.11}$$

<sup>1910</sup> In practice, implementation in CUDAProb3 [184] is relatively straightforward as  
<sup>1911</sup> the majority of these terms are already calculated in the standard oscillation calculation.  
<sup>1912</sup> Figure 5.17 illustrates the results of the production height averaging. As expected,  
<sup>1913</sup> the main effect is observed in the low-energy downward-going and horizontal-going  
<sup>1914</sup> events. Upward-going events have to travel the radius of the Earth,  $R_E = 6371\text{km}$ ,  
<sup>1915</sup> where the production height uncertainty is a small fraction of the total path length.

<sup>1916</sup>

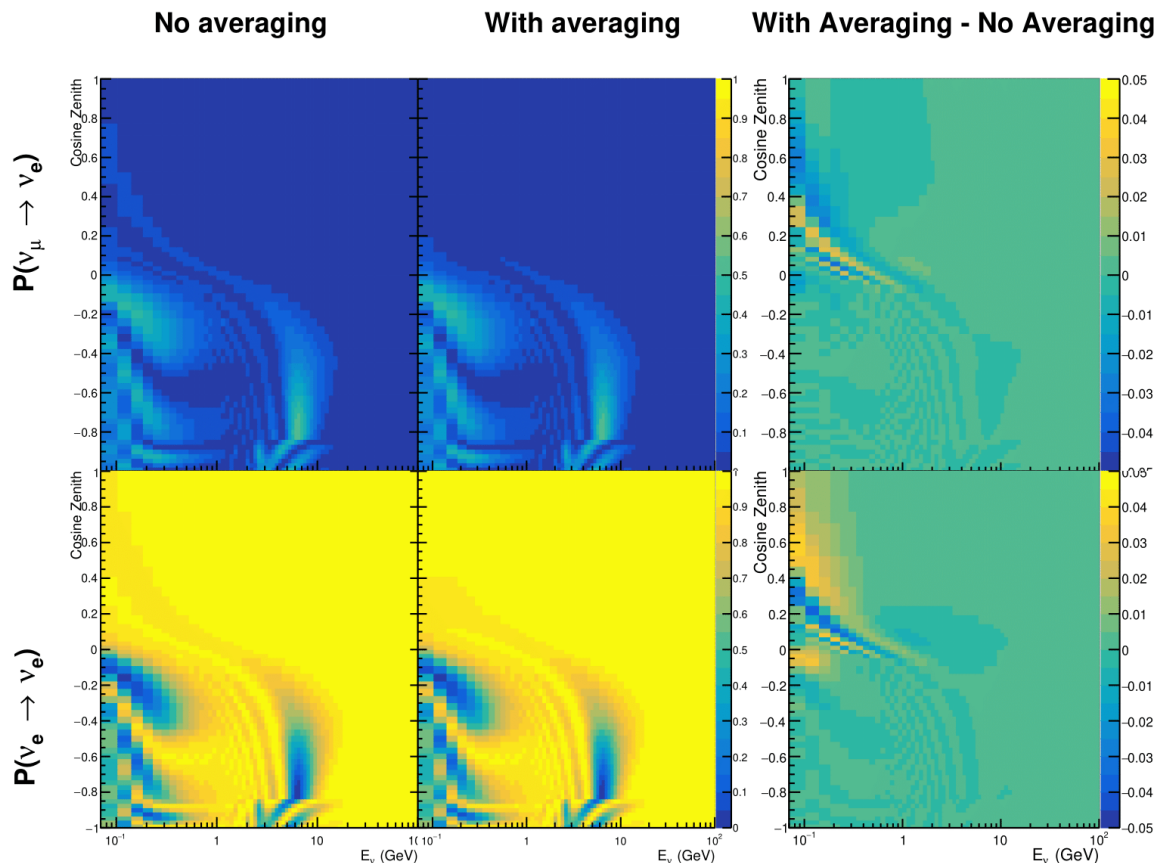


**Figure 5.17:** The oscillation probability,  $P(\nu_\mu \rightarrow \nu_e)$  (top row) and  $P(\nu_e \rightarrow \nu_\mu)$  (bottom row), given as a function of neutrino energy and zenith angle. The left column gives probabilities where a fixed production height of 25km is used. The middle column gives the probabilities where the production height is analytically averaged. The right column illustrates the difference in oscillation probability between the two different techniques.

# <sup>1917</sup> Bibliography

- <sup>1918</sup> [1] J. Chadwick, Verhandl. Dtsc. Phys. Ges. **16**, 383 (1914).
- <sup>1919</sup> [2] C. D. Ellis and W. A. Wooster, Proc. R. Soc. Lond. A Math. Phys. Sci. **117**, 109 (1927).
- <sup>1920</sup>
- <sup>1921</sup> [3] W. Pauli, Phys. Today **31N9**, 27 (1978).
- <sup>1922</sup> [4] E. Fermi, Z. Phys. **88**, 161 (1934).
- <sup>1923</sup> [5] F. Reines and C. L. Cowan, Phys. Rev. **92**, 830 (1953).
- <sup>1924</sup> [6] C. L. Cowan, F. Reines, F. B. Harrison, H. W. Kruse, and A. D. McGuire, Science **124**, 103 (1956), <http://science.sciencemag.org/content/124/3212/103.full.pdf>.
- <sup>1925</sup>
- <sup>1926</sup> [7] G. Danby *et al.*, Phys. Rev. Lett. **9**, 36 (1962).
- <sup>1927</sup> [8] K. Kodama *et al.*, Physics Letters B **504**, 218 (2001).
- <sup>1928</sup> [9] LSND, A. Aguilar-Arevalo *et al.*, Phys. Rev. **D64**, 112007 (2001), hep-ex/0104049.
- <sup>1929</sup> [10] MiniBooNE Collaboration, A. A. Aguilar-Arevalo *et al.*, Phys. Rev. Lett. **110**, 161801 (2013).
- <sup>1930</sup>
- <sup>1931</sup> [11] Planck Collaboration *et al.*, aap **641** (2020).
- <sup>1932</sup> [12] B. Pontecorvo, Sov. Phys. JETP **26**, 984 (1968), [Zh. Eksp. Teor. Fiz. 53, 1717 (1967)].
- <sup>1933</sup> [13] B. Pontecorvo, Sov. Phys. JETP **7**, 172 (1958), [Zh. Eksp. Teor. Fiz. 34, 247 (1957)].
- <sup>1934</sup> [14] M. Kobayashi and T. Maskawa, Progress of Theoretical Physics **49**, 652 (1973).
- <sup>1935</sup> [15] N. Cabibbo, Phys. Rev. Lett. **10**, 531 (1963).
- <sup>1936</sup> [16] A. M. and, Journal of Physics: Conference Series **587**, 012030 (2015).
- <sup>1937</sup> [17] A. Y. Smirnov, (2003).
- <sup>1938</sup> [18] S. Mikheyev and A. Smirnov, Soviet Journal of Nuclear Physics **42**, 913 (1985).
- <sup>1939</sup> [19] L. Wolfenstein, Phys. Rev. D **17**, 2369 (1978).
- <sup>1940</sup> [20] V. D. Barger, K. Whisnant, S. Pakvasa, and R. J. N. Phillips, Phys. Rev. D **22**, 2718 (1980).
- <sup>1941</sup>

- [21] The Super-Kamiokande Collaboration, Y. Ashie *et al.*, Phys. Rev. Lett. **93**, 101801 (2004).
- [22] SNO Collaboration, Q. R. Ahmad *et al.*, Phys. Rev. Lett. **89**, 011301 (2002).
- [23] 2015 Nobel prize in Physics as listed by Nobelprize.org, [https://www.nobelprize.org/nobel\\_prizes/physics/laureates/2015/](https://www.nobelprize.org/nobel_prizes/physics/laureates/2015/), Accessed: 22-06-2022.
- [24] J. A. Formaggio and G. P. Zeller, Rev. Mod. Phys. **84**, 1307 (2012), 1305.7513.
- [25] A. Bellerive, Int. J. Mod. Phys. A **19**, 1167 (2004).
- [26] R. Davis, D. S. Harmer, and K. C. Hoffman, Phys. Rev. Lett. **20**, 1205 (1968).
- [27] N. Vinyoles *et al.*, Astrophys. J. **835**, 202 (2017).
- [28] V. Gribov and B. Pontecorvo, Phys. Lett. B **28**, 493 (1969).
- [29] K. S. Hirata *et al.*, Phys. Rev. Lett. **63**, 16 (1989).
- [30] W. Hampel *et al.*, Phys. Lett. B **447**, 127 (1999).
- [31] SAGE Collaboration, J. N. Abdurashitov *et al.*, Phys. Rev. C **60**, 055801 (1999).
- [32] Q. R. Ahmad *et al.*, Phys. Rev. Lett. **89** (2002).
- [33] Borexino Collaboration, Nature **562**, 505 (2018).
- [34] B. Aharmim *et al.*, Astrophys. J. **653**, 1545 (2006).
- [35] M. Agostini *et al.*, (2020).
- [36] S. Andringa *et al.*, Adv. High Energy Phys. **2016**, 1 (2016).
- [37] J. F. Beacom *et al.*, Chin. phys. C **41**, 023002 (2017).
- [38] F. An *et al.*, J. Phys. G Nucl. Part. Phys. **43**, 030401 (2016).
- [39] J. Aalbers *et al.*, (2020), 2006.03114.
- [40] T. K. Gaisser and M. Honda, (2002).
- [41] G. D. Barr, T. K. Gaisser, P. Lipari, S. Robbins, and T. Stanev, Physical Review D **70** (2004).
- [42] M. Honda, T. Kajita, K. Kasahara, S. Midorikawa, and T. Sanuki, Physical Review

- 1968 D **75** (2007).
- 1969 [43] M. Honda, T. Kajita, K. Kasahara, and S. Midorikawa, Phys. Rev. D **70**, 043008 (2004).
- 1970
- 1971 [44] M. Honda, T. Kajita, K. Kasahara, and S. Midorikawa, Phys. Rev. D **83**, 123001 (2011).
- 1972
- 1973 [45] A. Fasso, A. Ferrari, P. R. Sala, and J. Ranft, (2001).
- 1974 [46] Y. Ashie *et al.*, Physical Review D **71** (2005).
- 1975 [47] F. Reines *et al.*, Phys. Rev. Lett. **15**, 429 (1965).
- 1976 [48] D. Casper *et al.*, Phys. Rev. Lett. **66**, 2561 (1991).
- 1977 [49] K. S. Hirata *et al.*, Phys. Lett. B **280**, 146 (1992).
- 1978 [50] Z. Li *et al.*, Physical Review D **98** (2018).
- 1979 [51] Kamiokande Collaboration *et al.*, (2017).
- 1980 [52] T2K Collaboration, Nature **580**, 339 (2020).
- 1981 [53] M. A. Acero *et al.*, Phys. Rev. Lett. **123**, 151803 (2019).
- 1982 [54] M. G. Aartsen *et al.*, Phys. Rev. Lett. **120** (2018).
- 1983 [55] P. Adamson *et al.*, Phys. Rev. Lett. **112** (2014).
- 1984 [56] M. S. Athar *et al.*, Progress in Particle and Nuclear Physics **124**, 103947 (2022).
- 1985 [57] G. Danby *et al.*, Phys. Rev. Lett. **9**, 36 (1962).
- 1986 [58] K. Abe *et al.*, Physical Review D **87** (2013).
- 1987 [59] MINOS Collaboration, D. G. Michael *et al.*, Phys. Rev. Lett. **97**, 191801 (2006).
- 1988 [60] G. Danby *et al.*, Phys. Rev. Lett. **9**, 36 (1962).
- 1989 [61] NOvA Collaboration, M. A. Acero *et al.*, Phys. Rev. Lett. **123**, 151803 (2019).
- 1990 [62] B. Abi, R. Acciarri, M. A. Acero, and G. e. a. Adamov, Eur. Phys. J. C Part. Fields **80** (2020).
- 1991
- 1992 [63] Hyper-Kamiokande Proto-Collaboration *et al.*, Prog. Theor. Exp. Phys. **2015**, 53C02 (2015).
- 1993

- 1994 [64] C. Blanco, D. Hooper, and P. Machado, Physical Review D **101** (2020).
- 1995 [65] MicroBooNE Collaboration *et al.*, Search for an Excess of Electron Neutrino  
1996 Interactions in MicroBooNE Using Multiple Final State Topologies, 2021.
- 1997 [66] KARMEN Collaboration, B. Armbruster *et al.*, Phys. Rev. D **65**, 112001 (2002).
- 1998 [67] S.-B. Kim, T. Lasserre, and Y. Wang, Adv. High Energy Phys. **2013**, 1 (2013).
- 1999 [68] M. Sajjad Athar *et al.*, Prog. Part. Nucl. Phys. **124**, 103947 (2022), 2111.07586.
- 2000 [69] K. Abe *et al.*, Nucl. Instrum. Methods Phys. Res. A **1027**, 166248 (2022).
- 2001 [70] F. P. An *et al.*, Phys. Rev. Lett. **108**, 171803 (2012).
- 2002 [71] RENO Collaboration, J. K. Ahn *et al.*, Phys. Rev. Lett. **108**, 191802 (2012).
- 2003 [72] Double Chooz Collaboration, Y. Abe *et al.*, Phys. Rev. Lett. **108**, 131801 (2012).
- 2004 [73] J. Collaboration *et al.*, TAO Conceptual Design Report: A Precision Measurement  
2005 of the Reactor Antineutrino Spectrum with Sub-percent Energy Resolution, 2020,  
2006 2005.08745.
- 2007 [74] for the RENO Collaboration, New results from RENO and the 5 MeV excess,  
2008 AIP Publishing LLC, 2015.
- 2009 [75] Y. Abe *et al.*, Journal of High Energy Physics **2014** (2014).
- 2010 [76] Daya Bay Collaboration, D. Adey *et al.*, Phys. Rev. Lett. **123**, 111801 (2019).
- 2011 [77] M. P. Decowski, Nucl. Phys. B. **908**, 52 (2016).
- 2012 [78] The KamLAND Collaboration, A. Gando *et al.*, Phys. Rev. D **83**, 052002 (2011).
- 2013 [79] Y. Fukuda *et al.*, Phys. Rev. Lett. **81**, 1562 (1998).
- 2014 [80] K. Abe *et al.*, Nuclear Instruments and Methods in Physics Research Section  
2015 A: Accelerators, Spectrometers, Detectors and Associated Equipment **737**, 253  
2016 (2014).
- 2017 [81] S. Fukuda *et al.*, Nucl. Instrum. Methods Phys. Res. A **501**, 418 (2003).
- 2018 [82] Y. Itow *et al.*, (2001).
- 2019 [83] M. Jiang *et al.*, Prog. Theor. Exp. Phys. **2019** (2019).

- 2020 [84] S. Fukuda *et al.*, Nuclear Instruments and Methods in Physics Research Section  
2021 A: Accelerators, Spectrometers, Detectors and Associated Equipment **501**, 418  
2022 (2003), <http://www.sciencedirect.com/science/article/pii/S016890020300425X>.
- 2023 [85] Y. Nakano *et al.*, Nucl. Instrum. Methods Phys. Res. A **977**, 164297 (2020).
- 2024 [86] Hamamatsu, Hamamatsu Photonics Photomultiplier Tubes Handbook.
- 2025 [87] K. Abe *et al.*, Nucl. Instrum. Methods Phys. Res. A **1027**, 166248 (2022).
- 2026 [88] J. F. Beacom and M. R. Vagins, Phys. Rev. Lett. **93**, 171101 (2004).
- 2027 [89] L. Marti *et al.*, Nucl. Instrum. Methods Phys. Res. A **959**, 163549 (2020).
- 2028 [90] L. Marti *et al.*, (2019).
- 2029 [91] T. Tanimori *et al.*, IEEE Transactions on Nuclear Science **36**, 497 (1989).
- 2030 [92] Super-Kamiokande Collaboration, J. Hosaka *et al.*, Phys. Rev. D **73**, 112001  
2031 (2006).
- 2032 [93] H. Nishino *et al.*, Nucl. Instrum. Methods Phys. Res. A **610**, 710 (2009).
- 2033 [94] S. Yamada *et al.*, IEEE Transactions on Nuclear Science **57**, 428 (2010).
- 2034 [95] S. Yamada, Y. Hayato, Y. Obayashi, and M. Shiozawa, New online system  
2035 without hardware trigger for the Super-Kamiokande experiment, in *2007 IEEE*  
2036 *Nuclear Science Symposium Conference Record*, IEEE, 2007.
- 2037 [96] G. Carminati, Phys. Procedia **61**, 666 (2015).
- 2038 [97] P. A. Čerenkov, Phys. Rev. **52**, 378 (1937).
- 2039 [98] I. Frank and I. Tamm, Coherent visible radiation of fast electrons passing  
2040 through matter, in *Selected Papers*, pp. 29–35, Springer Berlin Heidelberg, Berlin,  
2041 Heidelberg, 1991.
- 2042 [99] The T2K Collaboration, KEK Proposal (2001),  
2043 <http://neutrino.kek.jp/jhfnu/loi/loi.v2.030528.pdf>.
- 2044 [100] Y. Itow *et al.*, (2001), hep-ex/0106019.
- 2045 [101] The K2K Collaboration and S. H. Ahn, (2001), hep-ex/0103001.
- 2046 [102] The T2K Collaboration, KEK Proposal (2006), <http://j->

- 2047 parc.jp/researcher/Hadron/en/pac\_0606/pdf/p11-Nishikawa.pdf.
- 2048 [103] T2K Collaboration, K. Abe *et al.*, Phys. Rev. Lett. **112**, 061802 (2014),  
2049 <https://link.aps.org/doi/10.1103/PhysRevLett.112.061802>.
- 2050 [104] NINJA Collaboration, T. Fukuda *et al.*, Proposal for precise measurement of  
2051 neutrino-water cross-section in NINJA physics run, Proposal for J-PARC and  
2052 KEK, 2017.
- 2053 [105] T. Ovsianikova *et al.*, Physics of Particles and Nuclei **48**, 1014 (2017),  
2054 <https://doi.org/10.1134/S1063779617060478>.
- 2055 [106] M. Antonova *et al.*, Journal of Instrumentation **12**, C07028 (2017),  
2056 <http://stacks.iop.org/1748-0221/12/i=07/a=C07028>.
- 2057 [107] The T2K Collaboration, K. Abe *et al.*, Phys. Rev. D **102**, 012007 (2020).
- 2058 [108] K. Abe *et al.*, Progress of Theoretical and Experimental Physics **2021** (2021).
- 2059 [109] The T2K Collaboration, K. Abe *et al.*, Nuclear Instruments  
2060 and Methods in Physics Research Section A: Accelerators, Spectrometers,  
2061 Detectors and Associated Equipment **659**, 106 (2011),  
2062 <http://www.sciencedirect.com/science/article/pii/S0168900211011910>.
- 2063 [110] K. Matsuoka *et al.*, Nuclear Instruments and Methods in Physics Research Section  
2064 A: Accelerators, Spectrometers, Detectors and Associated Equipment **624**, 591  
2065 (2010), <http://www.sciencedirect.com/science/article/pii/S016890021002098X>.
- 2066 [111] K. Abe *et al.*, Phys. Rev. D. **103** (2021).
- 2067 [112] T. Vladislavljevic, *Predicting the T2K neutrino flux and measuring oscillation parameters* Springer theses, 1 ed. (Springer Nature, Cham, Switzerland, 2020).
- 2069 [113] D. Beavis, A. Carroll, and I. Chiang, (1995).
- 2070 [114] P.-A. Amaudruz *et al.*, Nuclear Instruments and Methods in Physics Research  
2071 Section A: Accelerators, Spectrometers, Detectors and Associated Equipment  
2072 **696**, 1 (2012).
- 2073 [115] N. Abgrall *et al.*, Nuclear Instruments and Methods in Physics Research Section  
2074 A: Accelerators, Spectrometers, Detectors and Associated Equipment **637**, 25  
2075 (2011).

- 2076 [116] S. Assylbekov *et al.*, Nuclear Instruments and Methods in Physics Research  
2077 Section A: Accelerators, Spectrometers, Detectors and Associated Equipment  
2078 **686**, 48 (2012).
- 2079 [117] D. Allan *et al.*, Journal of Instrumentation **8**, P10019 (2013).
- 2080 [118] F. Vannucci, Advances in High Energy Physics **2014**, 1 (2014).
- 2081 [119] UA1 magnet sets off for a second new life, 2022.
- 2082 [120] S. Aoki *et al.*, Nuclear Instruments and Methods in Physics Research Section  
2083 A: Accelerators, Spectrometers, Detectors and Associated Equipment **698**, 135  
2084 (2013).
- 2085 [121] K. Suzuki *et al.*, Progress of Theoretical and Experimental Physics **2015**, 53C01  
2086 (2015).
- 2087 [122] S. Brooks, A. Gelman, G. L. Jones, and X.-L. Meng, *Handbook of Markov Chain  
Monte Carlo* (CRC Press, 2011).
- 2089 [123] W. R. Gilks, S. Richardson, and D. J. Spiegelhalter, *Markov Chain Monte Carlo in  
Practice* (Chapman & Hall/CRC Interdisciplinary Statistics, 1995).
- 2091 [124] C. Wret, *Minimising systematic uncertainties in the T2K experiment using near-  
detector and external data*, PhD thesis, Imperial College London, 2018.
- 2093 [125] K. E. Duffy, *Measurement of the Neutrino Oscillation Parameters  $\sin^2 \theta_{23}$ ,  $\Delta m_{32}^2$ ,  
2094  $\sin^2 \theta_{13}$ , and  $\delta_{CP}$  in Neutrino and Antineutrino Oscillation at T2K*, PhD thesis, Oriel  
2095 College, University of Oxford, 2016.
- 2096 [126] T. Bayes, Rev., Phil. Trans. Roy. Soc. Lond. **53**, 370 (1764).
- 2097 [127] N. Metropolis, A. W. Rosenbluth, M. N. Rosenbluth, A. H. Teller, and E. Teller,  
2098 Journal of Chemical Physics **21** (1970).
- 2099 [128] W. K. Hastings, Biometrika **57** (1970).
- 2100 [129] J. Dunkley, M. Bucher, P. G. Ferreira, K. Moodley, and C. Skordis, Mon. Not. R.  
2101 Astron. Soc. **356**, 925 (2005).
- 2102 [130] Particle Data Group *et al.*, Prog. Theor. Exp. Phys. **2020** (2020).
- 2103 [131] H. Jeffreys, *The Theory of Probability* Oxford Classic Texts in the Physical Sciences  
2104 (, 1939).

- 2105 [132] R. E. Kass and A. E. Raftery, *J. Am. Stat. Assoc.* **90**, 773 (1995).
- 2106 [133] T. Böhlen *et al.*, Nuclear Data Sheets **120**, 211 (2014),  
2107 <http://www.sciencedirect.com/science/article/pii/S0090375214005018>.
- 2108 [134] R. Brun *et al.*, *GEANT: Detector Description and Simulation Tool; Oct 1994*CERN  
2109 Program Library (CERN, Geneva, 1993), <http://cds.cern.ch/record/1082634>,  
2110 Long Writeup W5013.
- 2111 [135] T2K Collaboration, K. Abe *et al.*, *Phys. Rev. D* **87**, 012001 (2013).
- 2112 [136] C. Zeitnitz and T. Gabriel, Nuclear Instruments and Meth-  
2113 ods in Physics Research Section A: Accelerators, Spectrom-  
2114 eters, Detectors and Associated Equipment **349**, 106 (1994),  
2115 <http://www.sciencedirect.com/science/article/pii/0168900294906130>.
- 2116 [137] N. Abgrall *et al.*, *Physical Review C* **84** (2011).
- 2117 [138] N. Abgrall *et al.*, *Physical Review C* **85** (2012).
- 2118 [139] N. Abgrall *et al.*, Nuclear Instruments and Methods in Physics Research Section  
2119 A: Accelerators, Spectrometers, Detectors and Associated Equipment **701**, 99  
2120 (2013), <http://www.sciencedirect.com/science/article/pii/S016890021201234X>.
- 2121 [140] HARP Collaboration, M. Apollonio *et al.*, *Phys. Rev. C* **80**, 035208 (2009),  
2122 <https://link.aps.org/doi/10.1103/PhysRevC.80.035208>.
- 2123 [141] A. Fiorentini *et al.*, *T2K Technical Note* **217** (2017).
- 2124 [142] B. Blau *et al.*, *Nuclear Physics B - Proceedings Supplements* **113**, 125 (2002).
- 2125 [143] S. Haino *et al.*, *Physics Letters B* **594**, 35 (2004).
- 2126 [144] NASA, U.S. Standard Atmosphere, 1976, 1976.
- 2127 [145] S. Roesler, R. Engel, and J. Ranft, The Monte Carlo Event Generator DPMJET-III,  
2128 in *Advanced Monte Carlo for Radiation Physics, Particle Transport Simulation and*  
2129 *Applications*, pp. 1033–1038, Springer Berlin Heidelberg, 2001.
- 2130 [146] K. Niita *et al.*, *Radiation Measurements* **41**, 1080 (2006).
- 2131 [147] T. Sanuki *et al.*, *Physics Letters B* **541**, 234 (2002).
- 2132 [148] P. Achard *et al.*, *Physics Letters B* **598**, 15 (2004).

- <sup>2133</sup> [149] Y. Hayato and L. Pickering, *The European Physical Journal Special Topics* **230**, 4469 (2021).
- <sup>2134</sup>
- <sup>2135</sup> [150] Y. Hayato, *Acta Physica Polonica B* **40** (2009).
- <sup>2136</sup> [151] C. L. Smith, *Physics Reports* **3**, 261 (1972),  
<sup>2137</sup> <http://www.sciencedirect.com/science/article/pii/0370157372900105>.
- <sup>2138</sup> [152] O. Benhar, A. Fabrocini, and S. Fantoni, *Nuclear Physics A* **497**, 423 (1989).
- <sup>2139</sup> [153] R. Bradford, A. Bodek, H. Budd, and J. Arrington, *Nu-*  
<sup>2140</sup> *clear Physics B - Proceedings Supplements* **159**, 127 (2006),  
<sup>2141</sup> <http://www.sciencedirect.com/science/article/pii/S0920563206005184>,  
<sup>2142</sup> *Proceedings of the 4th International Workshop on Neutrino-Nucleus Interac-*  
<sup>2143</sup> *tions in the Few-GeV Region.*
- <sup>2144</sup> [154] A. A. Aguilar-Arevalo *et al.*, *Physical Review D* **81** (2010).
- <sup>2145</sup> [155] R. Gran, J. Nieves, F. Sanchez, and M. J. V. Vacas, *Phys. Rev. D* **88**, 113007 (2013),  
<sup>2146</sup> <https://link.aps.org/doi/10.1103/PhysRevD.88.113007>.
- <sup>2147</sup> [156] C. Berger and L. M. Sehgal, *Phys. Rev. D* **76**, 113004 (2007).
- <sup>2148</sup> [157] C. Berger and L. M. Sehgal, *Phys. Rev. D* **79**, 053003 (2009),  
<sup>2149</sup> <https://link.aps.org/doi/10.1103/PhysRevD.79.053003>.
- <sup>2150</sup> [158] T. Sjöstrand, *Computer Physics Communications* **82**, 74 (1994).
- <sup>2151</sup> [159] C. Bronner and M. Hartz, Tuning of the Charged Hadrons Multiplicities for Deep  
<sup>2152</sup> Inelastic Interactions in NEUT, in *Proceedings of the 10th International Workshop on*  
<sup>2153</sup> *Neutrino-Nucleus Interactions in Few-GeV Region (NuInt15)*, *Journal of the Physical*  
<sup>2154</sup> *Society of Japan*, 2016.
- <sup>2155</sup> [160] M. Glück, E. Reya, and A. Vogt, *The European Physical Journal C* **5**, 461 (1998).
- <sup>2156</sup> [161] A. Bodek and U.-k. Yang, Axial and Vector Structure Functions for Electron- and  
<sup>2157</sup> Neutrino- Nucleon Scattering Cross Sections at all  $Q^2$  using Effective Leading  
<sup>2158</sup> order Parton Distribution Functions, 2010.
- <sup>2159</sup> [162] A. Bodek and U.-K. Yang, (2010).
- <sup>2160</sup> [163] S. Gollapinni, (2016).
- <sup>2161</sup> [164] E. S. P. Guerra *et al.*, *Phys. Rev. D* **99**, 052007 (2019).

- <sup>2162</sup> [165] GEANT4, S. Agostinelli *et al.*, Nucl. Instrum. Meth. **A506**, 250 (2003).
- <sup>2163</sup> [166] R. Brun, F. Bruyant, M. Maire, A. C. McPherson, and P. Zanarini, (1987).
- <sup>2164</sup> [167] K. Abe *et al.*, Physical Review Letters **121** (2018).
- <sup>2165</sup> [168] K. Abe *et al.*, Physical Review D **91** (2015).
- <sup>2166</sup> [169] R. Patterson *et al.*, Nuclear Instruments and Methods in Physics Research Section A: Accelerators, Spectrometers, Detectors and Associated Equipment **608**, 206 (2009).
- <sup>2169</sup> [170] e. a. S. Berkman, T2K Technical Note **146** (2013).
- <sup>2170</sup> [171] e. a. A. Himmel, T2K Technical Note **219** (2015).
- <sup>2171</sup> [172] F. a. James, (1998), CERN Program Library Long Writeups.
- <sup>2172</sup> [173] e. a. D. Barrow, T2K Technical Note **326** (2020).
- <sup>2173</sup> [174] A. Maghrabi, A. Aldosari, and M. Almutairi, Advances in Space Research **68**, 2941 (2021).
- <sup>2175</sup> [175] Super-Kamiokande Collaboration, K. Abe *et al.*, Phys. Rev. D **97**, 072001 (2018), <https://link.aps.org/doi/10.1103/PhysRevD.97.072001>.
- <sup>2177</sup> [176] Particle Data Group, J. Beringer *et al.*, Phys. Rev. D **86**, 010001 (2012).
- <sup>2178</sup> [177] Y. N. and, Journal of Physics: Conference Series **888**, 012191 (2017).
- <sup>2179</sup> [178] M. Jiang, *Study of the neutrino mass hierarchy with the atmospheric neutrino data collected in Super-Kamiokande IV*, PhD thesis, Kyoto University, 2019.
- <sup>2181</sup> [179] P. Machado, H. Schulz, and J. Turner, Physical Review D **102** (2020).
- <sup>2182</sup> [180] T2K Collaboration, K. Abe *et al.*, Phys. Rev. Lett. **112**, 181801 (2014).
- <sup>2183</sup> [181] R. Wendell, *Three Flavor Oscillation Analysis of Atmospheric Neutrinos in Super-Kamiokande*, PhD thesis, University of North Carolina, 2008.
- <sup>2185</sup> [182] R. G. Calland, A. C. Kaboth, and D. Payne, **9**, P04016 (2014).
- <sup>2186</sup> [183] R. Wendell, <http://www.phy.duke.edu/raw22/public/Prob3++/>.
- <sup>2187</sup> [184] F. Kallenborn, C. Hundt, S. Böser, and B. Schmidt, Computer Physics Communications **234**, 235 (2019).

- <sup>2189</sup> [185] L. Warsame, MaCh3 Analysis Progress.
- <sup>2190</sup> [186] A. M. Dziewonski and D. L. Anderson, Phys. Earth Planet. Inter. **25**, 297 (1981).
- <sup>2191</sup> [187] S. Bourret, J. A. B. Coelho, and V. V. E. and, Journal of Physics: Conference Series **888**, 012114 (2017).
- <sup>2192</sup>
- <sup>2193</sup> [188] C. Rott, A. Taketa, and D. Bose, Scientific Reports **5** (2015).
- <sup>2194</sup> [189] K. Hagiwara, N. Okamura, and K. ichi Senda, Journal of High Energy Physics **2011** (2011).
- <sup>2195</sup>
- <sup>2196</sup> [190] D. Typinski, Earth Gravity, <http://www.typnet.net/Essays/EarthGravGraphics/EarthGrav.pdf>, Accessed: 24-06-2022.
- <sup>2197</sup>
- <sup>2198</sup> [191] e. a. D. Barrow, T2K Technical Note **425** (2022).

# <sup>2199</sup> List of Figures

<sup>2200</sup>	1.1	The cross-section of neutrinos from various natural and man-made sources as a function of neutrino energy. Taken from [24] . . . . .	10
<sup>2201</sup>			
<sup>2202</sup>	1.2	The solar neutrino flux as a function of neutrino energy for various fusion reactions and decay chains as predicted by the Standard Solar Model. Taken from [25]. . . . .	11
<sup>2203</sup>			
<sup>2204</sup>			
<sup>2205</sup>	1.3	Left panel: The atmospheric neutrino flux for different neutrino flavours as a function of neutrino energy as predicted by the 2007 Honda model (“This work”) [42], the 2004 Honda model (“HKKM04”) [43], the Bartol model [41] and the FLUKA model [45]. Right panel: The ratio of the muon to electron neutrino flux as predicted by all the quoted models. Both figures taken from [42]. . . . .	13
<sup>2206</sup>			
<sup>2207</sup>			
<sup>2208</sup>			
<sup>2209</sup>			
<sup>2210</sup>			
<sup>2211</sup>	1.4	A diagram illustrating the definition of zenith angle as used in the Super Kamiokande experiment [46]. . . . .	13
<sup>2212</sup>			
<sup>2213</sup>	1.5	Prediction of $\nu_e, \bar{\nu}_e, \nu_\mu, \bar{\nu}_\mu$ fluxes as a function of zenith angle as calculated by the HKKM model [44]. The left, middle and right panels represent three values of neutrino energy, 0.32GeV, 1.0GeV and 3.2GeV respectively. Predictions for other models including Bartol [41], Honda [42] and FLUKA [45] are given in [46]. . . . .	14
<sup>2214</sup>			
<sup>2215</sup>			
<sup>2216</sup>			
<sup>2217</sup>			
<sup>2218</sup>	1.6	Constraints on the atmospheric oscillation parameters, $\sin^2(\theta_{23})$ and $\Delta m_{23}^2$ , from atmospheric and long baseline experiments: SK [51], T2K [52], NO $\nu$ A [53], IceCube [54] and MINOS [55]. Figure taken from [56].	15
<sup>2219</sup>			
<sup>2220</sup>			
<sup>2221</sup>	1.7	Reactor electron antineutrino fluxes for $^{235}\text{U}$ (Black), $^{238}\text{U}$ (Green), $^{239}\text{Pu}$ (Purple), and $^{241}\text{Pu}$ (Orange) isotopes. The inverse $\beta$ -decay cross-section (Blue) and corresponding measurable neutrino spectrum (Red) are also given. Top panel: Schematic of Inverse $\beta$ -decay interaction including the eventual capture of the emitted neutron. This capture emits a $\gamma$ -ray which provides a second signal of the event. Taken from [68]. . . . .	18
<sup>2222</sup>			
<sup>2223</sup>			
<sup>2224</sup>			
<sup>2225</sup>			
<sup>2226</sup>			
<sup>2227</sup>	2.1	A schematic diagram of the Super-Kamiokande Detector. Taken from [82].	22

2228	2.2	The location of “standard PMTs” (red) inside the SK detector. Taken from [80]. . . . .	26
2229	2.3	Schematic view of the data flow through the data acquisition and online system. Taken from [94]. . . . .	29
2232	2.4	The cross-section view of the Tokai to Kamioka experiment illustrating the beam generation facility at J-PARC, the near detector situated at a baseline of 280m and the Super Kamiokande far detector situated 295km from the beam target. . . . .	33
2233	2.5	The near detector suite for the T2K experiment showing the ND280 and INGRID detectors. The distance between the detectors and the beam target is 280m. . . . .	34
2236	2.6	Top panel: Bird’s eye view of the most relevant part of primary and sec- ondary beamline used within the T2K experiment. The primary beam- line is the main-ring proton synchrotron, kicker magnet, and graphite target. The secondary beamline consists of the three focusing horns, decay volume, and beam dump. Figure taken from [109]. Bottom panel: The side-view of the secondary beamline including the focusing horns, beam dump and neutrino detectors. Figure taken from [110]. . . . .	35
2240	2.7	The Monte Carlo prediction of the energy spectrum for each flavour of neutrino ( $\nu_e$ , $\bar{\nu}_e$ , $\nu_\mu$ and $\bar{\nu}_\mu$ ) in the neutrino dominated beam FHC mode (Left) and antineutrino dominated beam RHC mode (Right) expected at SK. Taken from [111]. . . . .	37
2244	2.8	Top panel: T2K muon neutrino disappearance probability as a function of neutrino energy. Middle panel: T2K electron neutrino appearance probability as a function of neutrino energy. Bottom panel: The neutrino flux distribution for three different off-axis angles (Arbitrary units) as a function of neutrino energy. . . . .	38
2245	2.9	The components of the ND280 detector. The neutrino beam travels from left to right. Taken from [109]. . . . .	39
2257	2.10	Comparison of data to Monte Carlo prediction of integrated deposited energy as a function of track length for particles that stopped in FGD1. Taken from [114]. . . . .	41

2260	2.11 Schematic design of a Time Projection Chamber detector. Taken from [115].	42
2261	2.12 The distribution of energy loss as a function of reconstructed momentum for charged particles passing through the TPC, comparing data to Monte Carlo prediction. Taken from [115].	43
2264	2.13 A schematic of the P0D side-view. Taken from [116].	44
2265	2.14 Left panel: The Interactive Neutrino GRID on-axis Detector. 14 modules are arranged in a cross-shape configuration, with the center modules being directly aligned with the on-axis beam. Right panel: The layout of a single module of the INGRID detector. Both figures are recreated from [109].	47
2270	3.1 Example of using Monte Carlo techniques to find the area under the blue line. The gradient and intercept of the line are 0.4 and 1.0 respectively. The area found to be under the curve using one thousand samples is 29.9 units.	52
2274	3.2 The area under a line of gradient 0.4 and intercept 1.0 for the range $0 \leq x \leq 10$ as calculated using Monte Carlo techniques as a function of the number of samples used in each repetition. The analytical solution to the area is 30 units as given by the red line.	53
2278	3.3 Three MCMC chains, each with a stationary distribution equal to a Gaussian centered at 0 and width 1 (As indicated by the black dotted lines). All of the chains use a Gaussian proposal function but have different widths (or 'step size $\sigma$ '). The top panel has $\sigma = 0.1$ , middle panel has $\sigma = 0.5$ and the bottom panel has $\sigma = 5.0$ .	58
2283	3.4 The log-likelihood from the fit detailed in <a href="#">DB: Link to AsimovA Sensitivity Section</a> as a function of the number of steps accumulated in each fit. Many independent MCMC chains were run in parallel and overlaid on this plot. The red line indicates the $1 \times 10^5$ step burn-in period after which the log-likelihood becomes stable.	59

---

2288	3.5	Left: The two dimensional probability distribution for two correlated parameters $x$ and $y$ . The red distribution shows the two dimensional probability distribution when $0 \leq x \leq 5$ . Right: The marginalised probability distribution for the $y$ parameter found when requiring the $x$ to be bound between $-5 \leq x \leq 5$ and $0 \leq x \leq 5$ for the black and red distribution, respectively. . . . .	62
2294	4.1	The NEUT prediction of the $\nu_\mu$ -H <sub>2</sub> O cross-section overlaid on the T2K $\nu_\mu$ flux. The charged current (black, solid) and neutral current (black, dashed) inclusive, charged current quasi-elastic (blue, solid), charged current 2p2h (blue, dashed), charged current single pion production (pink), and charged current multi- $\pi$ and DIS (Purple) cross-sections are illustrated. Taken from [149]. . . . .	68
2300	4.2	Illustration of the various processes which a pion can undergo before exiting the nucleus. Taken from [163]. . . . .	70
2302	4.3	Event displays from Super Kamiokande illustrating the “crisp” ring from a muon and the typically “fuzzier” electron ring. Each pixel represents a PMT and the color scheme denotes the accumulated charge deposited on that PMT. Figures taken from [171]. . . . .	72
2306	4.4	The electron/muon PID separation parameter for all sub-GeV single-ring events in SK-IV. The charged current (CC) component is broken down in four flavours of neutrino ( $\nu_\mu, \bar{\nu}_\mu, \nu_e$ and $\bar{\nu}_e$ ). Events with positive values of the parameter are determined to be electron-like. . . . .	76
2310	4.5	The variation of the measured dark rate as a function of date, broken down by PMT type. The SK-IV and SK-V periods span September 2008 to May 2018 and January 2019 to July 2020 respectively. The break in measurement between 2018 corresponds to the period of tank repair and refurbishment. Figure adapted from [173]. . . . .	78
2315	4.6	Comparison of the measured raw charge deposited per event from the stopping muon data samples between SK-IV (Blue) and SK-V (Red), split by the primary muon subevent and the associated decay electron subevent. . . . .	79

2319	4.7	The distribution of the reconstructed momentum from the muon ring divided by the distance between the reconstructed muon and decay elec- tron vertices as found in the stopping muon data sets of SK-IV (Black) and SK-IV (Red). Only events with one tagged decay electron and con- sidered. A Gaussian fit is considered in the range [2.0, 2.4] MeV/cm and illustrated as the solid curve. . . . .	80
2320			
2321			
2322			
2323			
2324			
2325	4.8	The $\chi^2$ difference between the SK-IV and SK-V reconstructed muon momentum divided by range when the SK-V is modified by the scaling parameter $\alpha$ . Both additive (Blue) and multiplicative (Black) scaling factors have been considered. In practice, the additive scaling factor actually uses the value of $(\alpha - 1.0)$ . . . . .	81
2326			
2327			
2328			
2329			
2330	4.9	A depiction of the topology patterns for fully-contained (FC), partially- contained (PC) and up-going muon (Up- $\mu$ ) samples included in this analysis. . . . .	82
2331			
2332			
2333	4.10	The predicted neutrino flux of the fully contained (FC) sub-GeV and multi-GeV, partially contained (PC) and upward-going muon (Up- $\mu$ ) events. The prediction is broken down by the $\nu_x \rightarrow \nu_e$ prediction (top left), $\nu_x \rightarrow \nu_\mu$ prediction (top right) and $\nu_x \rightarrow \nu_\tau$ prediction (bottom). All systematic dials are set to their nominal values and the Asimov A oscillation parameters are assumed. . . . .	84
2334			
2335			
2336			
2337			
2338			
2339	5.1	An “Oscillogram” that depicts the $P(\nu_\mu \rightarrow \nu_e)$ oscillation probability as a function of neutrino energy and cosine of the zenith angle. The zenith angle is defined such that $\cos(\theta_Z) = 1.0$ represents neutrinos that travel from directly above the detector. The four-layer constant density PREM model approximation is used and Asimov A oscillation parameters are assumed. . . . .	88
2340			
2341			
2342			
2343			
2344			
2345	5.2	The effect of $\delta_{CP}$ for atmospheric neutrinos given in terms of the neu- trino energy and zenith angle. The oscillogram compares the $P(\nu_\mu \rightarrow \nu_e)$ oscillation probability for a CP conserving ( $\delta_{CP} = 0.0$ ) and CP violating ( $\delta_{CP} = -1.601$ ) value of $\delta_{CP}$ . The other oscillation parameters assume the “Asimov A” oscillation parameter set given in Table 5.1. . . . .	90
2346			
2347			
2348			
2349			

---

2350      5.3	An illustration of the matter-induced effects on the oscillation probability, given as a function of neutrino energy and zenith angle. The top row of panels gives the $P(\nu_e \rightarrow \nu_e)$ oscillation probability and the bottom row illustrates the $P(\bar{\nu}_e \rightarrow \bar{\nu}_e)$ oscillation probability. The left column highlights the oscillation probability in a vacuum, whereas the middle and right column represents the oscillation probabilities when the four layer fixed density PREM model is assumed. All oscillation probabilities assume the “Asimov A” set given in Table 5.1, but importantly, the right column sets an inverted mass hierarchy. The “matter resonance” effects at $E_\nu \sim 5\text{GeV}$ can be seen in the $P(\nu_e \rightarrow \nu_e)$ for normal mass hierarchy and $P(\bar{\nu}_e \rightarrow \bar{\nu}_e)$ for inverted hierarchy. . . . .	91
2361      5.4	The oscillation probability for beam neutrino events given as a function of neutrino energy. All oscillation parameters assume the “Asimov A” set given in Table 5.1 unless otherwise stated. Each panel represents a change in one of the oscillation parameters whilst keeping the remaining parameters fixed. . . . .	92
2366      5.5	The number of electron-like events in the FHC and RHC operating mode of the beam, as a function of the oscillation probabilities. Both normal hierarchy (Solid) and inverse hierarchy (Dashed) values of $\Delta m_{23}^2$ are given. . . . .	93
2370      5.6	The oscillation probability $P(\nu_\mu \rightarrow \nu_e)$ , given as a function of neutrino energy and zenith angle, which highlights an example of the “fast” oscillations in the sub-GeV upgoing region. . . . .	95
2373      5.7	Illustration of the averaging procedure for $N = 2$ . The oscillation probabilities calculated on the finer left binning are averaged to obtain the oscillation probabilities in the coarser right binning. These averaged oscillation probabilities with the coarser binning are then applied to each event during the fit. . . . .	97
2378      5.8	Event rate of the SubGeV_elike_0dcy sample as a function of the number of sub-divisions per coarse bin. Each subplot represents the event rate of the sample at a different oscillation parameter set (thrown from the PDG priors). The red line in each subplot represents the mean of the event rate over the different values of sub-divisions for that particular oscillation parameter throw. . . . .	99

2384	5.9	Variance of event rate for each atmospheric sample as a function of the number of sub-divisions per coarse bin. The solid red line indicates the 0.1% threshold and the dashed red line is a graphical indication of the variance at a sub-division $N = 10$ . . . . .	100
2388	5.10	Variance of sample likelihood, when compared to ‘Asimov data’ set at Asimov A, for each atmospheric sample as a function of the number of sub-divisions per coarse bin. The solid red line indicates the 0.1% threshold and the dashed red line is a graphical indication of the variance at a sub-division $N = 10$ . . . . .	101
2393	5.11	The oscillation probability, $P(\nu_\mu \rightarrow \nu_e)$ (top row) and $P(\nu_e \rightarrow \nu_e)$ (bottom row), given as a function of neutrino energy and zenith angle. The left column gives the “fine” binning used to calculate the oscillation probabilities and the right column illustrates the “coarse” binning used to reweight the MC events. The fine binning choice is given with $N = 10$ , which was determined to be below threshold from Figure 5.9 and Figure 5.10. . . . .	102
2400	5.12	The calculation time taken to both calculate the oscillation probabilities and fill the “coarse” oscillograms, following the technique given in section 5.2, for the CUDAProb3 and ProbGPU (Red) calculation engines. CUDAProb3 has both a GPU (Blue) and CPU (Black) implementation, where the CPU implementation is multithreaded. Therefore, 8-threads (solid) and 40-threads (dashed) configurations have been used. Prob3, which is a CPU single-thread implementation has a mean step time of 1.142s. . . . .	104
2408	5.13	The density of the Earth given as a function of the radius, as given by the PREM model (Black) and the constant density four-layer approximation (Blue), as used in the official SK-only analysis. . . . .	105

2411	5.14 The oscillation probability, $P(\nu_\mu \rightarrow \nu_e)$ (top row) and $P(\nu_e \rightarrow \nu_e)$ (bottom row), given as a function of neutrino energy and zenith angle. The left column gives probabilities where the constant $Z/A = 0.5$ approximation which is used in the official SK-only analysis. The middle column gives the probabilities where the more accurate $Z/A = [0.468, 0.498]$ values as given in Table 5.2. The right column illustrates the difference in oscillation probability between the two different techniques. . . . .	107
2419	5.15 The density of the Earth given as a function of the radius, as given by the PREM model (Black), the constant density four-layer approximation (Blue), as used in the official SK-only analysis, and the quadratic approximation of the PREM model (Red). . . . .	108
2423	5.16 The oscillation probability, $P(\nu_\mu \rightarrow \nu_e)$ (top row) and $P(\nu_e \rightarrow \nu_e)$ (bottom row), given as a function of neutrino energy and zenith angle. The left column gives probabilities where the four-layer constant density approximation is used. The middle column gives the probabilities where the density is integrated over the trajectory, using the quadratic PREM approximation, for each $\cos(\theta_Z)$ is used. The right column illustrates the difference in oscillation probability between the two different techniques.	110
2430	5.17 The oscillation probability, $P(\nu_\mu \rightarrow \nu_e)$ (top row) and $P(\nu_e \rightarrow \nu_e)$ (bottom row), given as a function of neutrino energy and zenith angle. The left column gives probabilities where a fixed production height of 25km is used. The middle column gives the probabilities where the production height is analytically averaged. The right column illustrates the difference in oscillation probability between the two different techniques.	114

# **List of Tables**

2437	2.1	The various SK periods and respective live-time. The SK-VI live-time is calculated until 1 <sup>st</sup> April 2022. SK-VII started during the writing of this thesis. . . . .	21
2440	2.2	The trigger thresholds and extended time windows saved around an event which were utilised throughout the SK-IV period. The exact thresholds can change and the values listed here represent the thresh- olds at the start and end of the SK-IV period. . . . .	30
2444	2.3	The threshold momentum and energy for a particle to generate Cherenkov light in ultrapure water, as calculated in Equation 2.2 in ultrapure water which has refractive index $n = 1.33$ . . . . .	31
2447	3.1	Jeffreys scale for strength of preference for two models $A$ and $B$ as a function of the calculated Bayes factor ( $B_{AB} = B(A/B)$ ) between the two models [131]. The original scale is given in terms of $\log_{10}(B(A/B))$ but converted to linear scale for easy comparison throughout this thesis.	64
2451	5.1	Reference values of the neutrino oscillation parameters for two different oscillation parameter sets. . . . .	93
2453	5.2	Description of the four layers of the Earth invoked within the average constant density approximation of the PREM model [186]. . . . .	105
2455	5.3	The quadratic polynomial fits to the PREM model for four assumed layers of the PREM model. The fit to calculate the coefficients is given in [191], where $x = R/R_{Earth}$ . . . . .	108